Bubble Size Effect on the Gas-lift Technique

Bubble Size Effect

on the Gas-lift Technique

Proefschrift

ter verkrijging van de graad van doctor
aan de Technische Universiteit Delft,
op gezag van de Rector Magnificus prof. dr. ir. J.T. Fokkema
voorzitter van het College voor Promoties,
in het openbaar te verdedigen
op dinsdag 11 mei 2004 om 10.30 uur

door

Sébastien Christophe Laurent GUET
Diplôme d'études approfondies
Dynamique des fluides et des transferts
Université Paris XI - Centre d'Orsay,
geboren te Meknes.

Dit proefschrift is goedgekeurd door de promotoren:
Prof. dr. ir. G. Ooms
Prof. dr. R.V.A. Oliemans

Samenstelling promotiecommissie:

Rector Magnificus,	voorzitter
Prof. dr. ir. G. Ooms,	Technische Universiteit Delft, promotor
Prof. dr. R.V.A. Oliemans,	Technische Universiteit Delft, promotor
Prof. dr. ir. P.J. Jansens,	Technische Universiteit Delft
Prof. dr. D. Lohse,	Universiteit Twente
Prof. dr. J. Magnaudet,	Institut de Mécanique des Fluides de Toulouse
Prof. dr. R.F. Mudde,	Technische Universiteit Delft
Prof. dr. ir. J. Westerweel,	Technische Universiteit Delft

The work presented in this thesis was supported financially by the European Union through the European Research Network on Nonideal Turbulence (contract HPRN-CT-200000162).

Published and distributed by DUP Science
DUP Science is an imprint of
Delft University Press
P.O. Box 98
2600 MG Delft
The Netherlands
Telephone: +31 15 27 85 678
Telefax: + 31 15 27 85 706
E-mail: info@library.tudelft.nl

ISBN 90-407-2492-X

Keywords: gas-lift, bubbly flow, bubble size

Printed in The Netherlands.

Contents

Summary

Bubble size effect on the gas-lift technique, by Sébastien Guet

The gas-lift technique uses gas injection in vertical oil wells to decrease the gravitational pressure drop. The decreased pressure in the production pipe results in an increase of the pressure drop from the reservoir to the oil well and enhances the oil production. In this thesis we investigated the influence of the bubble size and initial concentration distribution on the gas-lift technique efficiency. A vertical upward bubbly pipe flow of air and water is used, with a height of $18m$ and a diameter of $72mm$. The flow velocity conditions investigated in the experiments were representative of practical gas-lift circumstances. Different bubble injectors were tested in order to vary the size and initial concentration distribution of the bubbles. The influence of the initial concentration distribution was limited. The effect of bubble size, on the contrary, was significant. It was due to three contributions: the effect of the bubble size on the flow pattern changes, on the radial distribution (of void fraction and of gas and liquid velocity) and on the relative velocity between the gas and the liquid.

To study separately these different contributions associated with bubble size changes we developed and used local measurement techniques. We investigated the possibility of Laser-Doppler Anemometry (LDA) measurements in bubbly flows. These tests were conducted in two different experimental configurations, corresponding to a stirred vessel and a pipe flow. To determine the size and the velocity of the bubbles a four-point optical fibre probe was validated and used. We also developed a method for estimating the bubble shape and orientation based on the time series provided by the four-point optical fibre probe. This method was first validated and then applied to our multiple bubbles pipe flow conditions.

We then studied the effects of bubble size and concentration distribution on the gas-lift technique. In general it can be concluded that a decreasing bubble size increases the efficiency of the gas-lift technique. This is, among others, caused by the fact that the initial bubble size significantly affected the flow pattern transition from bubbly flow to slug flow. This effect could be described by using a bubble size dependent critical void fraction relation for the transition from bubbly flow to slug flow. With decreasing bubble size the transition shifts to larger values of the void fraction.

Measurements were conducted to measure the influence of the bubble size on the velocity profile of gas and liquid and on the bubble concentration profile. For this purpose the four-point probe optical fibre probe and the LDA measurement technique were used. The velocity and concentration profiles were strongly influenced

by the bubble size. Also the parameters C_0 and $|U_{drift}|$ of the drift-flux model are therefore bubble-size dependent. Based on the measurements, mathematical relations have been developed to describe these bubble size effects on the drift-flux parameters.

We also developed a numerical model based on the Euler-Euler modelling approach for predicting the radial profiles of the void fraction and velocity as a function of the relevant parameters, such as bubble size. The predictions were in reasonable agreement with experimental data.

Samenvatting

Invloed van de belgrootte op de "gas-lift" techniek, door Sébastien Guet

De gas-lift techniek maakt gebruik van injectie van gas in verticale olieproductie putten met het doel het door de zwaartekracht veroorzaakte drukverschil over deze productieputten te verkleinen. De door de gas-lift techniek veroorzaakte afgenomen druk onderin een productieput resulteert in een toename van het drukverschil tussen het oliereservoir en de productieput en verhoogt de olieproductie. In dit proefschrift worden de resultaten van een onderzoek beschreven betreffende de invloed van de grootte en de initiële concentratieverdeling van de geïnjecteerde bellen op de efficiëntie van de gas-lift techniek. Bij dit onderzoek werd gebruikt gemaakt van een bellenstroming (van lucht in water) door een pijp met een hoogte van $18m$ en een diameter van $72mm$. De stroomsnelheid van het bellenmengsel was representatief voor praktische gas-lift omstandigheden. Verschillende belleninjectoren werden getest met als doel de grootte en initile concentratieverdeling van de bellen te kunnen variëren. De invloed van de initiële concentratieverdeling was beperkt. Het effect van de belgrootte daarentegen was aanzienlijk en werd veroorzaakt door drie factoren: de invloed van de belgrootte op het stromingspatroon, op de radiale verdeling (van de concentratie en snelheid van het gas en de vloeistof) en op de relatieve snelheid van het gas ten opzichte van de vloeistof.

Om deze verschillende invloeden te bestuderen hebben we locale meettechnieken ontwikkeld en gebruikt. We onderzochten b.v. de mogelijkheid van LDA-metingen (LDA : Laser-Doppler Anemometry) in een bellenstroming. Deze metingen werden uitgevoerd in twee verschillende opstellingen, te weten in een geroerd vat en in een pijpstroming. Om de grootte en snelheid van de bellen te bepalen werd een optische vierpunt vezelsonde gebruikt. Tevens ontwikkelden we een methode voor het schatten van de vorm en oriëntatierichting van de bellen door gebruik te maken van de signalen van de vierpunt vezelsonde. Deze methode is eerst gevalideerd en daarna toegepast op de bellenstroming in de verticale pijp.

Vervolgens bestudeerden wij de effecten van de belgrootte en initiële concentratieverdeling op de gas-lift techniek. Als algemene conclusie kunnen we stellen, dat een afnemende belgrootte de efficiëntie van de gas-lift techniek verhoogt. Dit wordt o.a. veroorzaakt door het feit, dat de belgrootte een belangrijke invloed heeft op de overgang in stromingspatroon van bellenstroming naar slugstroming. Dit effect kan beschreven worden met een belgrootte afhankelijke relatie voor deze overgang. Met afnemende belgrootte vindt de overgang plaats bij hogere waarden van de gas concentratie.

Metingen werden ook uitgevoerd om de invloed van de belgrootte op het snelheids-

profiel (van gas en vloeistof) en het bellenconcentratie profiel te meten. Hierbij werd gebruik gemaakt van de optische vierpunt vezelsonde en de LDA meettechniek. Het snelheidsprofiel en het concentratie profiel werden sterk benvloed door de belgrootte. Ook de parameters C_0 en $|U_{drift}|$ behorende bij het drift-flux model zijn daarom afhankelijk van de belgrootte. Wiskundige relaties zijn ontwikkeld om deze afhankelijkheid te beschrijven.

Ook is een numeriek model ontwikkeld, gebaseerd op de Euler-Euler methode, met als doel de gas concentratie en snelheidsprofielen te voorspellen als functie van de relevante parameters zoals de belgrootte. De voorspellingen zijn in redelijke overeenstemming met de experimentele gegevens.

Chapter 1

Introduction

1.1 Motivation

Two-phase gas-liquid flow situations are encountered in a large variety of applications, such as bubble columns, stirring vessels, cavitating flows or transportation lines. The different type of problems found in these various two-phase flow applications suggest two-phase flow problems to be seen as 'a family of topics, rather than a single topic' (Batchelor, 1989). Together with the progress in computer science and chemical technologies, the perspective of improving the efficiency of industrial processes has become a subject of important study during the last decades. A topic of particular relevance for large-scale industrial applications is a vertical upward bubbly flow in a pipe. This situation can for instance be found in airlift reactors for enhancing mixing, or for providing oxygen to microorganisms. It is also encountered in mining technologies and wastewater treatment.

For underground oil recovery the gas-lift technique is often used. It is employed when a well down-hole pressure is decreasing towards a situation of zero oil production. By using gas injection in the well tubing the gravitational pressure drop is reduced. The decreased pressure results in an increased oil flow rate. During the application of the gas-lift technique the gas is injected via a large nozzle injector. The oil flow rate corresponds to moderate liquid Reynolds number flows. This results in a gravity-driven bubbly flow with relatively large bubbles.

The bubble size can be expected to have significant effects on the gas-lift efficiency. For instance, the bubble size influences the bubble relative velocity and therefore modifies the bubble residence time in the pipe for given gas and oil input flow conditions. It is affecting the radial distributions of void fraction and oil and gas velocities, and might have an effect on the flow pattern conditions. Also, the liquid input conditions have an influence on the velocity profiles and turbulence properties. These hydrodynamic effects are expected to contribute to the gravitational pressure drop associated with given mean flow conditions.

The aim of this thesis is to analyse in more details the effects of the bubble size and bubble injector configuration on the gas-lift efficiency. The flow conditions investigated are bubbly flow and slug flow. We will investigate experimentally how the stationary, time average pressure is affected by the bubble size and liquid input conditions in upward bubbly pipe flows and the corresponding gas-lift efficiency.

To separate the different influences due to the bubble size effect mentioned above, we will measure the local flow properties, and their change with bubble size and bubble initial distribution. A simplified numerical model will also be developed and validated for predicting the bubble size and liquid input effects on the gas-lift technique efficiency.

1.2 Outline

This thesis is organized as follows. In chapter 2 the particularities of gas-liquid flows are described, with emphasis on vertical bubbly pipe flows and the typical conditions associated with gas-lift operations. A brief overview of bubble size effects is given, and the relevant non-dimensional numbers for gas-lift characterisation are reviewed. This permits to derive the appropriate laboratory conditions necessary for studying the gas-lift efficiency associated with bubble injector and flow conditions changes, and to clarify the limitations of the present experiments.

In chapter 3, the experimental set-up and measurement techniques are described and assessed. The sections reporting the measurement technique assessments as well as the results reported in the subsequent chapters of this thesis are essentially based on publications; therefore they might be read independently, and some overlap might be found. The reader is however referred to section 3.1 for a general presentation of the experimental set-up and the bubble injectors used in this study. The local measurement techniques used in the present research are: back-scatter Laser Doppler Anemometry for the liquid velocity determination (section 3.2 and 3.3), and a four-point optical fibre probe for the bubble velocity and chord length determination (section 3.4). In a separate section, we report about the possibility of measuring the bubble shape and orientation by using our four-point optical fibre probe (section 3.5).

In chapter 4 we report the experimental results on the changes in gas-lift efficiency associated with our different bubble injectors. The effect of the initial bubble size and bubble concentration on the gas-lift efficiency is studied with a particular emphasis on the changes in the transition from bubbly flow to slug flow with bubble injector configuration. A bubble size dependent model for the bubbly flow to slug flow transition boundary is developed. We also propose a simple model for describing the associated consequences on gas-lift performances, based on the drift-flux model and our flow pattern transition model.

In chapter 5 we use a combination of our local measurement techniques for investigating in more detail the effect of bubble size on the gas-lift efficiency in bubbly flow conditions. Using the measured distributions of void fraction and phase velocities associated with given bubble size conditions, the gas-lift changes due to bubble relative velocity and transverse distribution effects are studied separately. We will then develop a bubble size and flow condition dependent drift-flux parameter model for predicting the area-average void fraction in bubbly flow.

In chapter 6 we develop a numerical model, based on the Euler-Euler approach, for predicting the changes in radial profiles of void fraction and velocities due to bubble size changes. The results obtained with this model are compared with experimental results reported in literature for small-diameter bubbly pipe flows, and with our experimental results. This model is then used to infer the bubble size ef-

fect on the gravitational pressure gradient by computing the drift-flux distribution parameter dependence on the bubble size and liquid input. These results are also compared with our experiments. In chapter 7 the conclusions of this project and the recommendations for further research are given.

Chapter 2

Gas-liquid flow during gas-lift

2.1 Introduction

2.1.1 Flow pattern

In contrast to single-phase flow, multiphase flow is characterised by interfaces between phases, resulting in discontinuities of associated properties. Various phase behaviours and distributions can be observed in practice, depending on the flow conditions. The determination of the flow pattern is necessary prior to a detailed modelling of the flow. In upward co-current vertical pipe flows of a gas and a liquid four essential flow regimes are commonly distinguished (figure 2.1.a):

(1)- Bubbly flow: the gas phase is dispersed in the liquid phase. This pattern corresponds to low void fraction conditions. Two liquid input conditions are of importance for the bubble size determination:

(a)- the low to moderate liquid input bubbly flow conditions, for which almost no bubble break-up occurs. In those conditions the bubble size is only affected by the inlet device and entrance conditions (Taitel *et al.*, 1980),

(b)- the finely dispersed bubbly flow regime, corresponding to large liquid input conditions. The bubbles are broken into small bubbles and a maximum stable bubble diameter can be connected to the turbulence conditions and surface tension properties (Hinze, 1975; Chen *et al.*, 1997).

(2)- The slug flow regime, corresponding to larger values of the void fraction. In these conditions the flow consists in large pockets of gas and liquid, eventually containing also dispersed bubbles. Near the wall, a falling liquid film is observed. Strong fluctuations of the liquid flow rate and pressure are observed in this regime.

(3)- Churn flow: this flow pattern corresponds to large gas input and moderate void fraction.

(4)- Annular flow: a flow of gas with small droplets of liquid in the centre of the pipe, and an annular film of liquid at the wall. The typical conditions are large gas and liquid input, with large void fraction.

The existing flow pattern at given flow conditions is in general determined by making use of a flow pattern map, as illustrated in figure 2.1(b) for our air-water vertical pipe of $72mm$ inner diameter.

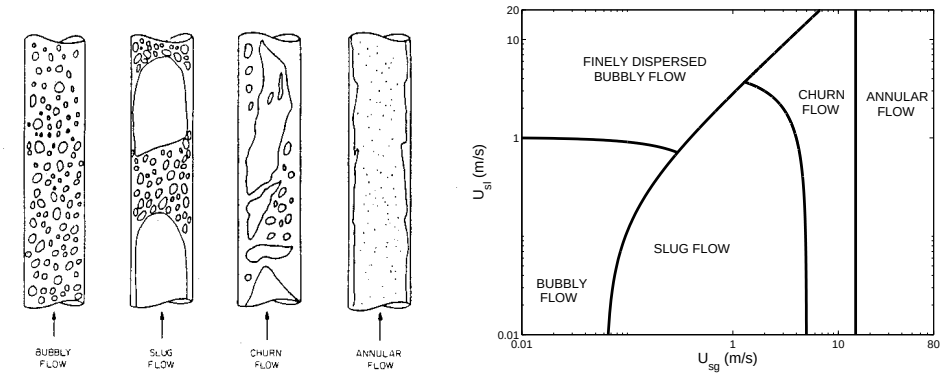

(a) Flow patterns (b) Flow map

Figure 2.1: Flow patterns observed in vertical upward bubbly pipe flow. (a) Visual observation, from Taitel *et al.* (1980); (b) Flow map for a $72mm$ diameter air-water pipe according to the model of Taitel *et al.* (1980).

2.1.2 Bubble relative motion

The relative velocity between *single* gas bubbles and the surrounding liquid is the result of a competition between the gravity and drag force. Experimental results on the rise velocity of single bubbles in an infinite medium of water have been collected from various experimental investigations in Clift *et al.* (1978) (figure 2.2.a). The terminal velocity values in clean and contaminated liquids are differing for a given spherical equivalent bubble diameter. This is due to the changes in bubble shape with the contamination level, which in turn affects the equivalent drag force coefficient (Tomiyama *et al.*, 2002a). Gravity is the dominant force for large bubbles (it is proportional to the bubble volume). Therefore the bubble terminal velocity increases with the bubble spherical equivalent diameter.
In figure 2.2(b), the correlations proposed by Peebles and Garber (1953) and Tomiyama *et al.* (2002a) for the terminal velocity of a single bubble in respectively clean and contaminated water are plotted. The experimental findings of figure 2.2(a) are properly described with these models.

In multiple bubbles flow conditions, i.e. bubbly flows with non-zero gas fraction, the mean relative velocity between the gas bubbles and the liquid as measured with local measurement techniques is lower than the values of the terminal velocity of a single bubble in an infinite medium. This void fraction relative velocity effect can be taken into account by using an hindering function $w(\epsilon)$ (Richardson and Zaki, 1954; Rivière and Cartellier, 1999; Zenit *et al.*, 2001; Garnier *et al.*, 2002):

$$U_{slip} = U_t w(\epsilon), \tag{2.1}$$

in which U_t is the terminal velocity of a single bubble in an infinite medium (as described by figure 2.2), and $0 < w(\epsilon) < 1$. More details on this relative velocity decrease at increased void fraction are given by Kowe *et al.* (1998) by using the concept of an interstitial liquid velocity, different from the time average liquid velocity.

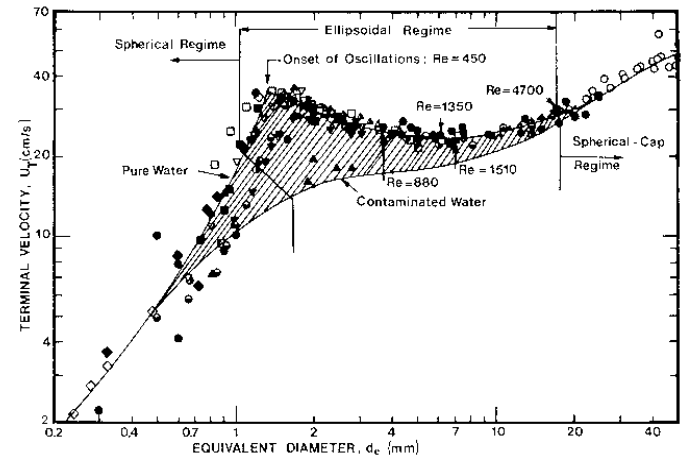

(a)

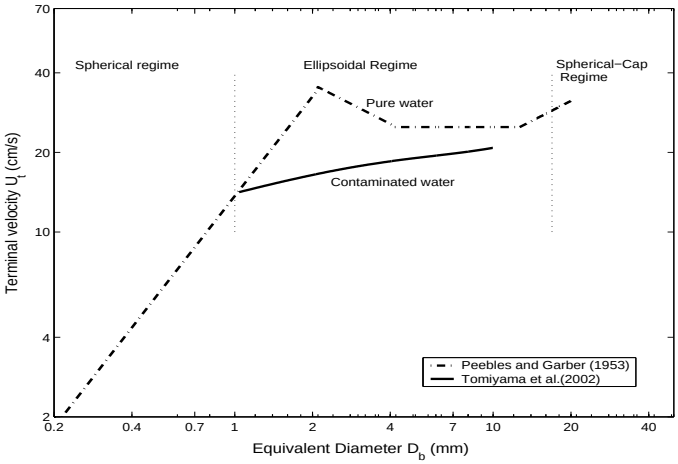

(b)

Figure 2.2: Terminal velocity of a single bubble in water as a function of the bubble spherical equivalent diameter. (a): from Clift *et al.* (1978), p172; (b): using the models of Peebles and Garber (1953) and Tomiyama *et al.* (2002a) for clean and contaminated water respectively.

2.1.3 Void fraction profiles in upward bubbly pipe flows

Depending on the flow conditions, the void fraction radial profile can present either a peak near the pipe wall or a maximum value at the centre line (Serizawa *et al.*, 1975; Wang *et al.*, 1987; Liu, 1993a; Grossetête, 1995). In their pioneering work, Serizawa *et al.* (1975) reported that the void fraction radial profile was evolving from a wall-peak to a core-peak trend with increased gas input (see figure 2.3.a), and proposed a simple map to describe this effect (figure 2.3.b). In general the bubble size is increasing with the gas input when using a given bubble injector made of porous material (Koide *et al.*, 1968) or using a nozzle. To study separately the

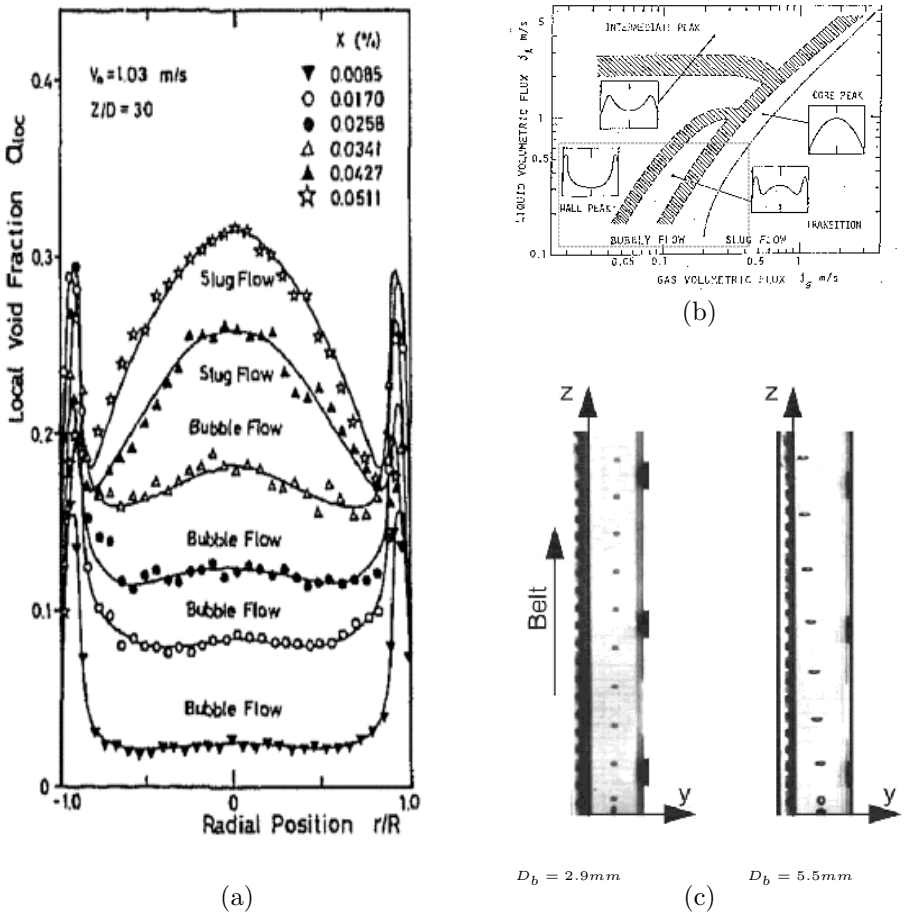

Figure 2.3: (a)Void fraction profiles measured by Serizawa *et al.* (1975) in a $60mm$ diameter air-water pipe at increased gas input. (b) A simple map for wall and core peaking bubbly flow as proposed by the authors (Serizawa *et al.*, 1994). Also the experimental conditions studied in our work are shown with a dotted frame. (c) Observations on bubble transverse migration in a linear shear field by Tomiyama *et al.* (2002b). Depending on the spherical equivalent diameter D_b, the bubble migrate towards the wall or towards the belt.

effect of bubble size and gas input, a special gas injector was used by Liu (1993a) for large liquid input conditions. It was shown by the author that the wall-to-core peak transition was triggered by the bubble diameter. The observed critical bubble diameter associated with the onset of transition was $D_b \approx 5 - 6mm$ in air-water bubbly pipe flow. More recently, Tomiyama (1998) and Tomiyama *et al.* (2002b) reported experiments on a single bubble in a linear shear field, and showed that the equivalent transverse lift force was changing sign with increased bubble size at large bubble Reynolds number ($Re_b > 50$) and large Eötvös number. This was due to the interactions between the (non-spherical) bubble wake and the shear field. In figure 2.3(c), series of photos taken by Tomiyama *et al.* (2002b) are clearly illustrating the different transverse motion of single small and large bubble placed in a linear shear field. Similar deformation induced lift force effects are reported for drops (Magnaudet *et al.*, 2003).

Also the pipe diameter has an impact on the void fraction profiles observed in upward bubbly pipe flows. For large diameter pipes ($D_p > 10cm$), experimental investigations mostly reported parabolic profiles of void fraction (Ohnuki and Akimoto, 1996; Mudde and Saito, 2001; Ohnuki and Akimoto, 2000). A near wall peak of void fraction can however be observed, but the magnitude is lower than for small diameter pipes (Ohnuki and Akimoto, 2000). In those large-scale flow conditions, the flow can however present inversed liquid velocities at the wall (Mudde and Saito, 2001). This would imply a change of the lift force direction in the near wall boundary, due to an inversed velocity gradient in this area. Also bubble dispersion effects due to the liquid turbulence are playing a significant role in the phase distribution in large pipes (Ohnuki and Akimoto, 2000, 2001).

2.2 The gas-lift technique

2.2.1 Principle

The gas-lift technique is a gravity-based pumping technique, which uses gas injection in a vertical pipe to increase the liquid input. In petroleum engineering this technique is used when the bottom pressure of an oil well is not large enough to create an upward velocity of oil. The robustness and reliability of the technique are known advantages, due to the absence of moving component and its ability to cope with multi-component fluids or mixtures containing solid particles. Initially the oil in a well can be naturally flowing upward, due to the large pressure in the down-hole reservoir, called Bottom Hole Pressure (BHP). Due to years of production, the BHP and the oil flow are decreasing till the BHP is equal to the gravitational pressure P_{Hl} due to the weight of the oil column, corresponding to zero liquid flow rate:

$$P_{Hl} = P_f + \rho_l g H, \tag{2.2}$$

where H is the total height of the oil column, P_f is the pressure in the pipe at the top and ρ_l is the liquid density. This critical pressure drop value determines the lifetime of naturally flowing single-phase oil wells. There exist a variety of gas lifted oil well installations. It can be vertically oriented or inclined, and there might be more than a single well producing from a site (e.g. dual gas-lifted wells). Also the flow rate conditions can differ from one situation to the other. The operating conditions

can be distinguished particularly by: the operating pressures (at the bottom and at the top), the well geometrical properties (length, diameter of the pipe and gas inlet geometries), and the associated flow pattern. By reducing the overall pressure drop, the necessary BHP for generating a net liquid flow decreases. In a section of the pipe, the equivalent average mixture density is evaluated from

$$< \rho_m >= < \epsilon > \rho_g + (1- < \epsilon >)\rho_l, \tag{2.3}$$

where $< \epsilon >$ denotes the area average void fraction. The overall gravitational pressure gradient in the pipe can then be written, considering a mixture model, as

$$P_{Hm} = \int_{z=0}^{z=H} < \rho_m > g dz. \tag{2.4}$$

Provided the void fraction is different from zero, $P_{Hm} < P_{Hl}$ since $\rho_g << \rho_l$: the contribution due to gravity to the pressure drop in the case of a gas-liquid flow is lower than the corresponding single-phase flow pressure drop. In the case of an oil well, the reservoir pressure and the top level pressure (called tubing head) are fixed, i.e. the total pressure drop is constant. The consequence of a lower gravitational pressure drop in the vertical pipe is therefore to compensate by an increased pressure drop through the reservoir, resulting in an increased net oil flow rate. A typical gas lifted oil well installation is sketched in figure 2.4. The gas is brought from the top into an annular chamber (the casing) with a compressor, then injected into the oil well (tubing) via nozzles, or gas-lift valves. These injectors are using two nozzles of typically a few millimetre diameter.

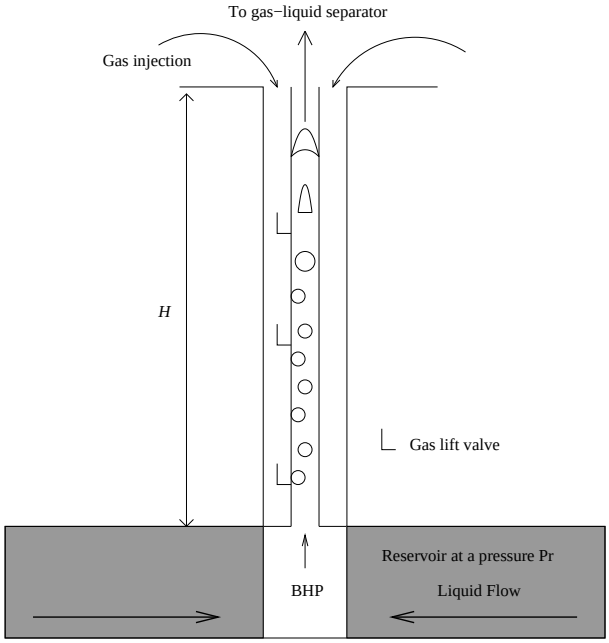

Figure 2.4: Schematic view of a gas-lift installation.

After the starting period only the deepest valve is injecting gas in the pipe, being the most efficient for decreasing the total gravitational pressure drop.

Relation (2.3) and (2.4) clearly illustrate the direct impact of the mean void fraction value $< \epsilon >$ on the gas-lift performance. Particularly, the radial void fraction profile as well as the relative velocity between the phases affect the mean void fraction value, hence influencing the gas-lift efficiency for given flow conditions.

2.2.2 Gas-lift prediction approaches

The pressure drop in the pipe and in the reservoir determines the flow rate observed in a gas-lifted well. Those coupled parts of the well are commonly modelled using the Tubing Performance Curve (TPC) and the Inflow Performance Relationship (IPR), respectively.

The liquid flow rate associated with a given pressure drop in the reservoir is expressed using a relation derived from Darcy's law for the radial inflow through the reservoir:

$$Q_l = P_I \Delta P_{res}, \tag{2.5}$$

where Q_l is the liquid flow rate, ΔP_{res} is the pressure drop from the far field to the pipe, and P_I is the Productivity Index (also called PI), characterising a mean reservoir permeability.

The tubing performance curve (TPC) relates the liquid flow rate to the pressure drop in the production tubing for a given ratio of gas to liquid input. It is modelled by considering the pressure gradient as the sum of the contributions due to gravity, friction and acceleration. To take into account the effect of the flow conditions on the gravitational pressure gradient, correlations based on the drift-flux model (Zuber and Findlay, 1965) are of practical usefulness (section 2.2.3).

By combining the Inflow Performance Relationship and the Tubing Performance Curve, it is possible to obtain a well operation point corresponding to a given flow situation. This is schematically represented in figure (2.5).

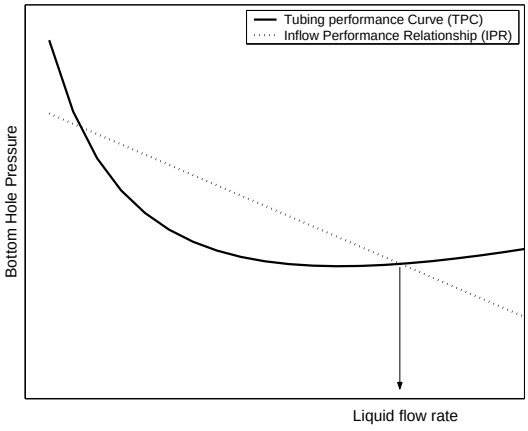

Figure 2.5: Gas-lift operating point determination, by using the IPR and TPC curves. A TPC curve is connected to a fixed ratio of gas to liquid input.

The left part corresponds to the gravity-dominated regime. In the right part the frictional pressure gradient starts to play a role, the liquid input being increased. The two intersection-points between the IPR and TPC curves are potential operating conditions. However the lower production rate point is corresponding to an unstable equilibrium. If the liquid flow rate is reduced slightly the intake pressure is required to be larger than the value that the reservoir can provide. Any negative perturbation is therefore amplified in this situation and the well might stop flowing. Due to the occurrence of coupled pressure oscillations between the casing and the tubing an instable behaviour might be observed, called heading phenomena. This corresponds to intermittent gas injection through the gas-lift valve. If the liquid flow rate is perturbed positively a lower intake pressure is required according to the TPC curve. The reservoir being able to supply this lower pressure, the oil production will increase and reach the value corresponding to a stable equilibrium operating point. It is however possible to prevent the heading instability and to operate in the gravity dominant region associated with a negative slope of the TPC curve. To that purpose, an electric gas-lift valve can be used for injecting the gas at constant gas flow rate through the injector, therefore avoiding gas pressure fluctuations in the casing.

In general, the point used for the gas-lift operating condition previsions is therefore the second intersection point between the TPC and IPR, corresponding to the large liquid flow rate part of the TPC curve. In these conditions friction also plays a role, and helps stabilising the gas pressure in the casing. Repeating this operation for various gas and liquid flow rates by using different TPC curves permits to generate a production curve, i.e. a plot of the liquid flow rate versus gas flow rate.

2.2.3 The drift-flux model

The prediction of a set of TPC curves associated with various gas and liquid input conditions calls for a proper modelling of the pressure drop corresponding to given flow conditions. The drift-flux model permits to incorporate the contributions of the bubble relative velocity and bubble radial profile on the gravitational pressure drop prediction.

The drift-flux model developed by Zuber and Findlay (1965) incorporates two particularly important phenomena in a one-dimensional model:

- The non-zero bubble relative velocity taken into account by the weighted mean drift velocity
$$|U_{drift}| = \frac{< \epsilon U_{drift} >}{< \epsilon >}, \tag{2.6}$$
- the (non-homogeneous) transverse profile of void fraction and phase fluxes. These effects are incorporated by defining a distribution parameter:
$$C_0 = \frac{< \epsilon j >}{< \epsilon >< j >}. \tag{2.7}$$

The symbol $< a >$ and $|a|$ represent respectively the area-average value and the void fraction weighted averaging procedure applied to a. The symbol ϵ represents the local void fraction, $< j >$ is the area-average mixture velocity ($< j > = U_{sg} + U_{sl}$) and

$|U_{drift}|$ is the weighted mean drift velocity, in which $U_{drift} = U_g - j$ is the relative velocity of the bubble with respect to the local mixture velocity.

The drift-flux model is formulated as:

$$\frac{U_{sg}}{<\epsilon>} = C_0 < j > + |U_{drift}|. \tag{2.8}$$

U_{sg} and U_{sl} are the superficial gas and liquid velocities, i.e. the area average gas and liquid volumetric fluxes ($U_{sg} = \frac{Q_g}{A}$ and $U_{sl} = \frac{Q_l}{A}$). The drift-flux model can be applied to predict the mean void fraction $<\epsilon>$ from the known global quantities U_{sg} and U_{sl} and by using appropriate models for C_0 and $|U_{drift}|$. The gravitational pressure gradient can then be computed with equation (2.3) and (2.4). It is therefore of practical importance for gas-lift performance predictions to investigate how the drift-flux parameters are changing with bubble size and liquid input. In the coming section a scaling analysis is carried out to infer the appropriate experimental conditions necessary for studying these effects.

2.3 Scaling analysis

In this section a scaling approach is used, based on the Navier-Stokes equations for the gas and liquid phases and the stress jump at the gas-liquid interface. This analysis provides a better understanding on how to carry out experiments in order to simulate real gas-lift conditions in a laboratory. It will also help in interpreting and generalising the experimental results. The requirements for obtaining a dynamic similarity between two gas-liquid flow situations are the equality of dimensionless flow parameters, as well as the equality of the initial and boundary conditions at all dimensionless times. This last consideration includes the equality of imposed distribution of dimensionless variables (Geraets, 1986), such as the initial distribution of void fraction and phase velocities.

2.3.1 Dimension analysis

2.3.1.1 Reference parameters

The reference velocity is taken as the liquid superficial velocity: $U = U_{sl} = \frac{Q_l}{A}$. The reference density ρ is the liquid density. The reference length L is taken as the pipe diameter D_p. The bubble size is considered by using the spherical equivalent bubble diameter D_b in our analysis. It should be stressed here that the bubble size is related to the bubble inlet conditions, the fluid properties, the local pressure condition (the bubbles are expanding) and eventually the liquid flow conditions (in case of finely dispersed bubbly flow).

2.3.1.2 Dimensionless variables

We introduce the dimensionless quantities:

$\tilde{\rho_g} = \frac{\rho_g}{\rho_l}$, $\tilde{\vec{u_k}} = \frac{\vec{u}_k}{U}$, $\tilde{P_k} = \frac{P_k}{\rho_l U^2}$ with $k = g$ and l, $\tilde{D_b} = \frac{D_b}{L}$, $\tilde{t} = \frac{tU}{L}$ and $\tilde{\vec{\nabla}} = L\vec{\nabla}$.

2.3.1.3 Dimensionless version of the equations

Our analysis is based on the non-dimensional versions of the state equation for the gas phase ($\frac{\tilde{P}_g}{\tilde{\rho_g}} = const.$), the Navier-Stokes equations for the gas and the liquid, and the stress jump at the interface. This approach has proven to guarantee a proper scaling of the effect of the pipe diameter in horizontal gas-liquid pipe flow by varying the equivalent gravity potential g in a rotating experimental set-up (Geraets, 1986):

$$\frac{D\tilde{\vec{u_g}}}{D\tilde{t}} = \frac{gL}{U^2}\vec{z} - \frac{1}{\tilde{\rho_g}}\tilde{\vec{\nabla}}\tilde{P}_g + \frac{\mu_g}{UL\rho_g}(\tilde{\vec{\nabla}}^2\tilde{\vec{u_g}} + \frac{1}{3}\tilde{\vec{\nabla}}(\tilde{\vec{\nabla}}.\tilde{\vec{u_g}})), \tag{2.9}$$

$$\frac{D\tilde{\vec{u_l}}}{D\tilde{t}} = \frac{gL}{U^2}\vec{z} - \tilde{\vec{\nabla}}\tilde{P}_l + \frac{\mu_l}{UL\rho_l}\tilde{\vec{\nabla}}^2\tilde{\vec{u_l}}, \tag{2.10}$$

$$\begin{aligned}(\tilde{P}_g - 2\frac{\mu_g}{UL\rho_l}(\frac{\partial \tilde{u_{g,n}}}{\partial\tilde{n}} - \frac{1}{3}\tilde{\vec{\nabla}}.\tilde{\vec{u_g}})) - (\tilde{P}_l - 2\frac{\mu_l}{UL\rho_l}(\frac{\partial \tilde{u_{l,n}}}{\partial\tilde{n}})) \\ = \frac{\sigma}{\rho_l U^2 L}(\frac{1}{\tilde{R_{b1}}} + \frac{1}{\tilde{R_{b2}}}),\end{aligned} \tag{2.11}$$

in which the $\tilde{n}$ direction is corresponding to the local gas-liquid interface normal, $\tilde{R_{b1}}$ and $\tilde{R_{b2}}$ are the dimensionless radii of curvature of the interface and $\vec{z}$ is the unit vector in the direction of $\vec{g}$. A complete set of six non-dimensional numbers is identified:

- The Reynolds numbers for the liquid $Re_{sl} = \frac{UL\rho_l}{\mu_l}$ and for the gas $Re_{sg} = \frac{UL\rho_g}{\mu_g}$,
- the Froude number $Fr = \frac{U^2}{gL}$,
- the Euler number $Eu = \frac{P_g}{\rho_g U^2}$,
- the ratio of densities $\frac{\rho_g}{\rho_l}$, and
- the Weber number $We = \frac{\rho_l U^2 L}{\sigma}$.

2.3.1.4 Dynamic similarity

For a proper dynamic scaling, the relevant non-dimensional numbers should be the same in both situations. Another equally important criteria for a proper dynamic similarity between the laboratory experiment and the real situation is the equality of imposed distributions of dimensionless variables.

The dynamic of the bubbly flow is thus exactly the same between the real gas-lift conditions and the laboratory if the six non-dimensional numbers given above are equal in both situations, provided that also the initial distributions and values of the dimensionless velocity, pressure and bubble size are equal. Particularly, to properly study the bubble injector and bubble size effects on the gas-lift technique, the initial distribution of dimensionless bubble size $\frac{D_b}{L}$ and the phase velocity ratio $\frac{U_{sg}}{U_{sl}}$ should be the same in both situations.

2.3.1.5 Simplifications

Considering the particular case of a vertically oriented pipe flow driven by gravity during gas-lift conditions, some simplifications are formulated.

- The most relevant force in the case of the gas-lift technique is the gravity force due to the difference in density between the two fluids. The relevant Froude number for dispersed bubbly flow driven by gravity is a densitometric one:

$$Fr_{sl} = \frac{\rho_l}{\Delta\rho}\frac{U^2}{gL}. \tag{2.12}$$

- The inertial effects due to the gas are neglected, assuming a low gas density compared to the liquid phase :

$$\frac{\rho_g}{\rho_l} << 1. \tag{2.13}$$

  This will restrict the present study to low pressure conditions.

- The viscous effects in the gas phase are neglected.

- The Euler number takes into account the compressibility effects. Only the static contribution will be considered in the present analysis.

2.3.1.6 Final formulation

After the simplifications, five non-dimensional numbers remain. The group of relevant dimensionless numbers can be used to investigate the axial pressure gradients occurring through the tubing for various fluid properties, bubble size and flow conditions:

$$\frac{\left(\frac{dP}{dz}\right)}{\left(\frac{\rho U^2}{L}\right)} = f(Fr_{sl}, Re_{sl}, We, \frac{D_b}{L}, \frac{U_{sg}}{U_{sl}}). \tag{2.14}$$

In the next section, we will identify the most relevant numbers for properly studying the effects of the dimensionless bubble size $\frac{D_b}{L}$.

2.3.2 Experimental scaling

In this section we formulate the conditions necessary for experimentally simulating the bubble size effects in a real gas lifted oil well. It is assumed that the pipe diameter is the same in both situations. The oil properties are considered as follows: the density $\rho_l = 800kg/m^3$, the surface tension $\sigma < 50mN/m$ ($\sigma_{field} \approx 30mN/m$), and the viscosity $\mu_l > 1mPa.s$ ($\mu_{field} \approx 5mPa.s$). At conditions where gas-lift is applied in the bubbly flow regime, the liquid input conditions are $U_{sl} \approx 1m/s$. Large bubbles being injected via a gas-lift valve in practice, $0 < \frac{D_b}{L} < 1$ in the field conditions.

The laboratory pipe used in our investigation has a diameter $D_p = 72mm$. This value corresponds to typical gas-lift conditions ($L_{Lab} \approx L_{field}$). The density of the liquids are also similar in the laboratory and in the field ($\rho_{Lab} \approx \rho_{field}$). The equality of Reynolds number Re_{sl} gives either a requirement on the viscosity or the liquid input:

$$\frac{U_{sl,Lab}}{\mu_{Lab}} \approx \frac{U_{sl,field}}{\mu_{field}}. \tag{2.15}$$

Considering the equality of the densitometric Froude number Fr_{sl}, we obtain

$$U_{sl,Lab} \approx U_{sl,field}. \tag{2.16}$$

To properly scale the Weber number We, we obtain for the surface tension

$$\sigma_{Lab} \approx \sigma_{field}, \tag{2.17}$$

and for the bubble size

$$D_{b,Lab} \approx D_{b,field}. \tag{2.18}$$

For practical reasons a large part of our experiments will be carried out with water-based mixtures ($\mu_{Lab} = 1mPa.s$ and $55mN/m < \sigma_{Lab} < 72mN/m$). For this liquid viscosity value, it is not possible to scale both the Froude number and the Reynolds number (equations 2.15 and 2.16). Therefore, to validate these measurements we will also report gas-lift experiments at larger liquid viscosity by using a solution of water and 40% glycerol, corresponding to $\mu_{Lab} = 4.6mPa.s$ and $\sigma_{Lab} = 67mN/m$. These liquid properties will permit to properly scale both the Froude and the Reynolds number.

In the present study, we are in particular interested in the effect of the bubble size on the gas-lift technique. To vary independently the bubble size D_b in the laboratory we select the non-finely dispersed bubbly flow conditions, for which bubble break-up due to turbulence is negligible. With our liquid properties the condition for non-finely dispersed bubbly flow typically corresponds to $U_{sl} < 1m/s$. Our experiments will therefore be conducted at low to moderate liquid input conditions.

Also the dimensionless initial and boundary conditions should be the same in the laboratory model. We will use a typical gas-lift injector generating large bubbles from the side of the pipe as a reference case. The effects of the initial bubble distribution and size on the gravitational pressure gradient will be studied by varying the bubble injector configuration. More details about the bubble injectors will be given in section 3.1.

2.4 Open questions

At conditions corresponding to gas-lift operations, the Reynolds number based on the liquid input is moderate ($Re_{sl} \approx 10000$). The bubbles are generated via a large nozzle valve in practice, and the tube diameter is typically $D_p \approx 10cm$. Although a number of experimental investigations have reported local measurements of the void fraction and velocity profiles in vertical bubbly pipe flows (Serizawa *et al.*, 1975; Liu, 1993a; Rivière and Cartellier, 1999; Mudde and Saito, 2001), only a few experiments reported in literature are comparable with gas-lift conditions, corresponding to moderate liquid input flow with large bubble size values. The existing studies on the gas-lift efficiency did not investigate the effects of the bubble size.

The aim of this thesis is to study the effects of bubble size and bubble injector changes on the gas-lift efficiency at low to moderate liquid input conditions. We are in particular interested in the effects of bubble size on the gravitational pressure gradient. In bubbly flow the bubble size is expected to affect the local flow structure through the bubble relative velocity (see section 2.1.2) and the bubble transverse distribution (section 2.1.3). This in turn will have an effect on the gravitational pressure drop associated with given mean flow conditions. Also, the bubble size might have an effect on the flow pattern boundary between bubbly flow and slug flow, as observed in small pipe diameter experiments (Song *et al.*, 1995; Cheng *et al.*, 2002).

The low liquid input conditions associated with the gas-lift application might lead to a liquid down-flow in the near-wall region. This effect was observed in large diameter and low liquid input bubbly pipe flows (Mudde and Saito, 2001). Such low liquid input conditions suggest the bubbly flow to be in the non-finely dispersed regime (section 2.1.1). The bubble break-up effects are therefore negligible, and the bubble size is essentially determined by the bubble injector configuration and the gas input conditions. In this regime it is interesting to investigate the effect of the bubble initial distribution, the bubbles being injected from the side of the pipe in practice. Another question is whether the wall peaking radial profile of void fraction is observed at low liquid input, moderate pipe diameter flow conditions. Such peaks of void fraction have been mainly reported for small diameter pipes when operating at large liquid input conditions (Serizawa *et al.*, 1975; Liu, 1993a). The possible presence of a down-flow at the wall could also affect this void fraction profile.

To first understand the overall effect of bubble size and bubble injector configuration on the gas-lift efficiency we will investigate the gas-lift liquid circulation and the gas-lift pressure drop associated with different bubble injectors, generating significantly different bubble size and bubble initial distribution. This will permit to infer the net effect of a reduced bubble size on the gas-lift efficiency. Particularly, we will investigate how the flow pattern is affected by the bubble size configuration. Based on these observations a first model attempt using the drift-flux model will be developed.

For investigating in details the contributions due to the bubble relative velocity, the bubble radial distribution and the phase velocities on the gravitational pressure gradient, these quantities have to be measured. Based on such measurements the weighted mean drift velocity and distribution parameters of the drift-flux model can be directly computed, allowing for quantifying the contributions due to the relative

motion and to the radial distribution effects respectively.

Local measurement techniques have therefore to be used. Since we expect to observe a down-flow of liquid near the wall for low liquid input flow conditions, the technique used for the liquid velocity should allow for the velocity sign determination. To that purpose Laser Doppler Anemometry (LDA) using a pre-shifting Bragg Cell is potentially appropriate, with the advantage of being non-intrusive. We therefore will investigate the feasibility of liquid velocity measurements by using LDA in large void fraction bubbly flows. The technique used for bubble size determination should allow measuring in a poly-disperse medium, since the distribution of bubble size resulting from a gas-lift valve can be expected to be relatively large. To that purpose, we will investigate the possibility of measuring the bubble size and velocity by using a four-point optical fibre probe selecting the bubbles rising at the axis of the probe.

As mentioned in section 2.1.3 the transverse migration of a single bubble is observed to be due to a critical bubble deformation, resulting in a modified lift force (Tomiyama, 1998). Although this effect correctly describes the transverse migration of multiple bubbles in a shear flow, it is not clear whether the same mechanism is responsible for these effects at large void fraction flow conditions, and additional effects might be observed in this situation (Tomiyama *et al.*, 2002b). To investigate this bubble shape effect on the transverse migration in large void fraction bubbly pipe flows, the bubble shape and orientation would need to be measured. A technique for extracting bubble shape and orientation information from the signal provided by a four-point probe will be developed and validated. This technique will be applied to our bubbly pipe flow four-point probe data to infer the bubble shape and orientation in bubbly pipe flow conditions.

Another equally important question for gas-lift predictions is whether the effects of bubble size and liquid input can be predicted with a model. Such a numerical model would potentially provide a mean of up-scaling our results to different flow conditions. Based on the Euler-Euler modelling approach we will develop a simplified model for predicting the void fraction and velocity profiles associated with bubble size changes. We will compute the associated distribution parameter values and compare the numerical results with our experiments.

Chapter 3

Experiments

3.1 Experimental set-up

3.1.1 Airlift and convected bubbly pipe flow

The experimental set-up used in this study is made for generating an upward gas-liquid pipe flow while operating in the bubbly and slug flow pattern in gravity-driven flow conditions. The experimental set-up is sketched in figure 3.1.

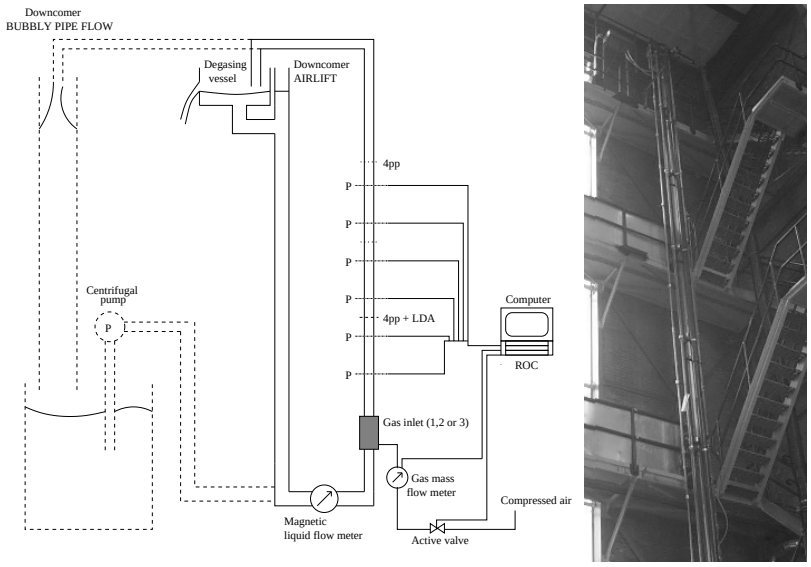

(a) (b)

Figure 3.1: (a) Experimental set-up: upward bubbly pipe flow (right); down-comer for the airlift experiments (middle) and down-comer equipped with a centrifugal pump (left). The height is $H = 18m$ and the diameter $D_p = 72mm$. (b) Upper part of the experimental set-up.

The height of the pipe is $H = 18m$ and the diameter $D_p = 72mm$. This experimental facility can be used in two different configurations by changing the down-comer part. In these two situations the same Perspex pipe is used for the upward bubbly flow (on the right-hand side of figure 3.1.a). In the airlift situation the liquid flow is only originating from the difference of density between the upward bubbly pipe flow and the returning liquid flow in the down-comer (in the middle of figure 3.1.a). In the second configuration (the forced bubbly flow situation) the down-comer is equipped with a centrifugal pump (Schmitt centrifugal pump, type T190) and a 250 litres vessel (on the left-hand side of figure 3.1.a). The flow in the down-comer is calmed prior to entering in the re-circulating vessel to prevent any variation in the liquid level and to avoid the presence of bubbles in the re-circulating vessel. This flow configuration allows investigating any combination of gas and liquid superficial velocities.

3.1.2 Global measurement techniques and controls

The liquid flow rate was measured with magnetic flow meters. At low liquid flow rates ($U_{sl} < 0.1m.s^{-1}$) a Rosemount Flowtube 8732C magnetic flow meter was used and for moderate flow rates ($0.1 < U_{sl} < 0.4m.s^{-1}$) an Endress+Hauser Promag50 magnetic flow meter was applied. The gas flow rate was measured with a gas mass flow meter Brooks 5861S, providing the gas volumetric flow rate at atmospheric pressure. The pressure was measured at two-meter intervals along the pipe with pressure transducers flush mounted to the wall, at $h = 2, 4, 6, 8, 10$ and $12m$ (AE sensors, type ATM). The range of calibration was 0 to 2 bars relative pressure, providing an inaccuracy of less than 0.5 % for the whole range of pressures investigated. A remote operations controller (ROC, Fisher Rosemount) was used with a $100MHz$ PC for sending and receiving information from the set-up. The ROC could also be used to control the gas mass flow rate by means of a control valve situated upstream from the flow meter.

3.1.3 Bubble generation

Four different inlet devices were used in this study (figure 3.2 and 3.3):

1- An annular porous inlet generating small bubbles with a diameter between 1 and $8mm$ (inlet 1 in figure 3.2). The bubbles are generated symmetrically from a horizontal circular porous metal plate (Mott metallurgical corporation, thickness $3mm$). This circular porous plate is welded onto a gas-distributing chamber to redistribute the gas pressure and prevent any preferential site bubble generation problem. The pore diameter is $10\mu m$ and the area $1000mm^2 \pm 50mm^2$.

2- A vertical long porous inlet, made of the same metal porous material, of $1cm \times 10cm$ and oriented parallel to the pipe wall (inlet 2 in figure 3.2). This injector generates small bubbles with a diameter between 1 and $10mm$. The distance separating the porous plate from the pipe wall is $15mm$. The bubbles are generated perpendicularly to the liquid flow direction. To achieve the same initial bubble size from the annular porous inlet and the long porous inlet, the

same porous material area is used for generating the bubbles. The long porous inlet can therefore be used to investigate, in particular, the effect of the bubble initial distribution on the flow development.

3- A large nozzle inlet, made of two $3mm$-diameter nozzle inlets attached to the pipe wall generating large bubbles, with a typical diameter between 5 and $20mm$ in water (inlet 3 in figure 3.2). This injector corresponds to gas-lift valves as used in practice: we have taken such an injector and glued the injector head part onto a copper tube, connected onto the air input.

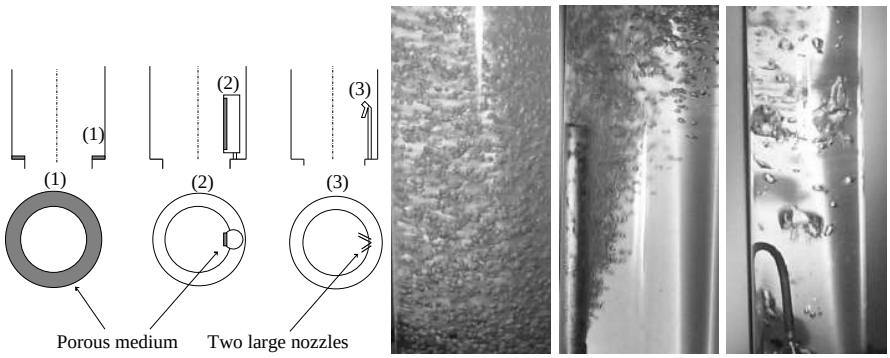

Figure 3.2: Left: Top and side views of the 3 inlets: (1) Annular porous medium inlet, (2) Long porous medium inlet, and (3) Large nozzle. Right: photos of the bubble distribution in the mixing zone of inlet (1), (2) and (3).

4- A mixing box making use of a large area of low pore size material for generating sub-millimeter size bubbles. A number of ceramic plates of $360cm^2$ area (Aquatech, diffuser type 600) are used. The liquid injection was distributed below the plates in a mixing box. Various plates geometrical configurations were tested to optimise the bubble mixing conditions and to minimise the bubble size. A configuration of four porous plates, as sketched in figure 3.3, was found to offer the best mixing conditions. The equivalent area of porous material is therefore $4 \times 360cm^2$, with an average pore size of $0.3\mu m$. This results in bubbles with a spherical equivalent diameter ranging from $100\mu m$ to $2mm$ for low gas input, and up to $5mm$ for the largest gas input conditions. Only pressure measurements are carried out with this injector, since the local measurement techniques used in the present study could not be applied to sub-millimetre size bubbles.

Each injector could be connected to the bottom of the pipe flow depicted in figure 3.1. The injectors (1) to (3) could also be used for airlift experiments, to quantify the changes in liquid output due to bubble injector changes. By using the injector (1), (2) and (3), we also measure the radial distribution of gas fraction with single-optical fibre probes at four locations downstream from the inlet: $h = 4$; 6, 8 and $12m$, i.e. $h/D_p = 55$; 83; 110 and 166. The bubble size resulting from these

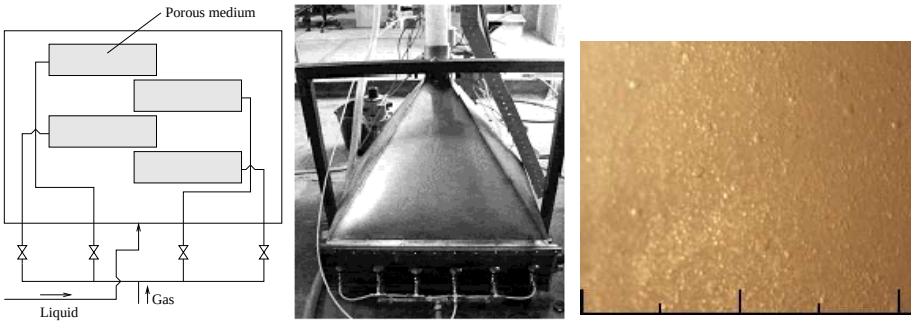

(a) Top view representation (b) Box (c) Typical bubble size

Figure 3.3: Sub-millimetric bubble injector, consisting in a mixing box with a large area of ceramic porous material. (a) Porous plates arrangement in the mixing box, (b) a photo of the mixing box placed at the bottom of the pipe flow, (c) typical bubble size resulting from the box. The width of the photo in (c) is $2cm$.

injectors was first determined from photos. Since it was essential to reduce light refractions, the well-known technique of applying a square box around the pipe was used.

To measure the bubble velocity and the bubble chord length, we use two four-point optical fibre probes. The four-point probes can be positioned at $h = 5m$ and $13m$, i.e. $h/D_p = 70$ and 180. This bubble velocity and size measurement technique will be described and assessed in section 3.4. To investigate the coupling between the gas and the liquid velocity, we will also measure the liquid velocity. For this purpose we will use Laser Doppler Anemometry in the backscatter mode. Ultimately, both a four point and a LDA probe will be positioned at $h = 5m$, i.e. $\frac{h}{D_p} = 70$ on our experimental set-up. The feasibility of liquid velocity measurements in our large void fraction bubbly flow conditions has however to be assessed as well. This is the topic of the coming section.

3.2 Feasibility of LDA measurements in high void fraction bubbly flow*

3.2.1 Introduction

The possibility of measuring the continuous phase velocity in high void fraction bubbly flows is of practical importance for the model validation and the optimisation of a number of industrial processes. Applications involving stirred vessels, reactors or pipe flows at 20% void fraction are far from being completely described. The use of numerical simulation for such problems is a challenging issue: Direct Numerical Simulation is computationally too expensive for large scale problems, while averaging approaches, such as two fluid Euler-Euler models, need accurate closure models for interfacial forces and dispersed phase turbulence modification. Devoted experiments in bubbly flow are therefore needed for the development of proper simulation models. An interesting application can be found in vertical bubbly pipe flows. The transverse profiles are strongly affected by the magnitude of the radial forces. Depending on the bubble size and turbulence conditions, the well-known wall peaking and core peaking void fraction profiles are observed (Liu, 1993a). In this experimental investigation, we want to measure the liquid velocity associated with these various bubble size and liquid input conditions.

At high void fraction with low liquid input flow conditions, e.g. in gravity-driven bubbly flow, the use of Hot Film Anemometry is questionable, due to the associated difficulty for discriminating between phases (Farrar *et al.*, 1995). Although the use of HFA had been shown to be suitable for individual bubble wake dynamic investigations (Ellingsen *et al.*, 1997; Larue de Tournemine *et al.*, 2001), the study of returning flows would be difficult due to its working principle, based on forced thermal convection. Two point HFA would then be needed to characterise the flow direction, thus increasing intrusiveness effects. Laser Doppler Anemometry had already been found to provide meaningful data in bubble columns when using the technique in the backscattering mode (Mudde *et al.*, 1997), particularly for measuring near the wall boundary, where the data rate was high. Groen *et al.* (1999) have shown that bubble scattering (i.e. velocity realisations associated with a bubble passage) was only occurring marginally.

In this section the results of a feasibility study to use LDA in a high void fraction bubbly flow are reported. For that purpose we used a stirred vessel, in which both the void fraction and the distance between sending and receiving optics could be varied. The diagnostic testing procedure described in Van Maanen (1999a) has been applied to the sampled data. The raw velocity data are first presented to illustrate the clear distinction between single and two phase flow signals. The time interval distributions, velocity probability distributions and signal-to-noise ratio (SNR) are determined. First, the experimental set-up arrangement is described. Next the results concerning the feasibility of the measurements are presented. The physical meaning and recoverability of the experimental results is then outlined, and some conclusions are drawn.

*See also: S. Guet, H.R.E. van Maanen, & R.F. Mudde. Paper 3.1 presented at the 11^{th} *International symposium on applications of laser techniques to fluid mechanics*, Lisbon, 8 – 11 July 2002.

3.2.2 Experimental arrangement

The experimental set-up is a stirring vessel of $270mm$ diameter, equipped with an impeller (figure 3.4). The impeller consists of four blades of $121mm$ diameter. The rotational speed can be varied from 0 to $700rpm$. A porous bubble inlet is inserted near to the LDA measurement volume, corresponding to the long porous inlet (2) sketched in figure (3.2). The resulting bubble size is between 2 and $10mm$. By controlling the gas flow rate through the porous bubble inlet, the void fraction in the bubble layer can be changed. The use of an optical glass fibre probe positioned near to the LDA measurement volume allows for the determination of the void fraction conditions. Bubbly flow layers of $30mm$ and $50mm$ thick are investigated, whereas the void fraction is varied from 0 to 20%.

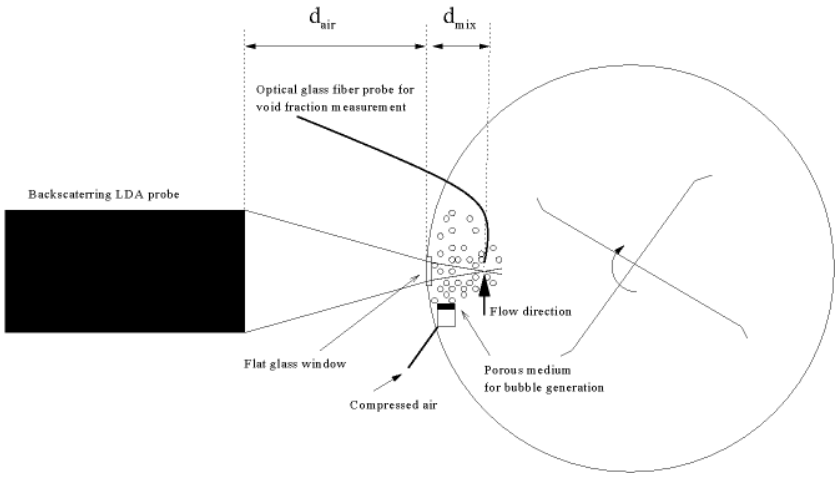

Figure 3.4: Experimental set-up used for the LDA feasibility study.

The LDA consists of a FiberFlow probe of $27mm$ diameter from Dantec (model $61X35$). This probe is positioned on a three-axis traversing equipment. It is adjusted to measure through a flat glass window (figure 3.4), and the effect of the bubbly flow layer thickness (d_{mix} in figure 3.4) on the data quality and rate can be studied by adjusting the measuring distance in air. The LDA is running in back-scattering mode, and the tangential component of the velocity is investigated. A $2W$ (all-lines) Coherent Argon - Ion water-cooled laser is used (Spectra physics Stabilite 2017), with $514.5nm$ wavelength. The measurement volume dimensions in water are $0.1 \times 3mm$, the fringe spacing is $5.48\mu m$. The focal length is $160mm$ in air. The bursts are processed with a Dantec FVA processor (model 58N20).

The void fraction is measured near to the LDA measurement volume with an optical fibre probe, as described in section 3.4.4.2. The signal is sampled on a PC at a frequency of $20kHz$.

3.2.3 Results

3.2.3.1 Signal modification in bubbly flow compared to single phase flow

The bubbles introduce 'drop-outs' in the signal. This can clearly be recognized in the time traces (figures 3.5.a, 3.6.a and 3.7.a, in which the symbols d_{mix} and ϵ denote the measuring distance in bubbly flow and the mean void fraction). However, in between the bubbles information about the shorter time scales is still available. Also, the bubbles introduce a change in the time interval distribution, which is similar to velocity bias (figures 3.6.b and 3.7.b compared to 3.5.b).

The deviation from the situation corresponding to a random distribution of scattering particles, as demonstrated in Van Maanen (1999a), is not due to velocity

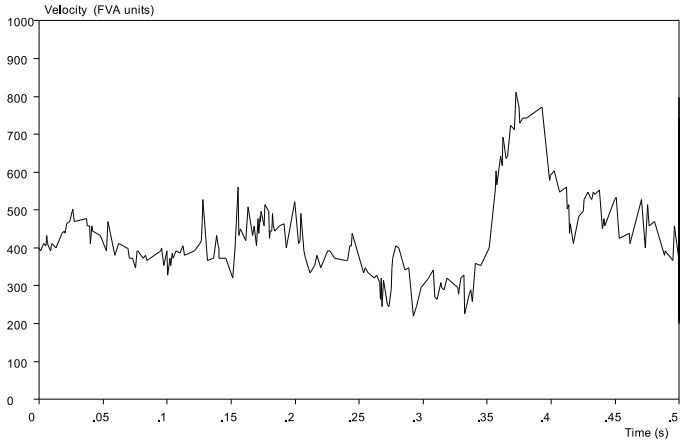

(a) Time trace

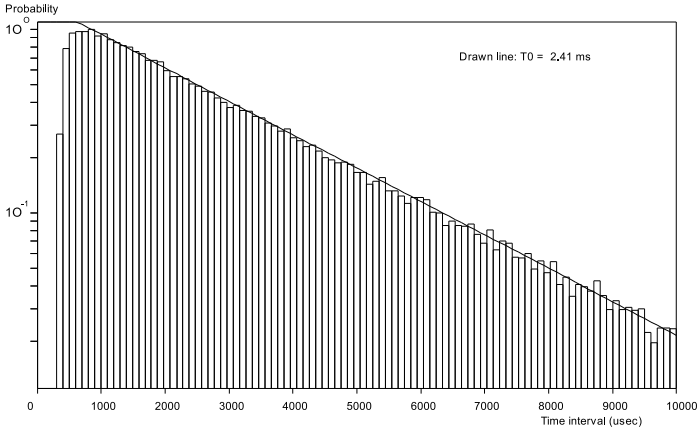

(b) TID

Figure 3.5: Time traces and Time Interval Distribution (TID) of the LDA signals at zero void fraction and $d_{mix} = 50mm$.

bias in that particular situation. The situation of zero void fraction (figure 3.5.b) shows an acceptable time interval distribution, corresponding to a meaningful measurement (on a semi-log scale, the time interval distribution should be linear for a random distribution of scattering particles). This is explained as follows: the bubbles are reducing the number of observations for the intermediate time scales, therefore contributing to the observed concavity deviation. A closer analysis of the optical fibre signal showed that it is the case: the time residence of the bubbles in the optical fibre probe or, similarly, in the measurement volume, is in the range of 1 to $10ms$, thus contributing to the intermediate time scales. The fact that the concavity in the time interval distribution of the measurements is increasing with the void fraction (figure 3.7.b compared to 3.6.b) confirms that this is indeed due

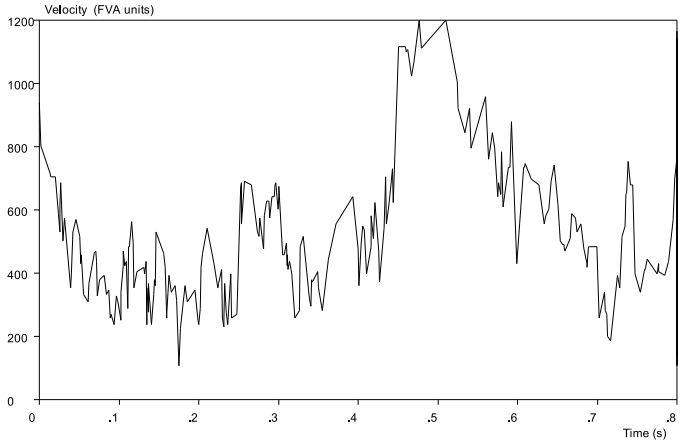

(a) Time trace

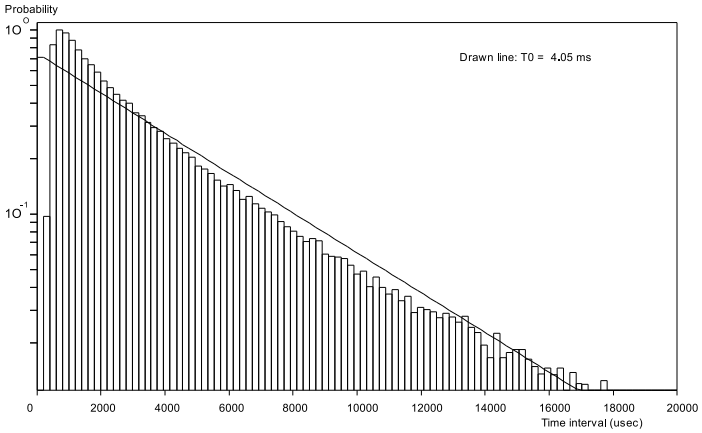

(b) TID

Figure 3.6: Time traces and Time Interval Distribution (TID) of the LDA signals at $\epsilon = 0.05$ and $d_{mix} = 50mm$.

to the bubble residence times. Similar deviations are reported by Mudde and Saito (2001).

In figures 3.8(a) and 3.9(a), the temporal auto correlation function clearly points to a decreased SNR for increased void fraction. However reasonably good Signal to Noise Ratios (> 3) are found for all the flow conditions investigated. This lower value compared to single-phase flow can be compensated by measuring longer. The probability density function of velocity is also showing coherent properties for both low and high void fraction values (figures 3.8.b and 3.9.b). From a signal diagnostic perspective, such measurements are therefore feasible. In Appendix A, we report some results on the feasibility of computing the turbulence spectrum from the collected measurements.

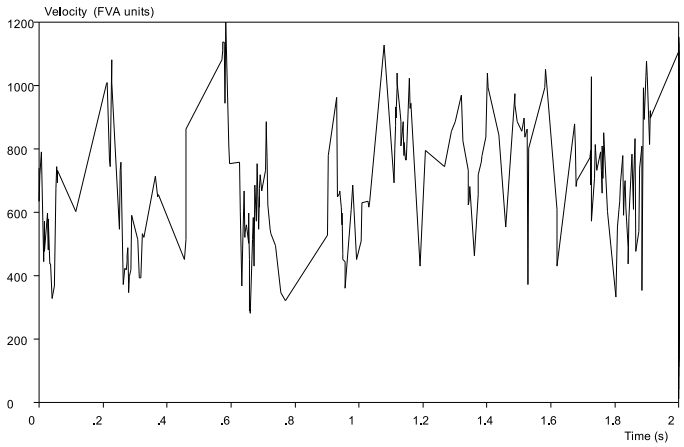

(a) Time trace

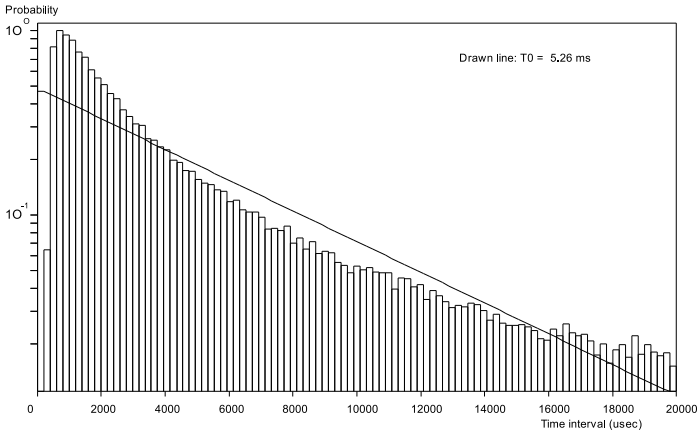

(b) TID

Figure 3.7: Time traces and Time Interval Distribution (TID) of the LDA signals at $\epsilon = 0.2$ and $d_{mix} = 30mm$.

3.2.3.2 Periodic components

A periodic component in the velocity can be observed in single-phase flow stirred vessels. Van der Molen and Van Maanen (1978) reported that this effect was significant for $\frac{r}{r_{blade}} < 1.5$, due to the dominance of trailing vortices from the impeller blades (r is the radial position of the LDA measurement volume and r_{blade} is the blade radius). At large rotational speed ($\omega \approx 670rpm$, i.e. a blade passing frequency of $45Hz$) and for a bubbly flow layer of $30mm$ ($\frac{r}{r_{blade}} \approx 1.4$), the enlarged time scale temporal auto-correlation functions of figure 3.10(a) and 3.11(a) for both low and high void fraction show quasi-periodic components (figure 3.10.b and 3.11.b).

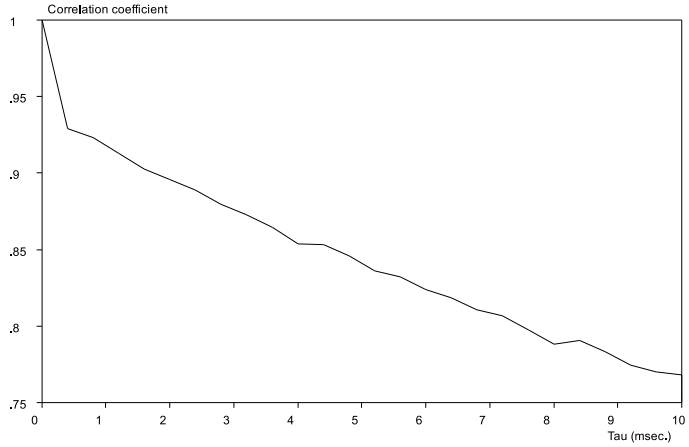

(a) ACF

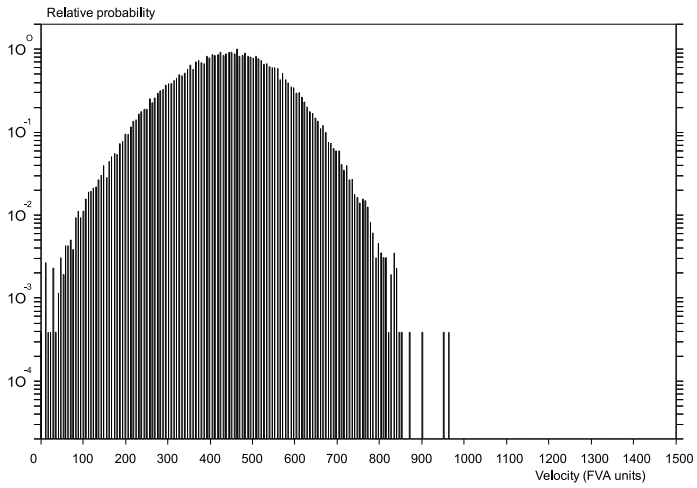

(b) PDF

Figure 3.8: Auto correlation function (ACF) and logarithmic velocity distribution of an LDA signal at $\epsilon = 0$ and $d_{mix} = 50mm$.

The frequency associated with those oscillations is of the order of $2Hz$. These low frequency components are attributed to some large-scale re-circulations in the vessel and some resonance effect at this large rotational speed. In high void fraction conditions, the auto correlation function shows a decaying periodic component (figure 3.11.b). The rotational speed being the same, the frequencies associated with the two measurements are similar (figure 3.11.b compared to figure 3.10.b). The fact that such components can be retrieved at 20% void fraction enhances the trustworthiness of the results.

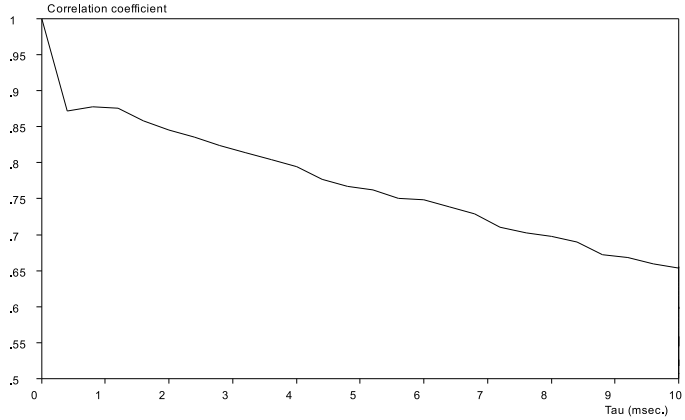

(a) ACF

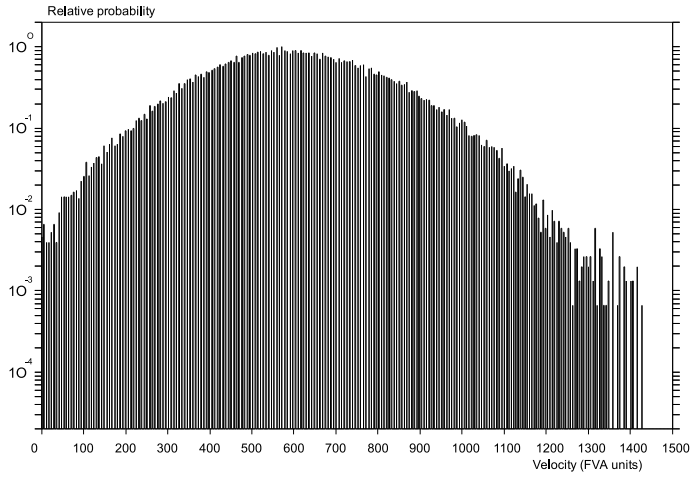

(b) PDF

Figure 3.9: Auto correlation function (ACF) and logarithmic velocity distribution of an LDA signal at $\epsilon = 0.2$ and $d_{mix} = 30mm$.

3.2.4 Conclusion of the feasibility study

The goal of this investigation was to study the feasibility of backscatter mode LDA measurements in a complex, packed bubbly flow. Experimental tests performed in a stirred vessel in which bubbles were injected from a porous material showed that such measurements are feasible. The diagnostic procedure described in Van Maanen (1999a) has been applied to the raw data. The main conclusions are the following:

- The bubbles introduce a change in the time interval distribution, which is similar to velocity bias. However, in this case the concavity in the Time Interval Distribution is physical. The liquid velocity distribution confirmed that physically reliable measurements were performed.

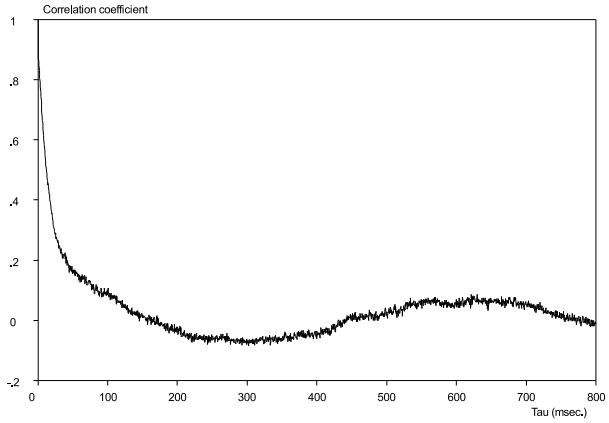

(a)

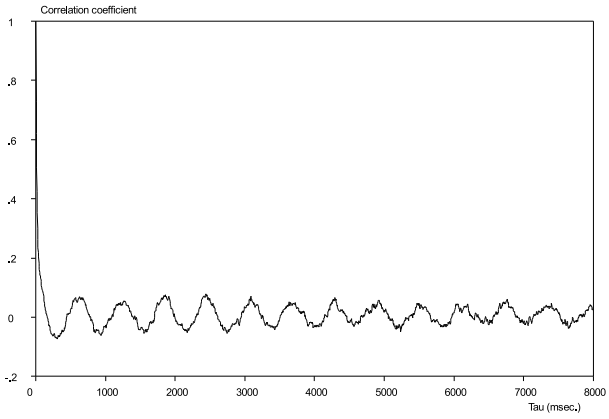

(b)

Figure 3.10: Autocorrelation function of a 4.7% void fraction test, bubble layer thickness of $30mm$. In (b) the time scale is enlarged to illustrate the periodic component induced by the blades.

- The auto correlation functions show a reasonably good Signal-to-Noise Ratio regarding the flow conditions.
- The diagnostic procedure and the turbulence fitting method developed by Van Maanen (1999a) are found to be suitable for such a complex bubbly flow situation.

It can be concluded that the application of LDA in high void fraction bubbly flow is feasible, provided that the distance between the measurement volume and the transmitting and receiving optics is small enough to obtain sufficient Doppler signals from the liquid to allow further processing. In this case $50mm$ showed to be feasible for void fractions of up to 10%. With a bubble layer thickness of $30mm$, it was possible to measure at void fraction values of up to 20%. The next step is to

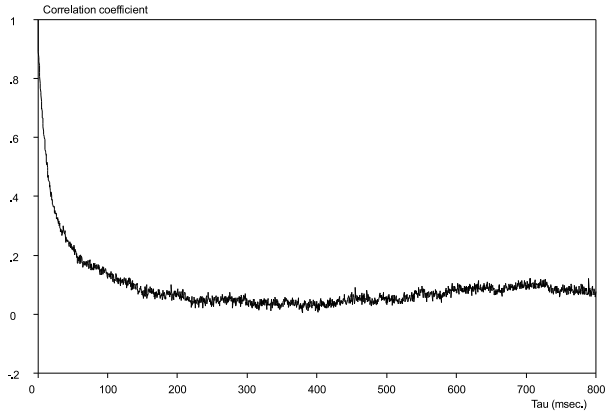

(a)

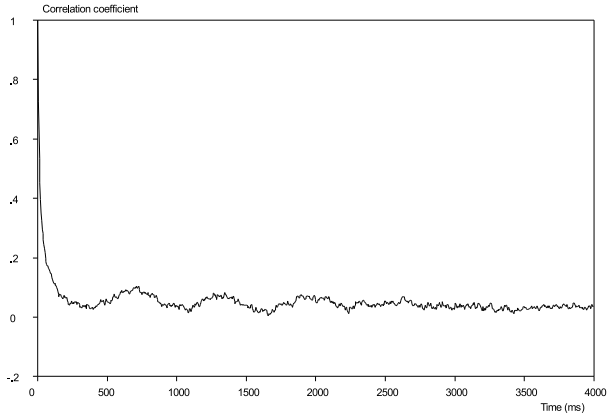

(b)

Figure 3.11: Autocorrelation function of a 20% void fraction test, with $d_{mix} = 30mm$ and $\omega = 670rpm$. In (b) the time scale is enlarged to illustrate the periodic component induced by the blades.

measure the liquid velocity in our high void fraction, vertical bubbly pipe flow of $36mm$ radius.

3.3 Bubbly pipe flow LDA measurements

3.3.1 Equipment

The LDA equipment used for the pipe flow measurements is based on the same Argon-Ion laser source and LDA processor as for the stirred vessel tests (Spectra Physics Stabilite 2017 laser source with a Dantec FVA 58N20 processor). A $14mm$ diameter FiberFlow back-scattering probe from Dantec (model 60X17) was used for the pipe flow measurements. The probe was inserted into a $27mm$ diameter probe holder, and could be traversed in the radial direction (figure 3.12).

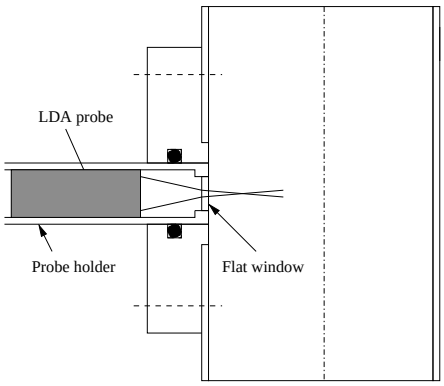

Figure 3.12: Sketch of the implementation of our $14mm$ diameter back-scatter probe on the pipe flow, by using a probe holder.

To avoid any beam distortion, the probe holder was fixed perpendicularly to the pipe and equipped with a $16mm$ diameter, $1mm$ thickness flat glass window adjusted flush to the pipe wall. The $514.5nm$ wavelength was used for measuring the axial velocity component. The measurement volume dimensions in water were $0.122 \times 1.52mm$. Hollow glass spheres particles of 10μm diameter (Sphericel, $\rho_l = 1090Kg.m^{-3}$) were used for light scattering. The measuring probe (including the probe holder, traversing equipment and support) was placed on a measurement section of $600mm$ length and $72mm$ diameter, which could be inserted on the experimental set-up at a height $h = 5m$, i.e. $\frac{h}{D_p} = 70$. To check the validity of the measurements, the diagnostic testing procedure proposed by Van Maanen (1999a) and applied in the previous section on our preliminary tests was also carried out on the pipe flow measurements. In this section typical low liquid input pipe flow diagnostic results that revealed a behaviour which deviates from that obtained during the stirred vessel tests are presented.

3.3.2 Bubbly pipe flow-LDA signal testing

The results for the time trace, time interval distribution and temporal autocorrelation of the pipe flow signals were comparable with the stirred vessel results. The PDF of the velocity was however having different properties: in figure 3.13 we present a typical PDF of the measured velocity for our pipe flow experiments when using our large nozzle inlet. Bubbles of spherical equivalent diameter of up to $D_b = 15mm$ were observed during this experiment. A clear difference with the PDF obtained during the stirred vessel tests can be observed. The histogram is not symmetric in this case. This effect is due to the non-zero relative velocity between the two phases in the measurement direction, which in turn generates a second peak tendency of the probability density function at the bubble velocity value. Similar results are reported for LDA measurements in bubble columns by Mudde *et al.* (1997).

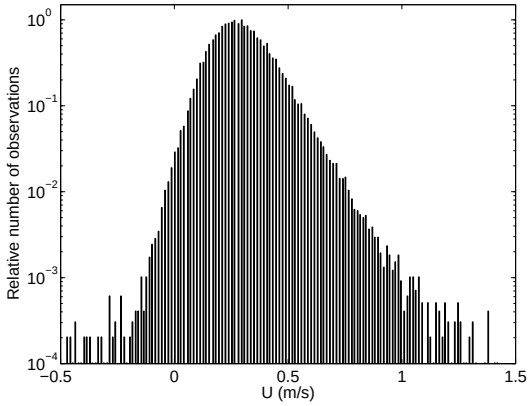

Figure 3.13: Logarithmic velocity distribution of an axial velocity component measurement in the pipe flow for $d_{mix} = 24mm$, $\epsilon = 0.05$, $U_{sl} = 0.35m/s$ and $D_b = 5 - 15mm$.

To investigate a potential velocity bias due to this effect, the Time Between Data correction (TBD) for the mean velocity calculation was tested on the measurements. We compared $U_l = \frac{\Sigma U_n}{N_{mes}}$ to:

$$U_{l,tbd} = \frac{\Sigma U_n (t_{n+\frac{1}{2}} - t_{n-\frac{1}{2}})}{T_{mes}}, \tag{3.1}$$

in which U_n is the measured velocity realization collected at time t_n. We used $t_{n+\frac{1}{2}} = \frac{t_n + t_{n+1}}{2}$, and T_{mes} is the total measurement time. In figure 3.14, we compare the two approaches: in most of the conditions, this correction did not change significantly the time average velocity evaluation. In this figure, two conditions are plotted, corresponding to similar flow input and void fraction ($U_{sl} = 0.35 m.s^{-1}$, $\epsilon \approx 0.05$). Only the bubble size conditions are different: experiment (1) corresponds to large bubbles ($D_b \approx 5 - 15mm$) and experiment (2) is associated with millimetre size bubbles ($D_b = 2 - 5mm$).

The bubble relative velocity increases with bubble diameter. Therefore the TBD correction can be expected to make a larger difference for larger bubbles. This is indeed the case (figure 3.14). This correction to the mean values is however not a crucial point in view of the measurements accuracy. These low values of the TBD correction confirm the validity of the time average velocity measurements. Only when the data rate was decreasing to values below $10 - 20Hz$, the two calculation techniques were providing different results. Those measurements will be disregarded in our measurement analysis.

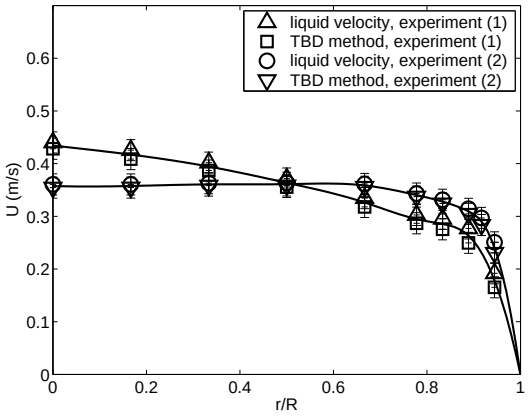

Figure 3.14: Comparison between the mean liquid velocity obtained by ensemble average and by using the Time Between Data (TBD) method for two different bubble size experiments: (1) large bubbles, (2) small bubbles.

The data rate was decreasing significantly with $d_{mix} = R - r$ during the pipe flow measurements (figure 3.15). As pointed out by Mudde *et al.* (1998), the data rate decreases exponentially with the measuring distance d_{mix} in bubbly flows. However, in the near wall region the data rate was generally increasing with d_{mix}, due to the increase of the scattering particle passage frequency with mean velocity.

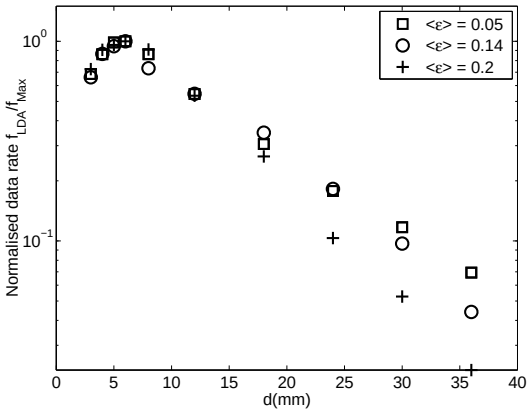

Figure 3.15: LDA data rate as a function of the bubbly flow layer measuring distance d_{mix} and for various void fraction conditions. The LDA data rate f_{LDA} is normalized by its maximum value f_{Max}.

3.3.3 Conclusion

We investigated the possibility of LDA measurements of the axial velocity in a low liquid input vertical bubbly pipe flow. The main particularity of these measurements is the presence of a second-peak tendency in the velocity probability density function. This is due to the velocity realisations in the wake of the bubbles, associated with the (non-zero) relative velocity between the bubbles and the liquid in the measurement direction. This effect was more pronounced at increased bubble size. However a comparison of the ensemble average and TBD correction method showed that this has a negligible effect on the time average velocity estimates in our flow configuration. The mean liquid velocity could be estimated with a deviation of less than 5%.

3.4 Bubble velocity and size measurements with a four point probe*

3.4.1 Introduction

An important issue in understanding and modelling dense bubbly flows is the dependence of the bubble velocity on the bubble concentration. The bubble velocity plays an important role, for instance, in understanding void fraction waves and in modelling interfacial forces such as the lift and drag force. The objective of this section is to report about a technique to measure reliably the radial bubble velocity profile in an upward vertical high-void-fraction bubbly pipe flow.

The measurement of the individual bubble velocity in a high-void-fraction bubbly flow ($\epsilon > 0.1$) is a complicated task: the opacity of the mixture often excludes the use of camera-based techniques. In an air-water bubbly flow the air (inside a bubble) can be distinguished locally from the surrounding water by using an optical fibre. The fibre is cut with a particular shape and the difference in refraction index between air and water is employed (Cartellier, 1992; Cartellier and Barrau, 1998a,b; Barrau *et al.*, 1999; Mudde and Saito, 2001). The light signal (reflected from the glass-air or the glass-water interface) is collected with a photo multiplier. A typical voltage signal is shown in figure 3.16. T_{rise} is the fibre piercing time, T_{gas} is the time spent by the fibre in the air inside the bubble and T_{wet} is the wetting time of the fibre (when the bubble has passed the probe sensitive part). The local void fraction can be determined by imposing a threshold value to the collected signals of many bubbles and computing the relative time spent in the gas phase. Contrary to resistivity probes the relevant times can unambiguously be determined, since $T_{wet} + T_{rise} << T_{gas}$ and no advanced adaptable threshold method (Liu, 2002) is

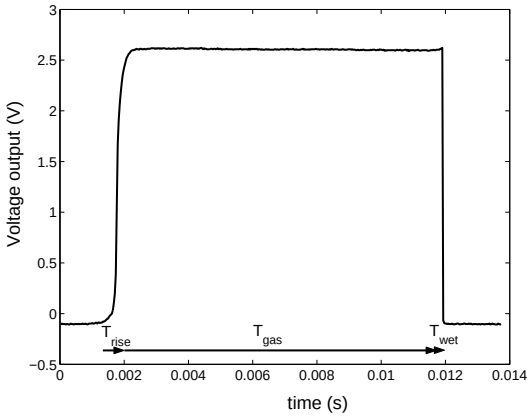

Figure 3.16: Typical signal obtained from a single fibre probe with T_{rise}, T_{gas} and T_{wet}.

*See also: S. Guet, R.V. Fortunati, R.F. Mudde, & G. Ooms. (2003). *Part. and Part. Syst. Char. J.*, vol 20, pp 219-230.

needed in the case of optical fibre probes. In moderate-void-fraction bubbly flows dual-fibre probes are known to provide meaningful results for the measurement of individual bubble velocities. However, serious experimental difficulties occur at high-void-fraction conditions. For instance the uncertainty that the two fibres pierce the same bubble (bubbles are known to exhibit spiralling and zigzagging motions) and the difficulty to relate the measured bubble chord length to the maximum vertical chord length are known problems of the dual-fibre probes. The lack of information regarding how a bubble is approaching the two-point probe and where the bubble is pierced makes it difficult to apply to poly-disperse systems or non-isotropic flows presenting transverse gradients, such as pipe flows. Furthermore, dual-fibre probes do not provide information about the angle of the bubble motion with respect to the vertical axis.

The objective of this section is to investigate the possibility to measure the individual bubble velocity and bubble chord length in a high-void-fraction bubbly flow with a preferential direction by using an arrangement of four optical fibres. A time-of-flight procedure is used, based on a criterion for selecting the bubbles travelling along the axis of the probe. The principle of the four-point probe measurements will first be explained in section 3.4.2, with special emphasis on the bubble selection criterion used. Then, in section 3.4.3, we report about the bubble-probe interaction, investigated by means of single-bubble measurements and by comparing the four-point probe measurements with CCD-camera recordings. Next the sensitivity of the results with respect to the bubble selection criterion is discussed for a vertical pipe with a high void fraction and a low liquid flow rate in section 3.4.4. The measured bubble size and radial profiles of void fraction and bubble velocity are presented in section 3.4.5 and compared with gas flow rate measurements to investigate the reliability of the measurement results. The bubble velocity measurements are also combined with Laser-Doppler Anemometry (LDA) measurements for the liquid phase to verify the consistency of the technique with existing bubble slip velocity correlations. These results will also be discussed in section 3.4.5.4. Finally, some conclusions are drawn.

3.4.2 Four-point optical probe

3.4.2.1 Description of the probe

Each fibre consists of three layers: a quartz glass core of $200\mu m$ diameter having a refraction index of 1.45, a silicon cladding of $380\mu m$ diameter and a protective layer of Teflon of $600\mu m$ diameter. The cladding and Teflon layers are removed over the last centimetres of the probe. Each optical fibre sensitive part is shaped by over-heating it, resulting in a rounded shape glass core extremity. The light is sent into each fibre by a LED (wave length $680nm$) via standard glass fibre connectors and detected by a photodiode. The collected light is then converted into a voltage output. The use of standard fibre connectors for every connection guarantees a large signal to noise ratio output. At the start of a measurement, the LED power is automatically adjusted such that the maximum signal-output is 500mV. During the measurement the signal is subsequently amplified to deliver several Volts output. The signal is then sampled on a computer.

A sketch of a four-point probe as used in this investigation is given in figure 3.17.

The four fibres were glued together and inserted into a $6mm$ external diameter tube. This tube was then bent as depicted in figure 3.17(a).

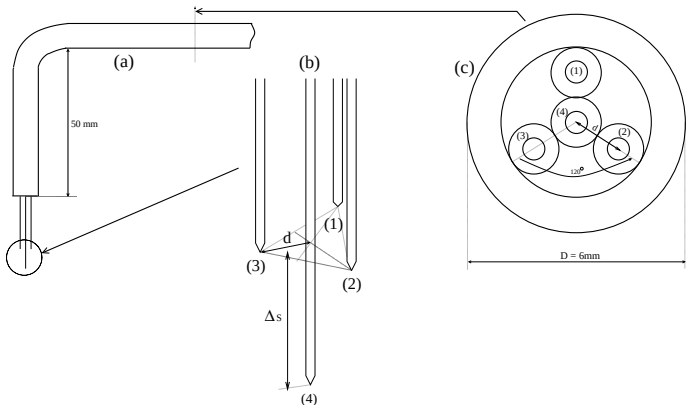

Figure 3.17: The four-point optical fibre probe used: (a) general sketch, (b) perspective view of the probe sensitive part and (c) sectional view.

The individual bubble velocity is determined by using the time of flight of the bubble between the central fibre tip (tip 4 in figure 3.17.b) and the 3 other fibre tips (1, 2 and 3) situated downstream of tip 4 (Burgess and Calderbank, 1975; Frijlink, 1987; Saito and Mudde, 2001). The vertical distance between tip 4 and the plane through tips 1, 2 and 3 is $\Delta s = 1.6 \pm 0.03mm$. The transversal distance between fibres is $d = 0.6mm$ (figures 3.17.b and 3.17.c). The signal associated with a bubble rising nearly at the axis of the central tip (4) is shown in figure 3.18. For such condition the time of flight τ is nearly equal for each of the three triangular positioned tips (1, 2 and 3). When the difference in length Δs of the central tip and the other tips is known, the absolute bubble velocity can be calculated as follows

$$U_b = \frac{\Delta s}{\tau}. \tag{3.2}$$

The bubble vertical chord length can then be determined from the time T that the central tip is present in the bubble and is given by

$$D_{bv} = U_b T. \tag{3.3}$$

Of course, the real signal obtained from a four-point probe in a dense bubble swarm is more complicated, and bubbles that do not approach the probe sufficiently close to the central axis should be filtered out from the results. An example of a signal of a bubble rising not close enough to the central axis is given in figure 3.19. A detection criterion is used to filter out the signals of such bubbles. It is based on differences in the times of flight τ_1, τ_2 and τ_3 of a bubble from the central tip (4) to the tips (1, 2 and 3), with respect to the average time of flight $\tau = \frac{1}{3}\sum \tau_i$. A bubble is selected if τ_1, τ_2 and τ_3 are not too different from the average value

$$\left| \frac{\tau_i - \tau}{\tau} \right| < \beta \quad \forall i, \tag{3.4}$$

in which i indicates tip 1, 2 or 3.

In order to compare accurately the individual times of flights, the four optical fibre signals are stored on a computer with a NI-DAQ AI-16E-4 sampling card at a sampling frequency of $f = 65kHz$ per channel. A threshold level in the signal corresponding to 10% above the voltage level in the liquid is used to extract the piercing and wetting times. For our noise level conditions and the range of bubble velocities investigated, the times of flight can be determined confidently by using such a sampling frequency and threshold level. The tolerance in orientation of the

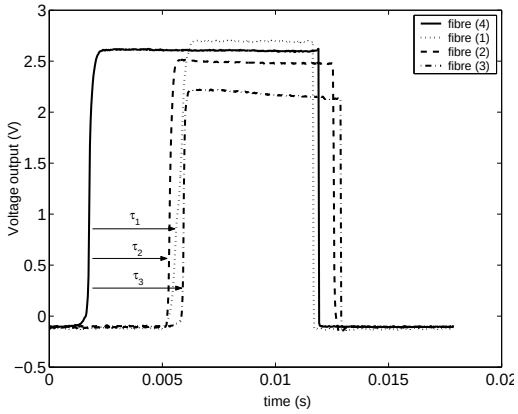

Figure 3.18: Four-point-probe signal corresponding to a bubble almost rising at the axis of the central tip (4).

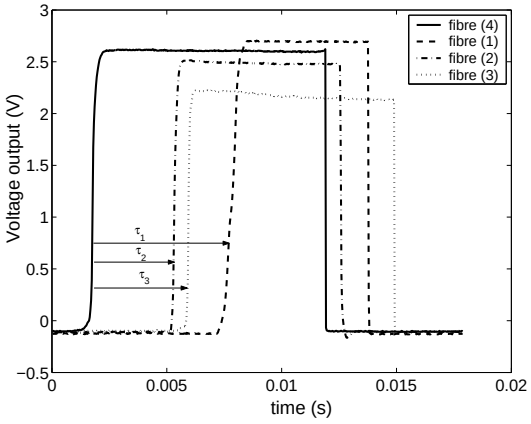

Figure 3.19: A four-point-probe signal obtained from a bubble not rising vertically at the axis of the central fibre (4). Fibre (1) is piercing the bubble much later than fibres (2) and (3).

bubble movement and bubble transverse distance with respect to the central tip are determined by β. For $\beta = 0$, no skew bubble movement or bubble distance with respect to the central tip is permitted. It is clear that in such an ideal case the real vertical diameter of the bubble would be measured. However, in practice the fibres 1, 2 and 3 will never pierce the bubble exactly at the same time (figure 3.18). Analysing a continuous signal by using $\beta = 0$ would mean, that no bubbles are selected. With an increasing value of β more bubbles are detected, but with a spread in the measured velocity and vertical chord length. Therefore, a β-sensitivity analysis was carried out, reported in section 3.4.4.3.

3.4.2.2 Effect of the curvature of the bubble surface

By using the method described above the curvature of the bubble surface is not taken into account when determining the vertical chord length of a detected bubble. The bubble surface is assumed to be flat in the plane through the tips (1, 2 and 3). However, the local bubble curvature effect can be taken into account in the computed vertical chord length. To that purpose Frijlink (1987) suggested a method to correct for this curvature effect. Using trigonometry and approximating the local bubble shape by a sphere, a correction was proposed for the vertical distance Δs_c between the central tip and the plane through the other three tips. This corrected distance is given by

$$\Delta s_c = \Delta s + \delta = \Delta s + \left[\frac{D_{bv}}{2} - \left(\frac{{D_{bv}}^2}{4} - d^2 \right)^{\frac{1}{2}} \right]. \tag{3.5}$$

The corrected bubble velocity can then be calculated from

$$U_c = \frac{\Delta s_c}{\tau}, \tag{3.6}$$

and the corrected vertical size follows from

$$D_{bvc} = U_c T. \tag{3.7}$$

During our air-water experiments the transverse distance between the fibres 1, 2 and 3 was $d = 0.6mm$ and the bubbles were ellipsoidal (to pancake) shaped with an equivalent diameter of 4 to $10mm$. For these conditions the bubble curvature effect is negligible, since it leads to a bubble velocity correction of less than 2.5 % for the smallest bubbles. Moreover, for wobbling type of bubbles ($D_b \geq 6 - 8mm$) the bubble top surface can be assumed to be flat. However, equations (3.5) to (3.7) are used to estimate the measurement technique accuracy.

3.4.2.3 Limitations of the selection criterion

The β selection criterion, as proposed in equation (3.4), is based on a minimisation of the deviation of the individual times of flight from the mean time of flight. It should be emphasized that this approach leads to some restrictions on the experimental conditions:

- The current technique is only suitable for preferential direction flows: the fibres axis should be oriented parallel to the main flow direction. The probe bending

would affect any liquid flow reversal and it would not be possible to detect negative bubble velocities.

- In order to pierce the same bubble with the three downstream fibres, the bubble horizontal dimension should be larger than the transverse distance between fibres: $D_{bh} > 2d$.
- If the bubbles are small and nearly spherical, the corrections as proposed by Frijlink (1987) (equations 3.5, 3.6 and 3.7) have to be applied. This critical bubble size for correction depends on the liquid properties (through bubble shape), the accuracy requirements as well as the probe dimensions.

3.4.3 Bubble-probe interaction experiments

Before using the four-point probe in a high-void-fraction bubbly pipe flow the bubble-probe interactions are investigated by measuring the single bubble velocity in two different manners (with the four-point probe and with a camera) using the experimental set-up depicted in figure 3.20.

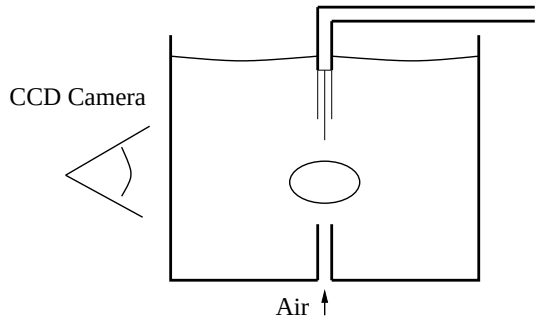

Figure 3.20: Experimental set-up to test the bubble-probe interaction.

The bubbles are released in water from a 0.8 and a $1mm$ inner diameter nozzle in a $100 \times 160mm$ glass box. The bubble trajectories were recorded with a Dalsa 256 CCD camera, providing pictures on a 256×256 pixel array at 200 frames per second. The trajectories of single bubbles are tracked at a high frame rate in order to obtain the vertical bubble velocity from a set of eight successive pictures. The four-point probe is positioned $1cm$ above, and on the axis of the nozzle in order to have a nearly stationary bubble motion at the measuring position. The bubbles are having an ellipsoidal shape with a vertical chord length in the range of $1.5mm$ to $2mm$ and an horizontal dimension ranging from $3mm$ to $5mm$. The four-point probe procedure described above is applied, i.e. the mean time of flight is used for the bubble velocity determination. The deviation of the individual times of flight from the mean value are minimised by positioning the four-point probe at the axis of the nozzle, resulting in β values of less than 0.15 for all the single bubble experiments. Figure 3.21 presents the comparison between bubble velocity as measured by the four-point probe and the bubble velocity measured with the CCD camera. The agreement is

good. From this result we may conclude, that the bubble-probe interaction effect on the bubble velocity is negligible. The inaccuracy of the probe measurements appears to be even smaller than the inaccuracy due to the pixel resolution of the CCD camera, which is less than 5% in terms of velocity. Similar findings are reported in Mudde and Saito (2001).

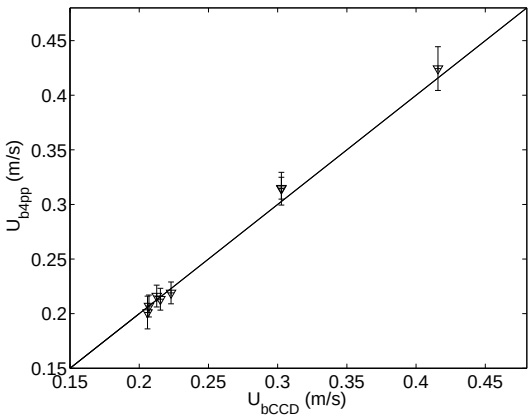

Figure 3.21: Bubble-probe interaction results for the bubble velocity. The bubble velocity obtained from the four-point probe is plotted versus the bubble velocity obtained from the CCD camera image analysis. The bisector is also shown.

The bubble vertical chord length as obtained with the four-point probe was compared with the CCD camera image analysis. Also in that case the agreement is reasonable between the four-point probe and the CCD camera image results (figure 3.22). No correction for bubble shape was applied to the present results. As suggested in section 3.4.2.2, the accuracy of this approach is found to be better when increasing the bubble chord length, since the larger bubbles are presenting a flatter shape (figure 3.22).

3.4.4 Bubbly pipe flow experiments

3.4.4.1 Experimental set-up

The experimental facility used for the vertical air-water bubbly pipe flow measurements is described in section 3.1.1. We used water as the liquid phase and the convected bubbly pipe flow configuration (with a centrifugal pump). For the local void fraction determination, two single-optical fibres were inserted at $h = 4m$ and $12m$. Two four-point probes were inserted in the vertical bubbly pipe flow at $h = 5m$ and $13m$. The four-point probes were oriented vertically downward, and could be traversed in the radial direction. A sketch of the probe with the traversing equipment is provided in figure 3.23.

Two of the six pressure transducers were situated upstream and downstream of the probe at $h = 5m$ (at $h = 4m$ and $h = 6m$). This allows to make a comparison

between the void fraction measurements obtained with the pressure transducers, the single-fibre probes and with the four-point probe. In general more bubble-probe interactions can be expected at the lowest bubble velocity conditions. We chose therefore to carry out the four-point probe tests at low liquid input conditions, corresponding to $U_{sl} = 1.7cm/s$. This will also have advantages for direct comparisons with pressure measurements.

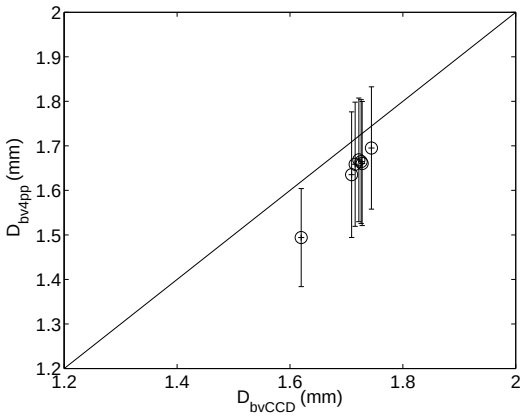

Figure 3.22: Bubble-probe interaction results for the bubble vertical chord length. The bubble chord length obtained from the four-point probe is plotted versus the bubble vertical size estimated from CCD camera image analysis. The bisector is also shown.

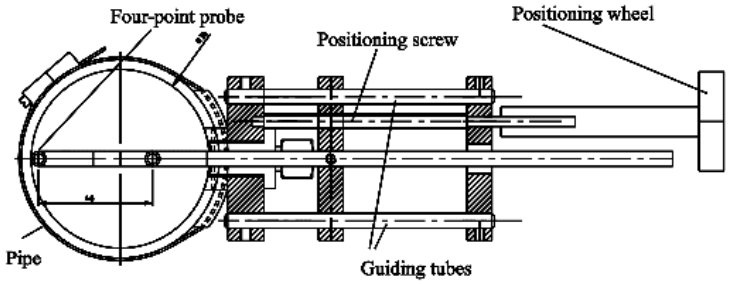

Figure 3.23: Top view of the implementation of the four-point probe on the pipe, including the traversing equipment.

3.4.4.2 Average void fraction evaluation

The void fraction could be estimated by means of the following three techniques: a single optical fibre probe, the central tip of the four-point optical fibre instrument or, for the direct determination of the volume average void fraction, from pressure gradient measurements.

For the local void fraction determination by using an optical fibre, a threshold was applied to the central tip voltage signal and the total time spent in gas bubbles was divided by the total measurement time: $\epsilon(r) = \left(\frac{\Sigma T_g}{T_{mes}}\right)(r)$. No additional criterion was used for the void fraction calculation. The mean value could then be computed by integrating $\epsilon(r)$ over the cross sectional area.

The mean void fraction evaluation from pressure measurements was done in the following way: for the low flow conditions investigated ($Re_{sl} = 1200$), the friction and acceleration contributions to the pressure gradient are negligible with respect to the hydrostatic pressure gradient. Also, regarding the low-pressure conditions during the experiments ($P \leq 3bars$), the air density contribution to the hydrostatic head is negligible regarding the liquid density effect. The sectional mixture density being approximated by $\rho_m \approx (1 - < \epsilon >)\rho_l$, the mean void fraction $< \epsilon >$ is then given by:

$$< \epsilon > = 1 - \frac{1}{\rho_l g} \frac{\Delta P}{\Delta z}. \tag{3.8}$$

To investigate a possible bias effect due to miscounted bubbles, the area average void fraction value obtained with the central tip of the four-point probe, $< \epsilon_{4pp} >$, is compared with the pressure drop technique result $< \epsilon_p >$. This is shown in figure 3.24 for the profiles obtained at $h = 5m$ and using the pressure drop between $h = 4m$ and $h = 6m$. The two measurement techniques provide similar results, confirming that the four-point fibre probe is not interacting with the bubbles motion, even for large void fraction values.

3.4.4.3 Sensitivity with respect to the bubble-selection criterion

As mentioned in the previous paragraph a bubble-selection criterion based on the deviation of the three individual times of flight (measured with tips 1, 2 and 3) from their mean value is applied (equation 3.4). Of course the chosen value of β has a strong effect on the frequency of selected bubbles and on the accuracy of the results. In figure 3.25 the ratio of the number of selected bubbles to the total number of bubbles passing through the central tip (4) is plotted for four void fraction conditions as a function of the value of β. When β tends to zero, the number of selected bubbles also tends to zero. For $0.1 < \beta < 0.4$ the number of selected bubbles increases significantly with β. A comparison of the measured bubble velocity and measured probability density of the bubble size obtained for various β-values shows, that the results are nearly insensitive to the β-value for $\beta \leq 0.25$ (Fortunati *et al.*, 2002) while the number of selected bubbles increases strongly with β (figure 3.25). Therefore, the value $\beta = 0.25$ will be used in the following, since it gives a good compromise between the frequency of selected bubbles and the robustness of the bubble-selection criterion. Using this β-value, the number of selected bubbles is

found to represent typically 5 to 30 % of the bubbles hitting the central tip. The relative number of selected bubbles is larger for the high void fraction conditions (figure 3.25). This is attributed to the increased bubble size and the more rectilinear motion of the bubbles when the void fraction is increased.

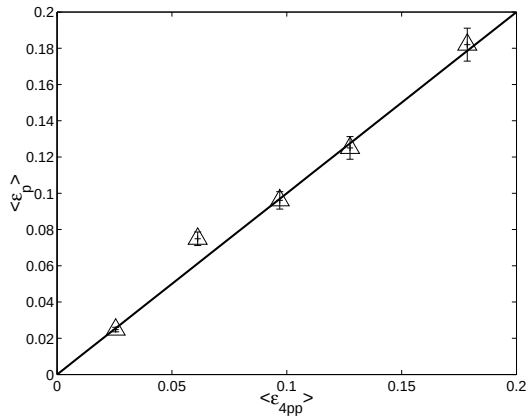

Figure 3.24: Void fraction obtained from the area integration of the void fraction profile (measured with the four-point probe) versus the mean void fraction obtained from pressure drop measurement, ϵ_p. The bisector is also shown.

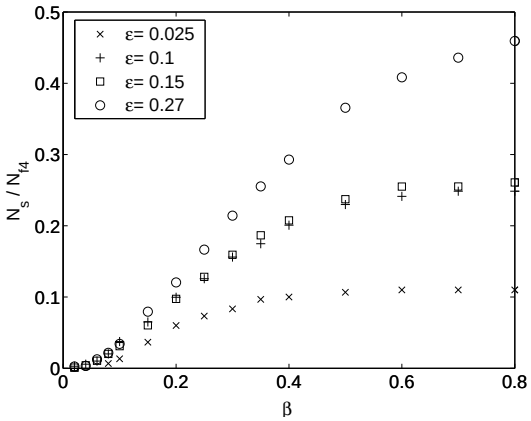

Figure 3.25: Sensitivity of the number of selected bubbles N_s on the β parameter at the bubbly pipe flow centerline. The number of selected bubbles is normalized by the number of bubbles pierced by the central fibre (4), N_{f4}.

3.4.4.4 Accuracy

The accuracy of the four-point probe is investigated by comparing the gas flow rate $Q_{g,4pp}$ as measured via the four-point probe with the gas flow rate measured via the gas flow meter. The gas flow rate measured with the four-point probe was found by area-averaging the local bubble velocity and void fraction measurements:

$$Q_{g,4pp} = \int_A \epsilon U_b dA = 2\pi \int_0^R \epsilon U_b r dr, \tag{3.9}$$

assuming radial symmetry for the second equality. With the four-point probe, the measurements were made at a (limited) number of points in the cross-section. We therefore use the discretised version:

$$\int_A \epsilon U_b dA = 2\pi \sum_{r_i=0}^{R} \epsilon_i U_{bi} r_i \left(r_{i+\frac{1}{2}} - r_{i-\frac{1}{2}} \right). \tag{3.10}$$

The gas flow meter indicates the measured gas flow rate at atmospheric pressure $Q_{g,atm}$. The local gas flow rate in the vertical pipe is calculated from the measurement provided by the gas flow meter and by correcting for the change of pressure with height:

$$Q_{g,fm} = \frac{P_{atm}}{P_s} Q_{g,atm}, \tag{3.11}$$

in which P_s is the pressure at the measurement position.

In figure 3.26 the four-point probe average value $Q_{g,4pp}$ as determined by equation (3.10) and the gas flow rate $Q_{g,fm}$ calculated from equation (3.11) are compared for $\beta = 0.25$.

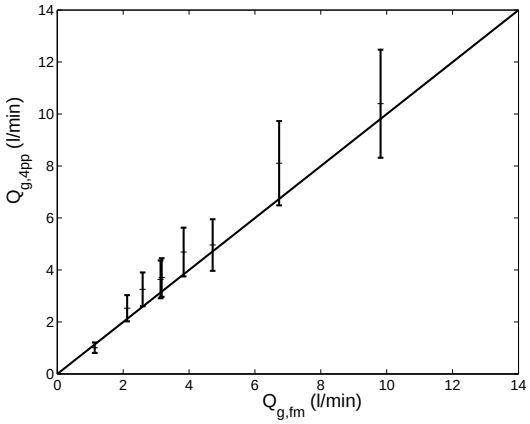

Figure 3.26: Comparison between the gas volumetric flow rate obtained by the four-point probe measurements and by global measurements. The void fraction ranges from 0.01 to 0.28 and the bisector is also shown.

Good agreement is found between $Q_{g,fm}$ and $Q_{g,4pp}$. The main source of inaccuracy is due to the near-wall values of bubble velocity. Since the probe was inserted into a $6mm$ diameter tube, the local void fraction and bubble velocities could not be measured for $\frac{r}{R} > 0.93$, leading to 15 % inaccuracy on the area-integrated value. From this results it can be concluded, that the bubble velocity can be measured within the expected accuracy by using a four-point optical glass fibre probe. However, the accessibility of the near wall region is not feasible with this probe due to its dimensions.

3.4.5 Measurement results

3.4.5.1 Vertical and spherical equivalent mean bubble size

The mean vertical bubble chord length was measured at the centreline of the pipe for various gas flow rate conditions and keeping the liquid flow rate constant. The results, presented in figure 3.27, show that the measured vertical chord length of the bubbles is in the range of 2 to $3.5mm$. For each point, more than 1000 bubbles are selected by applying the β selection criterion to the collected signal. The results are consistent with the bubble size as evaluated from photos. Predictions made with existing models for bubble generation from porous plates (Koide *et al.*, 1968) show the same trend of increased bubble size with gas flux. The bubbles were having an ellipsoidal shape with an aspect ratio of the order of 1 to 2.5 at the bottom location of the pipe ($h = 5m$).

At the top the bubbles were flattening and eventually evolving into a wobbling type of regime, due to expansion and coalescence. Also some spherical cap bubbles were observed in the core zone of the pipe at $h = 13m$. Within the accuracy of the instrument, the measured mean vertical chord length at the centreline were similar

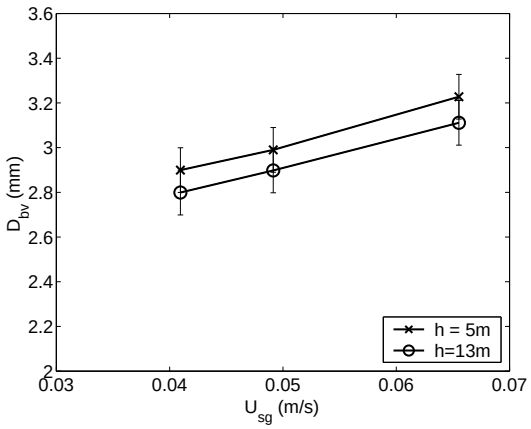

Figure 3.27: Bubble vertical chord length in the tube centerline and at $h = 5m$ and $13m$ as a function of the superficial gas velocity.

at $h = 5m$ and $h = 13m$ (figure 3.27). Since two different four-point optical fibre probes were applied at $h = 5m$ and at $h = 13m$, the vertical distance between fibre 4 and the three other fibres could be slightly different ($\Delta s = 1.6 \pm 0.03mm$). However, figure 3.27 suggests that the increase of the spherical-equivalent bubble size due to expansion (and eventually coalescence) was compensated by bubble flattening with height.

The ratio of pressure from $h = 5m$ to $h = 13m$ was typically $\frac{P_{5m}}{P_{13m}} \approx \frac{3}{2}$, leading to a 10 to 15% increase of the spherical equivalent bubble size with height ($\frac{D_{b,13m}}{D_{b,5m}} \approx (\frac{P_{5m}}{P_{13m}})^{\frac{1}{3}} \approx 1.14$). The changes in vertical chord length with height can be inferred by using a bubble aspect ratio correlation for the ellipsoidal-shape bubbles (Tomiyama *et al.*, 2002b): $\chi = 1 + 0.163{E_0}^{0.757}$, in which $E_0 = \frac{g\Delta\rho{D_b}^2}{\sigma}$ is the Eötvös number and χ is the ratio of the major to minor axis of the (ellipsoidal-shape) bubbles. The spherical equivalent diameter is related to the measured vertical chord length by $D_b = D_{bv}\chi^{2/3}$. Assuming a 15 % increase of the spherical equivalent bubble size, the vertical chord length of the (ellipsoidal) bubbles will increase by less than 10% for $D_b > 5mm$ in our air-water system. These expectations are consistent with the measurements presented in figure 3.27. Due to the potential deviations in the probe geometrical properties and the changes of bubble aspect ratio with height, the measured mean vertical chord length were similar at $h = 5m$ and $h = 13m$.

3.4.5.2 Void fraction profiles

The transverse void fraction was measured for various gas flow rates and at a fixed liquid input ($U_{sl} = 1.7cm.s^{-1}$, i.e $Re_{sl} = 1200$). At low values of the gas flow rate the void fraction profiles were wall peaking, both at the low and high vertical position in the pipe (figure 3.28). When increasing the gas flow a transition from wall peaking void fraction profile to core peaking was observed (figure 3.29). We compared the void fraction measurements made with the four-point probe at $h = 5m$ and $h = 13m$ with those made with the single-point probe at a height of $h = 4m$ and $h = 12m$. As can be seen from figure 3.28 and figure 3.29 the agreement is good. The shift of the mean void fraction values is due to gas expansion. The transition from wall peaking to core peaking is known to be strongly related to the bubble size (Liu, 1993a; Moursali *et al.*, 1995). The measured critical bubble chord length for transition from wall peaking to core peaking was $D_{bv,crit} = 3mm$, which corresponds to an equivalent spherical diameter of $D_{b,crit} \approx 5.5mm$. This is in agreement with the literature on bubble migration in a shear field (Tomiyama *et al.*, 2002b; Liu, 1993a; Lucas *et al.*, 2001).

3.4.5.3 Bubble velocity

The development of the bubble velocity profile associated with the void fraction profile evolution was measured with the four-point probes at $h = 5m$ and $h = 13m$. At wall peaking conditions the bubble velocity profile is flat (figure 3.30), while at wall-to-core peaking conditions the bubble velocity is evolving into a parabolic type of profile (figure 3.31).

The bubble velocity profile is in general coupled with a number of effects such as the magnitude of the frictional and gravitational forces (Mudde and Saito, 2001), the

local slip velocity of the bubbles and the transverse lift force (Lucas *et al.*, 2001). During the present low liquid input experiments ($Re_{sl} = 1200$), the changes of bubble velocity profile were essentially related to the increased bubble size and the occurrence of large spherical cap bubbles in the core zone of the pipe, with a large slip velocity. Also, a parabolic liquid velocity profile with a thin falling film at the wall can be expected during those experimental conditions, since the transition from bubbly flow to slug flow was approached. These effects result in an increased net bubble velocity at the centreline.

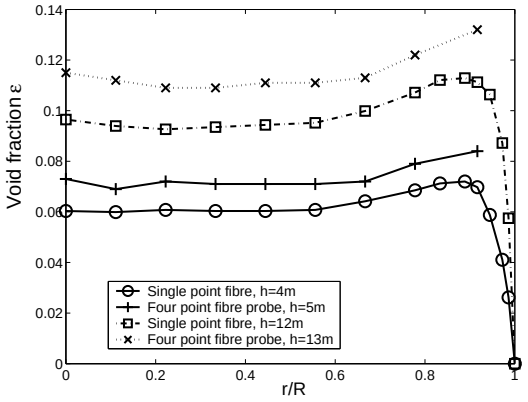

Figure 3.28: Void fraction profile evolution from $h = 4m$ to $h = 13m$ and with $\frac{Q_g}{Q_l} = 2$. The profiles remain wall peaking with height and the initial bubble diameter is $D_b \approx 4mm$.

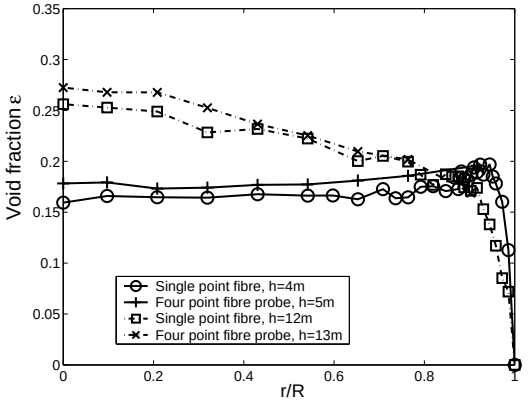

Figure 3.29: Void fraction profile evolution from $h = 4m$ to $h = 13m$ and with $\frac{Q_g}{Q_l} = 4$. The initial bubble diameter is $D_b \approx 5.5mm$. In those particular conditions the void fraction evolves from wall peaking to core peaking with height.

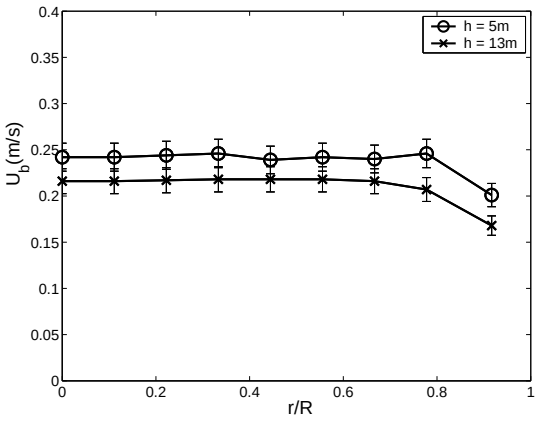

Figure 3.30: Bubble velocity evolution from $h = 5m$ to $h = 13m$ and with $\frac{Q_g}{Q_l} = 2$. The void fraction remains wall peaking with height.

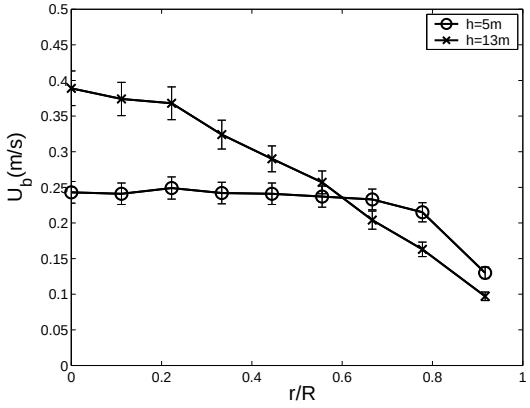

Figure 3.31: Bubble velocity evolution from $h = 5m$ to $h = 13m$ and with $\frac{Q_g}{Q_l} = 4$. The void fraction evolves from wall peaking to core peaking with height. The associated bubble velocity is evolving into a parabolic type of profile.

3.4.5.4 Comparison with liquid velocity measurements

To check the reliability of the four-point probe results, also liquid velocity measurements were carried out. The liquid velocity was measured by using a laser-Doppler anemometer, with the equipment described in section 3.3.1. The LDA measurement volume was placed $5mm$ below the central tip of the four-point probe to compare the results of the two measurement techniques (figure 3.32).

In figure 3.33 and 3.34 the profiles obtained for the void fraction, the liquid velocity and the gas velocity are presented for zero liquid input conditions, i.e. the

pipe flow is used in the bubble column flow mode.

The well known returning liquid flow is observed near the wall. For this case of low gas flow rate the void fraction profile (as measured with the four-point probe) is found to be flat (see figure 3.33). The slip velocity $U_{slip} = U_b - U_l$ can be correlated to the terminal velocity of a single bubble U_∞ and the local void fraction.

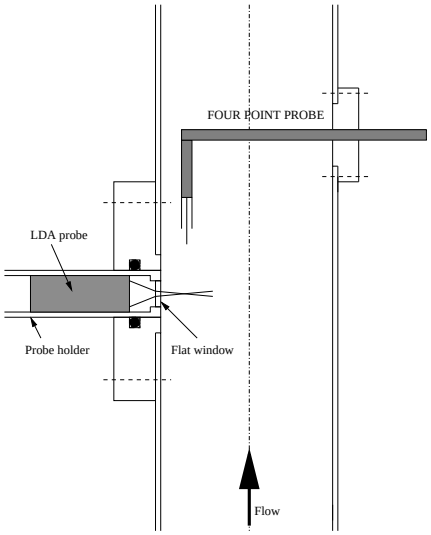

Figure 3.32: Arrangement for liquid velocity measurements with a LDA and bubble velocity with the four-point probe.

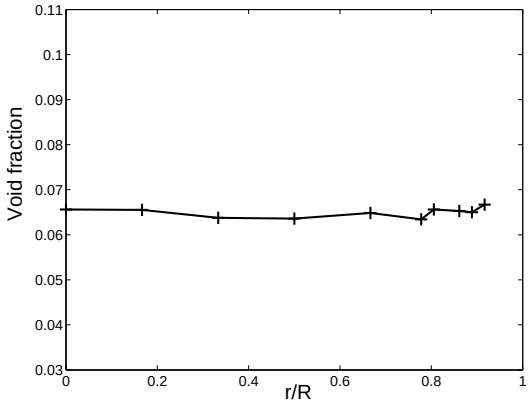

Figure 3.33: Void fraction profile obtained in the bubble column flow mode (no liquid input).

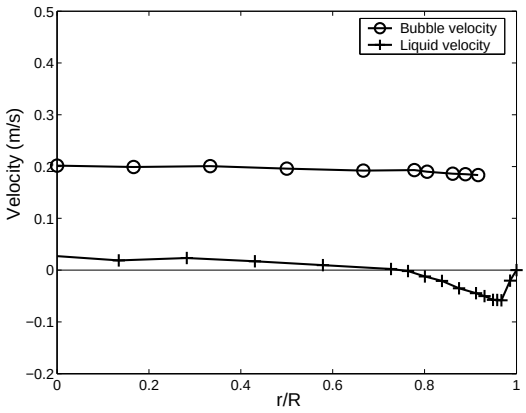

Figure 3.34: Bubble and liquid velocity profiles obtained in the bubble column flow mode. The gas velocity profile is similar to the trend of the liquid velocity (with a shift of magnitude U_{slip}).

Richardson and Zaki (1954) proposed $U_{slip} = U_\infty(1-\epsilon)^n$. More recently, Garnier *et al.* (2002) suggested $\frac{U_\infty - U_{slip}}{U_\infty} = \epsilon^{\frac{1}{3}}$. These correlations predict the slip velocity $U_{slip} = f(\epsilon, U_\infty)$ to be constant in the radial direction if the void fraction and bubble size are constant. This is in agreement with the bubble column measurements in the core zone ($r < 28mm$): the vertical slip velocity is constant in the radial direction (figure 3.34), as well as the void fraction (figure 3.33). Only near the wall, where the liquid velocity was negative, the bubble velocity measurements were biased to larger values. This is due to three reasons. First, in that region of the flow some bubbles were observed to travel downward, which could not be measured with the four-point optical fibre probe. Secondly, the amplitude of the (negative) liquid velocity at the fibre location was damped by the probe, the probe bending being positioned upstream in that case. Finally, bubbles presenting a low momentum ($U_b < 0.03m/s$) were rarely selected compared to larger velocity bubbles, their motion being more easily affected by the fibres. This probe is therefore only suitable for co-current flows.

3.4.6 Conclusion

The possibility of measuring the bubble velocity and size in a high void fraction bubbly flow by using a four-point optical fibre probe was investigated. Special attention was paid to the bubble-probe interactions and the validity and efficiency of the bubble selection criterion used for high void fraction flow conditions. First, single bubble experiments showed that the bubble-probe interaction effects were negligible for bubbles rising at the axis of the probe.

The reliability of the four-point probe was then demonstrated by applying the instrument to an upward bubbly pipe flow operating at void fraction conditions of up to $\epsilon = 0.28$. It was shown that the bubble selection criterion could be chosen in such a way, that a good compromise was possible between the accuracy and the frequency of selected bubbles. This criterion for selecting bubbles rising at the axis of the probe corresponds to $\beta = 0.25$ in equation (3.4). The void fraction measured with the central fibre of the probe was found to be consistent with pressure and single optical fibre measurements. Also, the measured bubble velocity profiles were in agreement with gas volumetric flow rate measurements. The validity of the local bubble velocity measurements in co-current flow situations was further confirmed by comparing the bubble velocity profile with the liquid velocity at homogeneous void fraction conditions. It was found that the bubble velocity and chord length could be measured within 5% accuracy by using the above mentioned bubble selection criterion. However, near wall measurements could not be carried out with our probe due to its dimensions. Therefore, a single point probe will be used to gain accuracy on the near wall void fraction determination and improve the area-average measurements.

The present time of flight method permits to compute the bubble vertical chord length. For obtaining the bubble spherical equivalent diameter with this approach, a correlation for the bubble aspect ratio will be needed. As an extension of the present time of flight method, it would be interesting to have a direct access to the bubble horizontal chord length. Such a method would potentially allow for investigating the existence of a lift-force inversion effect with increased bubble deformation in large void fraction flows, as already observed for single bubbles by Tomiyama *et al.* (2002b) (see figure 2.3.c). It is therefore of interest to investigate the possibility of estimating the individual bubble shape and orientation by using the time series provided by a four-point probe. This will be the subject of the next section.

3.5 Bubble shape and orientation determination with a four-point optical-fibre probe*

3.5.1 Introduction

The experimental determination of the particle motion, shape and orientation is of importance for a proper understanding and modelling of two-phase flows. For instance, the transverse motion of single bubbles is known to be affected by the bubble size and shape, resulting in a spiralling or a zigzagging behaviour (Magnaudet and Eames, 2000; De Vries, 2001). In shear flows, the direction of single fluid particles transverse migration is known to depend on the particle shape, both for solid particles (Gavze and Shapiro, 1997), liquid drops (Mortazavi and Tryggvason, 2000; Magnaudet *et al.*, 2003) or for gas bubbles (Tomiyama *et al.*, 2002b; Ford and loth, 1998; Bunner and Tryggvason, 2003). The effect of deformed bubbles on their transverse migration has been clearly demonstrated experimentally in Tomiyama *et al.* (2002b) by using single bubble tracking experiments in simple shear flows of viscous liquids. A transverse lift force coefficient correlation was deduced from the experiments, by connecting the lift force to the bubble size and shape.

The quantities describing the bubble shape and orientation are difficult to obtain experimentally in high void fraction conditions, for which direct optical techniques cannot be applied. Optical fibre probes provide access to local properties of the dispersed phase, since they give access to the gas-liquid interface passage time. Single, two and four-point optical probes have been developed and successfully applied for the determination of the bubble velocity and chord length (Frijlink, 1987; Cartellier, 1992; Barrau *et al.*, 1999; Mudde and Saito, 2001).

The objective of this section is to develop and validate a method for determining the parameters describing the motion of non-spherical bubbles rising on non-straight paths, by using their associated four-point optical fibre probe time series. The four-point probe technique used in this study is based on the same four-point probe equipment as the one used in the previous section. This new method is however conceptually different from the above-mentioned methods: it uses a numerical model to reconstruct the bubble geometry and position from its four-point probe signal. This approach has the potential to provide for each individual bubble its aspect ratio, its spherical-equivalent diameter, its orientation as well as its three velocity components.

First, this technique will be described. We will then make use of synthetic data for validating our conceptual approach. The experimental validity of our approach will be investigated by using single bubble experiments, during which the bubble properties are also obtained via images‡. The comparison between the results provided by the two techniques will be discussed. The four-point probe technique developed in the present study will then be applied to multiple bubbles four-point probe data collected on our vertical upward bubbly pipe flow. The validity of the bubble aspect

*See also: S. Guet, S. Luther, & G. Ooms. (2004). 3^{rd} *International Symposium on two-phase flow modelling and instrumentation*, Pisa.

‡Details about the camera model and the numerical robustness of the present method are given in: S. Luther, J. Rensen, & S. Guet. (2004). *Exp. in Fluids.*, 36, 326-333.

ratio estimate will be discussed by comparing our results with an available correlation, and some first results on the bubble orientation in the near wall region of our pipe will be presented.

3.5.2 Bubble reconstruction algorithm

A typical bubble-probe interaction signal and the associated image series are presented in figure (3.35). For such a bubble-probe interaction, a set of times (T_0, T_1), (T_2, T_3), (T_4, T_5), and (T_6, T_7) are obtained for the rising and the falling edges, respectively. The signal of the optical four-point probe is defined as:

$$\begin{array}{lll} \text{fibre } \#4 & [T_0, T_1] & T_0 < T_1, \\ \text{fibre } \#1 & [T_2, T_3] & T_2 < T_3, \\ \text{fibre } \#2 & [T_4, T_5] & T_4 < T_5, \\ \text{fibre } \#3 & [T_6, T_7] & T_6 < T_7. \end{array} \tag{3.12}$$

At time T_0 the central tip pierces the bubble surface. Referring the following piercing times to T_0, we define the signal of a bubble probe interaction to be

$$\vec{t} = (t_1, ..., t_7), \tag{3.13}$$

where $t_i = T_i - T_0$ for $i = 1, ..., 7$.

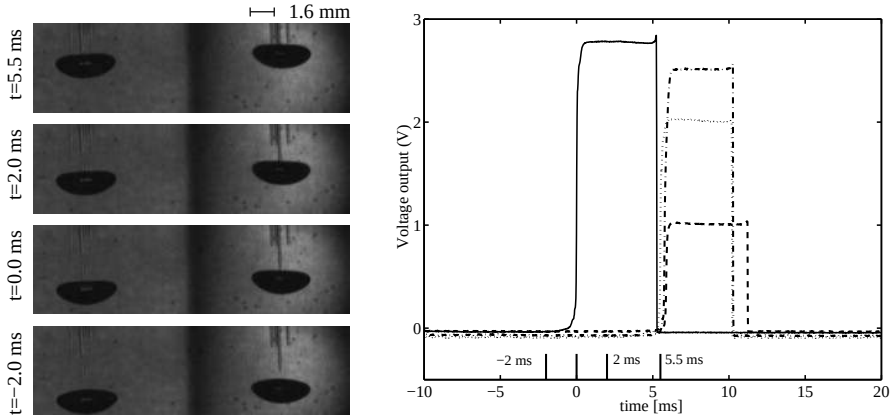

Figure 3.35: Bubble-probe interaction. (a) Example of a stereoscopic image sequence. Each frame shows the two orthogonal views in the left and right half of the image. (b) The corresponding probe signals of fibre 4 (solid line), fibre 1 (dashed line), fibre 2 (dashed-dotted line), and fibre 3 (dotted line).

The bubbles are assumed to be oblate spheroids with principal axes $a = b$ and c, as depicted in figure 3.36. We use a coordinate system $x_b = (x_b, y_b, z_b)$ attached to the centre of the bubble such that the bubble is rotationally symmetric with respect to the z axis.

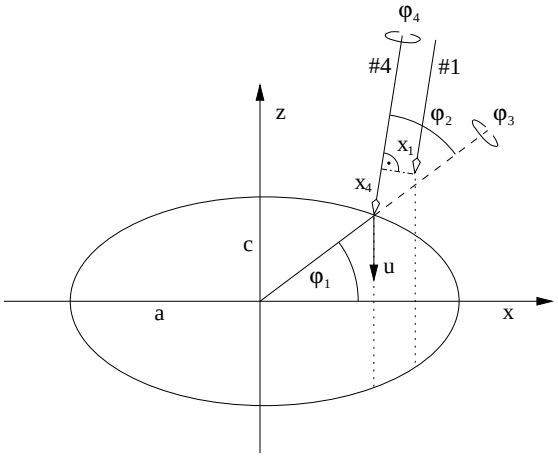

Figure 3.36: Geometric model. The system of reference is located in the origin of the (ellipsoidal) bubble.

The surface of the bubble is defined by

$$\frac{x_b^2 + y_b^2}{a^2} + \frac{z_b^2}{c^2} = 1. \tag{3.14}$$

The position of the tip of the central fibre 4 is denoted by $\vec{x}_b^4$. It pierces the surface of the bubble in $\vec{x}_{b,0}^4$ at $t = 0$. This point can be expressed in polar coordinates by the angle φ_1. We define $\vec{x}_{b,0}^4$ to be in the $x - z$ plane or

$$\vec{x}_{b,0}^4 = \begin{pmatrix} a \sin \varphi_1 \\ 0 \\ c \cos \varphi_1 \end{pmatrix}, \tag{3.15}$$

with $\varphi_1 \in [0, \pi]$. The symmetry axis of the probe can be rotated using the rotation matrix $\underline{\mathbf{R}}_{op} = \underline{\mathbf{R}}_{op}(\varphi_2, \varphi_3, \varphi_4)$. The positions of the fibre 1, 2, and 3 are then

$$\begin{aligned} \vec{x}_{b,0}^1 &= \vec{x}_{b,0}^4 + \underline{\mathbf{R}}_{op} \begin{pmatrix} 0 \\ d \\ s \end{pmatrix}, \\ \vec{x}_{b,0}^2 &= \vec{x}_{b,0}^4 + \underline{\mathbf{R}}_{op} \begin{pmatrix} -\frac{1}{2}\sqrt{3}d \\ -\frac{1}{2}d \\ s \end{pmatrix}, \\ \vec{x}_{b,0}^3 &= \vec{x}_{b,0}^4 + \underline{\mathbf{R}}_{op} \begin{pmatrix} \frac{1}{2}\sqrt{3}d \\ -\frac{1}{2}d \\ s \end{pmatrix}, \end{aligned} \tag{3.16}$$

where s and d describe the spacing of the fibre tips and $\vec{\underline{R}}_{op} = \underline{\mathbf{R}}_{op}(\varphi_2, \varphi_3, \varphi_4)$ their rotation with respect to the bubble reference frame with $\varphi_2 \in [0, \pi]$, $\varphi_3 \in [0, 2\pi]$, and $\varphi_4 \in [0, 2\pi]$. We assume that the bubble has a constant velocity u during the interaction. We also assume that the local liquid velocity is parrallel to the bubble velocity. This assumption is valid for stagnand liquids and low liquid input co-current flows. Within the frame of reference given, the probe tips move with respect to the bubble along the trajectory

$$\begin{pmatrix} x^k_{b,t_i} \\ y^k_{b,t_i} \\ z^k_{b,t_i} \end{pmatrix} = \begin{pmatrix} x^k_{b,0} \\ y^k_{b,0} \\ z^k_{b,0} \end{pmatrix} + t_i \begin{pmatrix} 0 \\ 0 \\ -u \end{pmatrix}, \tag{3.17}$$

where $k = 1, .., 4$. These trajectories intersect the bubble surface at times

$$\tilde{t}_i = \left(z^k_{b,0} \pm c\sqrt{\Delta_i} \right) / u, \quad \text{with} \quad \Delta_i = 1 - \frac{(x^k_{b,0})^2 + (y^k_{b,0})^2}{a^2}. \tag{3.18}$$

Equation (3.18) has none, one, or two real solutions corresponding to $\Delta_i < 0$, $\Delta_i = 0$, or $\Delta_i > 0$, respectively. A bubble-probe interaction is called a complete interaction, if each of the four fibre tips intersects the bubble surface twice. Given a parameter vector $\vec{p}$, our numerical model $\mathcal{M}$ should provide a probe signal similar to equation (3.13), i.e.

$$\mathcal{M}(\vec{p}) \mapsto \tilde{\vec{t}} = (\tilde{t}_1, ..., \tilde{t}_7). \tag{3.19}$$

A particular choice of the parameter vector $\vec{p}$ is a representation of a specific bubble-probe interaction event. To search for the best reconstruction of the interaction times $\tilde{\vec{t}}$ for each bubble, we define a cost function that evaluates for each $\vec{p}$ the discrepancy between the measured time signal and its representation by the model. A suitable choice is the sum of the squares of the normalised differences

$$C(\vec{p}) = \sum_{j=1}^{7} \left(\frac{t_j - \tilde{t}_j}{t_j} \right)^2. \tag{3.20}$$

We seek for a vector $\vec{p}$ that minimises $C(\vec{p})$, i.e. the mismatch between observed and modelled time series. The equations (3.14) to (3.18) constitute the bubble-probe interaction model $\mathcal{M}$. Its parameter vector is $\vec{p} = (a, c, u, \varphi_1, \varphi_2, \varphi_3, \varphi_4)$, i.e. the bubble's minor and major axes, its velocity, and the four angles of rotation. Only complete interactions are considered. The minimisation of the cost function given by equation (3.20) is numerically solved using a constrained non-linear least-square optimisation. The numerical robustness of this method has been demonstrated by using synthetic four-point optical fibre probe data (see Luther *et al.* (2004) and Rensen (2003)). In the present contribution, we focus on the accuracy of recovering the bubble shape and orientation from four-point probe experimental data. The numerical approach is first validated using synthetic data.

3.5.3 Validation by synthetic data

The accuracy of the algorithm is evaluated using data from simulated bubble-probe interactions, represented by a set of synthetic parameters $\vec{p}$. These data are then

reconstructed by using the model $\mathcal{M}$. This allows to validate the accuracy of the numerical method for the bubble orientation and shape reconstruction.

A set of 100 synthetic data is generated. The major axes and rise velocities are chosen to be 1.5 mm to 3 mm and 26 cm/s, while the minor axes is taken as 1.5 mm. The piercing angle φ_1 is taken from a uniform distribution in the interval $[0, \pi]$, whereas φ_3 and φ_4 are chosen from the same distribution in $[0, 2\pi]$ (see figure 3.36). The inclination angle φ_2 of the bubbles with respect to the probe axis is chosen from a Gaussian distribution with zero mean and a standard deviation of 30 degrees.

3.5.3.1 Accuracy of bubble orientation determination

The accuracy of the numerical algorithm is evaluated by comparing the synthetic test data with its reconstruction using equation (3.20). Defining $\vec{Z}_p$ as the probe axis, the polar angles

$$\theta = \tan^{-1}\left(\frac{\sqrt{\left(\vec{Z}_p.\vec{x}\right)^2 + \left(\vec{Z}_p.\vec{y}\right)^2}}{\left(\vec{Z}_p.\vec{z}\right)}\right) \quad \text{and} \quad \phi = \tan^{-1}\left(\frac{\vec{Z}_p.\vec{y}}{\vec{Z}_p.\vec{x}}\right) \tag{3.21}$$

given by the input synthetic data and as obtained from the algorithm are then compared for validating our bubble orientation estimate technique. Figure 3.37 illustrates the bubble-probe interaction in the frame of reference attached to the bubble and to the probe, i.e. the laboratory. The comparison of the bubble angle of orientation as generated by the synthetic data and as obtained by the model are shown in figure 3.38. It is clear from this figure, that the algorithm reproduces satisfactorily the bubble orientation parameters.

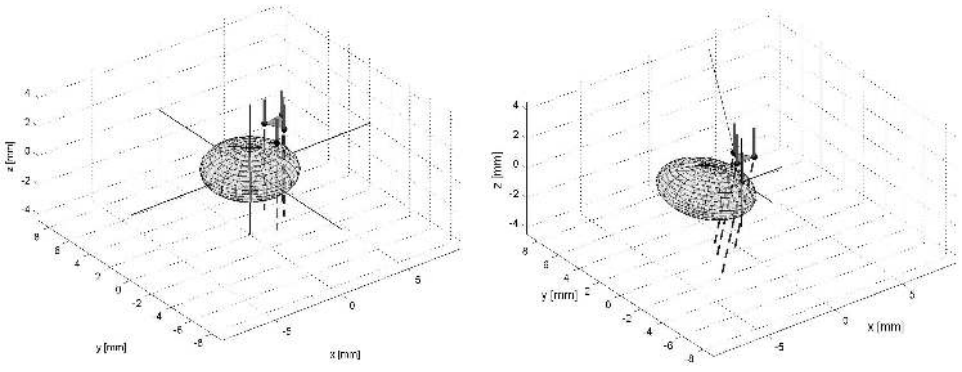

Figure 3.37: Frame of reference. (a):Coordinate system attached to the centre of the bubble, used in the numerics. (b): coordinate system attached to the probe, which gives the orientation of the bubble in the laboratory frame of reference. Both figures refer to the same (synthetic) bubble.

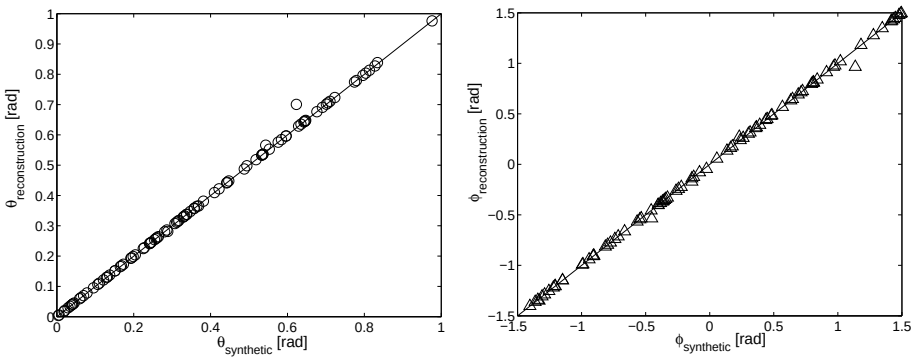

Figure 3.38: Accuracy of the reconstruction of the bubble orientation. The bubble polar angles are compared with their synthetic input. (a): θ, and (b): ϕ.

3.5.4 Single bubble experiments

In figure 3.39 the single bubble experimental set-up is depicted. It allows for the simultaneous recording of the probe signal and a stereoscopic high-speed image sequence. The four-point probe is vertically mounted in a Plexiglas cylinder of 10 cm inner diameter and 40 cm height filled with (purified) water. The cylinder is surrounded by a rectangular Plexiglas box filled with water for proper index match-

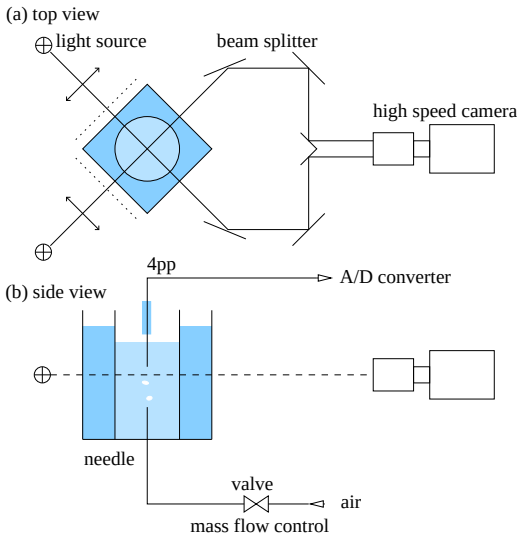

Figure 3.39: Experimental set-up for stereoscopic high-speed imaging. (a) Top view with beam splitter and illumination optics. (b) Side view.

ing. Single bubbles are generated using a capillary. The four-point probe signal is collected by an analog-to-digital converter (National Instruments PCI-6023E). The sampling rate is f=50kHz per channel with a resolution of 12 bit. The optical set-up consists of the high-speed camera (Kodak CR Imager 2000), the beam splitter and the illumination. The geometry of the optical set-up is calibrated using a calibration grid (Melles-Griot dot target) with dot spacing of 0.4 mm and an accuracy of $\pm 2\mu$m. More details about the calibration of the optical set-up are given in Luther *et al.* (2004).

The results from high-speed observations are compared with those from our optical probe data processing algorithm. To that purpose, optical probe data and stereoscopic images of rising bubbles are taken simultaneously. In figure 3.40 a typical example of a comparison between the collected and reconstructed time signal is presented. The arrival times and the departure times of the bubble on the probe could be reconstructed with an accuracy of less than 0.1%. It should be noted that the amplitude of the reconstructed signal is not part of the model but was adjusted to the experimental data for display purpose only. We also investigated the agreement between the results of the optical probe measurements and the results of the image analysis. The major axis, the minor axis, and the rising velocity were also computed from the optical probe signal and compared with the data obtained by the image processing for a set of bubble-probe interactions (Luther *et al.*, 2004; Rensen, 2003). The geometry of the bubbles was predicted within an accuracy of typically 20%.

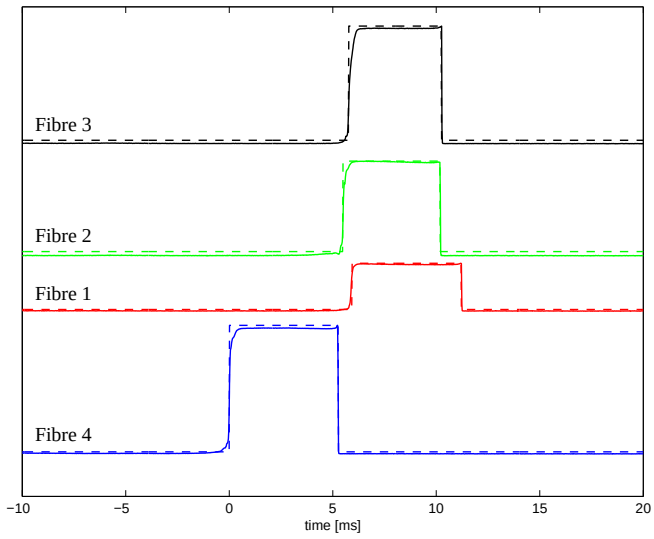

Figure 3.40: Typical signal from the four-point optical fibre (solid line) and its reconstruction (dashed line).

3.5.5 Multiple bubble experiments

In this section, we use the four-point probe data series collected on our vertical upward bubbly pipe flow experimental set-up (described in section 3.1.1). A top view of the geometrical arrangement of our four-point probe on the pipe flow experimental set-up is depicted in figure 3.41.

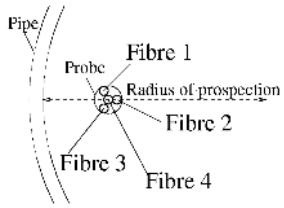

Figure 3.41: Top view of the probe alignment in the pipe.

3.5.5.1 Four-point probe measurements validity

The centreline four-point probe data are first used to validate the measurements. For symmetry reasons and since on average the bubbles are rising vertically, it is expected that the relative probability of piercing the bubbles first for fibre 1, 2 and 3 are equally distributed at the pipe centreline. We define the probability P_i of piercing first the bubble by fibre i, as:

$$P_i = P(t_i > t_j) \forall i \neq j, \tag{3.22}$$

where $i = 1$, 2 or 3. In figure 3.42 an histogram representing the relative probability distributions P_i is shown for a measurement carried out at the pipe centreline. As expected, $P_i \approx \frac{1}{3} \forall i$ in that case, since on average the bubbles are travelling upward

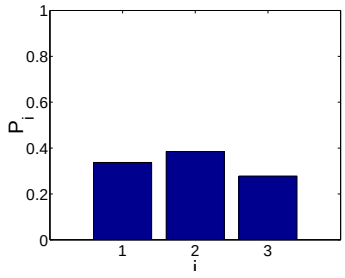

Figure 3.42: Histogram representing the relative probability of piercing first the bubbles for fibre i ($i = 1$, 2 or 3) for a measurement at the tube centreline and using 1000 bubble probe interactions. As expected, $P_i \approx \frac{1}{3} \forall i$.

with a zero mean orientation angle. The differences between the P_i values ($0.25 < P_i < 0.4$) are due to the uncertainties in the positioning of each fibre: the vertical distance between fibre 4 and fibre 1, 2 and 3 is given with an accuracy of $\pm 0.03mm$.

3.5.5.2 Bubble shape estimate

We also apply our bubble reconstruction algorithm to our four-point probe pipe flow data. To validate our method, the individual bubble aspect ratio results are compared with existing models. We use the correlation proposed in Wellek *et al.* (1966) for the bubble shape parameter $\frac{c}{a}$ in contaminated liquids:

$$\frac{c}{a} = \frac{1}{1 + 0.163 {E_o}^{0.757}}, \tag{3.23}$$

with $E_o = \frac{g\rho_l {D_b}^2}{\sigma}$ and $D_b = 2(a^2 c)^{\frac{1}{3}}$. For pure liquids, available correlations are predicting more important bubble deformations (Clift *et al.*, 1978), leading to lower values of the bubble shape parameter $\frac{c}{a}$. During our multiple bubbles experiments, we used non-filtered tap water with 0.5% volume ethanol ($\sigma = 68mN/m$). This corresponds to non-pure water conditions. We therefore expect our bubble shape measurements to be described by equation (3.23). In figure (3.43), our measurement results are compared with this correlation. In this figure a four-point probe measurement at the pipe centreline was used and our bubble-reconstruction algorithm was applied. A reasonable comparison of the bubble shape changes with the Eötvös number is found. The scatter in the measured bubble aspect ratio associated with a given bubble size is attributed to the bubble shape oscillations: our method provides a quasi-instantaneous estimate of the bubble geometrical parameters, which deviates form the mean value correlation.

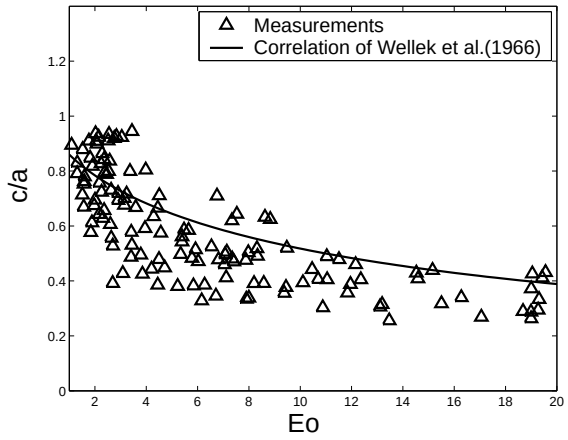

Figure 3.43: Bubble shape parameter $\frac{c}{a}$ obtained from our method as a function of the Eötvös number during a four-point probe measurement at the centreline of the pipe. Also the correlation of Wellek *et al.* (1966) is plotted.

3.5.5.3 Wall to core peaking void fraction profile

As already reported (Liu, 1993a; Tomiyama *et al.*, 2002b), we observed that small bubbles (typically $D_b < 5$ mm) were accumulating in the near wall region during our pipe flow experiments to form a wall peaking radial profile of void fraction. When increasing the bubble size, the void fraction profile changed from a wall peaking radial profile to a centreline peaking radial profile.

Assuming that ellipsoidal bubbles are travelling along their minor axis, the formation of the wall peaking void fraction radial profile associated with small bubbles is expected to be associated with a mean bubble orientation as depicted in figure 3.44, corresponding to $0 < \gamma < \frac{\pi}{2}$. In that case, the bubbles are expected to be pierced firstly by fibre 2, since $\gamma > 0$. Larger bubbles, migrating toward the pipe centreline, would lead to $-\frac{\pi}{2} < \gamma < 0$. We make a first estimate of the orientation angle of the bubbles by comparing the individual piercing times of fibres (1), (2) and (3). In figure 3.45 the radial distribution of the probabilities P_i associated with an experiment corresponding to wall peaking void fraction radial profile conditions are presented. It is clearly suggested from the large values of P_2 in the near wall region, that the bubbles had the tendency of having a preferential orientation as depicted in figure 3.44 in this flow region. Assuming that the bubbles are presenting a flat interface during the measurement and are travelling along their minor axis at a velocity $\vec{U}$ during the bubble-probe interaction event, the bubble angle of motion γ

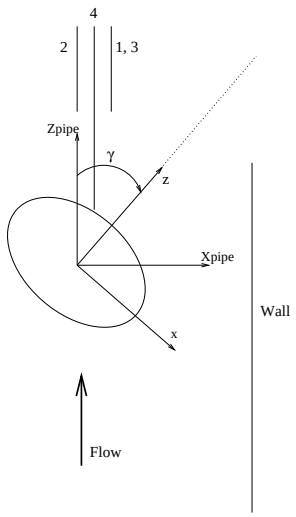

Figure 3.44: Expected bubble preferential orientation in the case of bubble migration towards the wall, i.e. at the formation of a wall peaking void fraction profile, corresponding to small bubbles. In that case, on average the fibre 2 should pierce the bubbles before fibre 1 and 3.

can be approximated by (see figure 3.46)

$$\gamma = \frac{1}{2} asin\left(\frac{U_z(2t_2 - t_1 - t_3)}{2d}\right). \tag{3.24}$$

t_1, t_2 and t_3 are the piercing times of fibre 1, 2 and 3, and $d = 0.6$ mm is the transverse distance between fibres. U_z is the vertical component of the bubble velocity, computed for each individual bubbles by using the mean time of flight method described in section 3.4.

Using this approach, the probability distribution of the orientation angle γ can be computed. The results are presented for the centreline measurement ($r = 0$) and near

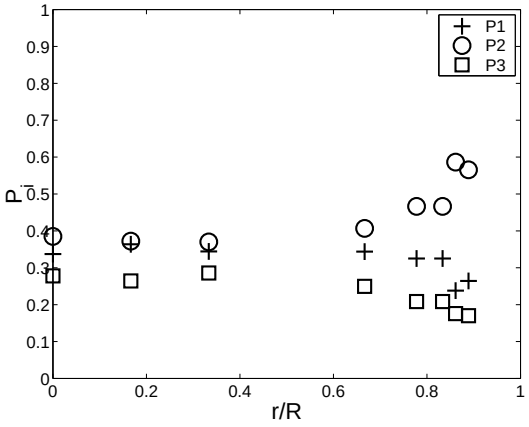

Figure 3.45: Radial distribution of the relative probability P_i that fibre i will pierce the bubble first, where $i = 1$, 2 and 3. In that case the void fraction radial profile is wall peaking.

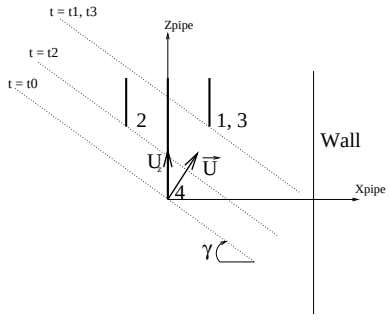

Figure 3.46: Simplified situation for evaluating the mean orientation angle γ of the bubbles. The dotted line represents the bubble interface at $t = t_0$, $t = t_2$ and $t = t_1, t_3$.

the wall ($r = 31mm$, i.e. $\frac{r}{R} = 0.86$) in figure 3.47 for the small bubble wall peaking flow conditions used previously. As expected, at the centreline the distribution is relatively symmetric, while at the near wall boundary, the asymmetry in the probability density function clearly points to a preferential orientation tendency (the peak occurs at $\gamma > 0$). The symmetric character of the mean bubble motion at the pipe centreline was also confirmed by applying our new method to the collected data.

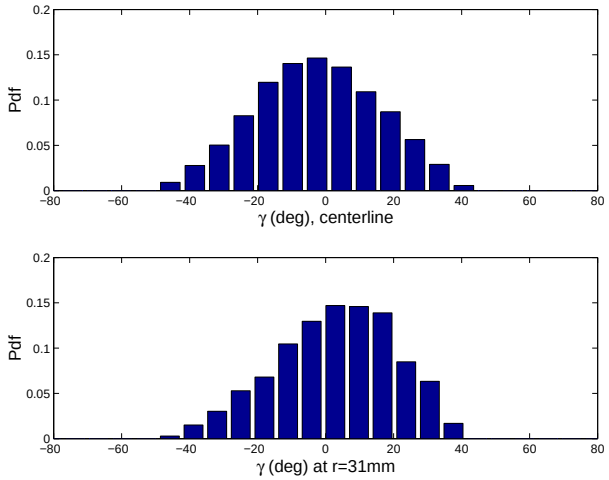

Figure 3.47: Probability density function of the angle of orientation γ for $r = 0$ and $r = 31mm$ and during a wall peaking void fraction profile experiment.

3.5.5.4 Bubble orientation changes with shape

We investigated the angle of orientation γ of individual bubbles by applying our method to the collected four-point probe signal near the wall (i.e. in the presence of shear). Using our evaluation method, the angle of orientation γ is obtained by computing the bubble minor axis in the pipe frame of reference $(\vec{X_{pipe}}, \vec{Y_{pipe}}, \vec{Z_{pipe}})$. For this purpose we apply an additional rotation matrix $\underline{\mathbf{R}}_{pipe}$ around the optical fibre axis (see figure 3.44). The bubble minor axis in the pipe frame of reference is computed from $\vec{Z_{bub,pipe}} = \underline{\mathbf{R}}_{pipe}(\underline{\mathbf{R}}_{op}.\vec{z})$. The physical angle γ is then given by

$$\gamma = tan^{-1}\left(\frac{\vec{Z_{bub,pipe}}.\vec{x}}{\vec{Z_{bub,pipe}}.\vec{z}}\right). \tag{3.25}$$

In figure 3.48, the bubble angle of motion γ as obtained with equation (3.25) (by applying our method) is plotted as a function of the bubble aspect ratio $\chi = \frac{a}{c}$, for a measurement in the near wall region of our pipe flow. Although some scattering is obtained due to the instantaneous character of the bubble parameters provided by our technique, the results point to a changing bubble angle of motion γ with an

increased bubble aspect ratio χ. Increasing bubble deformation leads to negative values of γ, associated with a bubble migration toward the pipe centreline.

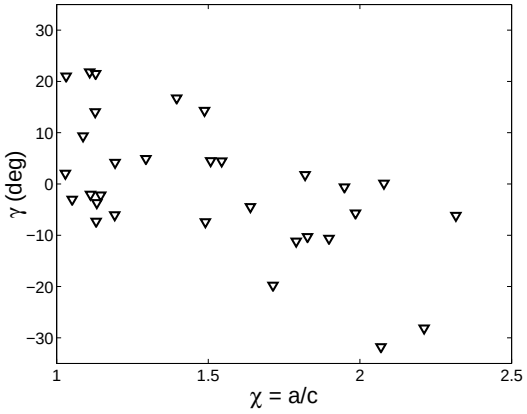

Figure 3.48: Bubble angle of orientation γ versus bubble aspect ratio $\chi = \frac{a}{c}$, for a near-wall measurement ($r = 31$ mm).

3.5.6 Conclusion

A new algorithm for the evaluation of four point optical fibre probe signals has been developed for estimating the bubble orientation and shape. Using synthetic data the bubble orientation information provided by the numerical method has been evaluated. A good accuracy was found. The evaluation and validation of the method with experimental data was done by simultaneous measurements of the bubble-probe interactions with high-speed stereoscopic imaging and recording of the probe signal. The method was then applied to four-point probe measurements collected on a vertical upward bubbly pipe flow. The bubble aspect ratio results were supported by an available correlation.

Some first results about the bubble orientation as a function of the shape in shear flows were presented. Those results were supported by the observations reported in literature on bubble transverse migration in pipes. An interesting subject of further research would be to analyse in more details the bubble orientation and shape conditions associated with bubble transverse migration in multiple-bubbles shear flows. Such results could be compared with the available literature on the effect of single bubble deformation on the transverse lift force (Ford and loth, 1998; Tomiyama *et al.*, 2002b).

Chapter 4

Bubble injector effect on the gas-lift efficiency*

Abstract

An experimental investigation is made of the influence of the (initial) bubble size and bubble concentration distribution on the gas-lift efficiency for a vertical air-water flow through our vertical pipe of $72mm$ diameter and $18m$ height. Three significantly different bubble injectors are used. It is found that with decreasing bubble size the liquid production increases at constant gas flow rate and, hence, the gas-lift efficiency increases. Also the initial concentration distribution can be important, as this distribution can influence the coalescence of bubbles close to the injector. With decreasing bubble size the transition from bubbly flow to slug flow can be postponed. This is one of the main reasons for the beneficial effect of the bubble size on the gas-lift efficiency. A model is developed to predict the influence of the bubble size on the gas-lift efficiency. The agreement is reasonable.

4.1 Introduction

In the oil industry the gas-lift technique is often applied. This gravity-driven pumping technique enhances oil production by injecting gas in the production pipe and, in this way, lowering the bottom-hole pressure to enable more inflow of oil into the well bore. In practice the diameter of the production pipe is of the order of $60mm$ to $90mm$. The Reynolds number of the oil flow is (at conditions where gas-lift is considered) rather low ($Re_{sl} \approx 10000$). The gas is injected from valves attached to the pipe wall. Large bubbles are generated with a non-symmetric initial radial distribution. This chapter reports about a study of the possibility to improve the efficiency of the gas-lift technique by injecting small bubbles. Previous laboratory experiments (Van Geest *et al.*, 2001) with water and air indicated already, that the gas-lift efficiency can be improved by injecting small bubbles via a special inlet device consisting of a porous material. As compared to the standard gas injection via large nozzles as used in practice, the liquid (water) production was remarkably higher.

*See also: S. Guet, G. Ooms, R.V.A. Oliemans & R.F. Mudde. (2003). *AIChE J.*, 49, 2242-2252.

The size of the generated bubbles influences the gas-lift technique in several ways. First, small bubbles have a lower rise velocity in the liquid than large ones (section 2.1.2). Hence the average gas concentration in the production pipe is for small bubbles higher than for large bubbles (at the same gas-injection rate). This means that the average density of the mixture is lower and the liquid production larger. A second effect is, that the bubble size is known to have a drastic influence on the evolution of the radial gas fraction distribution (section 2.1.3). Small bubbles in an upward flow move towards the pipe wall, whereas large bubbles move to the centre of the pipe. This is related to the interaction between the wake of the bubbles and the velocity distribution of the liquid (Tomiyama *et al.*, 2002b). For this reason the small bubbles are more evenly distributed over the cross-section of the pipe (compared to large bubbles) and, therefore, the average gas concentration is (again) larger. Thirdly, the size of the bubbles is observed to influence the transition from bubbly flow to slug flow (Song *et al.*, 1995). Bubbly flow is still possible with small bubbles at relative large values of the average gas fraction, where for the case of large bubbles slug flow would be present. The relatively large slug bubbles have a high-rise velocity (compared to the small bubbles) and cause a relatively low average gas concentration in the pipe and thus a lower liquid production.

The objective of the present chapter is to report about an experimental investigation carried out to study in more detail the effect of the bubble size on the gas-lift technique, by using local bubble size and void fraction measurements. Next to the gas-lift efficiency special attention will be paid to the influence of the bubble size on the average gas concentration, on the transition from bubbly flow to slug flow, and on the radial gas concentration distribution. We used an $18m$ height vertical pipe with a diameter of $72mm$. The liquid was water and the injected gas was air. Also some experimental results are reported where a surfactant is added to the water in order to reduce the surface tension and, in this way, make a more realistic simulation of practical conditions. The effect of an increased liquid viscosity is also discussed. Three different injectors, described in section 3.1.3 were used to generate bubbles of different sizes and different initial radial concentration distribution. Single and four-point optical fibre probes were used to measure the void fraction, bubble sizes and velocities.

In section 4.2 we discuss first an empirical relation for the transition from bubbly flow to slug flow. This relation plays an important role in the interpretation of the measurement results. In section 4.3 the results about the influence of the three different inlet conditions (different initial bubble size and different initial radial bubble concentration distribution) on the gas-lift efficiency, the flow pattern transition and the radial bubble concentration distribution will be discussed. In section 4.4 a bubble-size and flow pattern dependent model for the gas-lift efficiency will be introduced and compared with experimental data.

4.2 Flow pattern characterisation

4.2.1 Low-liquid-input to finely-dispersed bubbly flow

Bubbly pipe flows can be separated into two sub-regimes (Taitel et al 1980; Chen et al 1997): low-liquid-input bubbly flow, for which bubble break-up due to pipe flow turbulence is absent, and high-liquid-input bubbly flow (also called finely-dispersed bubbly flow), for which the turbulence intensity is determining the maximum bubble size (Levich, 1962; Hinze, 1975). By equating the total turbulent kinetic energy of the liquid phase to the total surface free energy of the dispersed phase, Chen *et al.* (1997) proposed a model for the transition from low-liquid-input bubbly flow to finely-dispersed bubbly flow. It was compared with experiments performed on pipes of $25mm$ to $127mm$ diameter. The result of this model is plotted in figure 4.1 for a water-air flow and a pipe diameter $D_p = 72mm$ as used in our experiments. The range of our liquid flow conditions is also plotted. It is clear, that for our experiments bubble break-up due to pipe flow turbulence is absent. Therefore the size of the bubbles will mainly be dependent on the injector outlet conditions and their associated mixing regions.

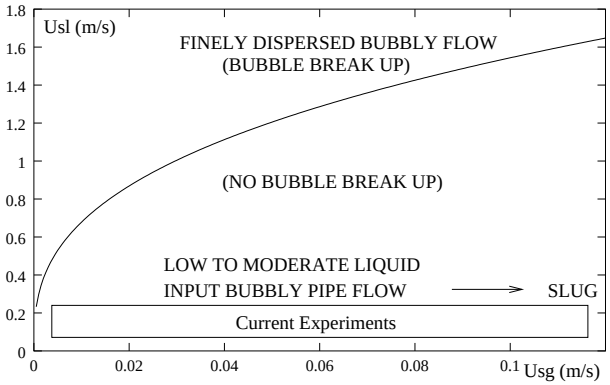

Figure 4.1: Boundary between low-liquid-input bubbly flow and finely-dispersed bubbly flow for an air water system of $72mm$ diameter according to Chen et al.(1997). The bubbly flow to slug flow transition occurs in the right part.

4.2.2 Bubbly flow to slug flow transition

Taitel *et al.* (1980) assumed that the transition from bubbly flow to slug flow occurs when the gas velocity is equal to the rise velocity of large bubbles moving with respect to the averaged liquid velocity and when the void fraction has a certain critical value. Harmathy (1960) proposed the following expression for the rise velocity:

$$U_t = 1.53 \left(\frac{g(\rho_l - \rho_g)\sigma}{{\rho_l}^2} \right)^{\frac{1}{4}}, \tag{4.1}$$

where ρ_l is the liquid density, ρ_g the gas density and σ the surface tension. Applying the assumption of Taitel *et al.* (1980) the following relation holds between the superficial liquid velocity U_{sl} and superficial gas velocity U_{sg} at the transition from bubbly flow to slug flow:

$$U_{sl} = U_{sg}\frac{1- < \epsilon >}{< \epsilon >} - (1 - < \epsilon >)U_t, \tag{4.2}$$

in which $< \epsilon >$ is the cross-section averaged value of the gas fraction and U_t is given by (4.1). As mentioned this transition relation only holds when the gas fraction $< \epsilon >$ is equal to the critical gas fraction ϵ_c for flow pattern transition. By using some geometrical considerations Taitel *et al.* (1980) suggested $\epsilon_c = 0.25$. Other studies proposed $\epsilon_c = 0.30$ (for example Mishima and Ishii (1984)), while the maximum gas fraction considering packed spherical shaped bubbles in a cubic lattice is $\epsilon_c = 0.52$. In a body centred cubic configuration, $\epsilon_c = 0.68$. A generally accepted expression for the critical gas fraction is still lacking. Song *et al.* (1995) found a strong dependence of the transition from bubbly flow to slug flow on the injected bubble size when carrying out experiments in a narrow pipe ($25mm$ diameter). An expression for the critical gas fraction ϵ_c as a function of the non dimensional bubble size D_b/D_p was found from an interpolation of their experiments:

$$\epsilon_c(D_b/D_p) = 0.55 - 2.37\frac{D_b}{D_p}, \tag{4.3}$$

where D_b is the bubble diameter. Cheng *et al.* (2002) mentioned also this effect of the bubble size on the critical gas fraction corresponding to flow pattern transition by using a $28.9mm$ diameter pipe.

For small pipe diameters the initial bubble diameter can easily be of the order of the pipe diameter if no special attention is paid to the bubble inlet geometry. In such cases break-up of large bubbles due to turbulence is necessary for a bubbly flow to develop. According to Taitel *et al.* (1980) low-liquid-input bubbly flow is only possible when the pipe diameter is above a critical value, corresponding to $D_p > 52mm$ for an atmospheric pressure air-water flow. For very-large diameter pipes the flow pattern is still rather uncertain. For instance Cheng *et al.* (1998) studied the flow pattern in a $150mm$ diameter pipe, and found no slug flow but a churn-like flow pattern for the conditions of slug flow in a smaller-diameter pipe. Ohnuki and Akimoto (1996) mentioned also the occurrence of churn-like structures in a $200mm$ diameter pipe.

We will apply the correlation (4.3) for an air-water flow through a $72mm$ diameter pipe; the range of bubble diameter to pipe diameter being similar to the Song *et al.* (1995) experiments: $0.1 < \frac{D_b}{D_p} < 0.2$. Our criterion for the bubbly flow to slug flow transition is thus given by:

$$U_{sl} = U_{sg}\frac{1 - \epsilon_c(D_b/D_p)}{\epsilon_c(D_b/D_p)} - (1 - \epsilon_c(D_b/D_p))U_t \tag{4.4}$$

where U_t is given by equation (4.1) and (4.3) is used for $\epsilon_c(D_b/D_p)$.

4.3 Results

4.3.1 Inlet characterisation

For this investigation, we used the injectors corresponding to the annular porous, the long porous and the large nozzle described in section 3.1.3 and represented in figure 3.2. A four-point probe, as sketched in figure 3.17, was used for the measurement of the vertical bubble velocity and vertical chord length of the bubbles. The individual bubble velocity was determined by using the bubble mean time of flight between the central fibre tip 4, situated upstream (see figure 3.17) and the 3 other fibre tips (1, 2, 3) situated downstream (see section 3.4).

In order to characterise the three inlet devices the mean vertical chord length of the bubbles was measured with the four-point probe for each inlet device at $h = 5m$ (i.e. $h/D_p = 70$). For this characterisation the liquid flow was kept constant at $U_{sl} = 8.2cm/s$, and the superficial gas velocity was increased from $1cm/s$ to the gas input needed for observing bubbly flow to slug flow transition (up to $9cm/s$ for the annular porous inlet). Since the largest bubbles are known to be in the core region of the pipe (Liu, 1993a; Lucas *et al.*, 2001), the centreline value of the bubble diameter was used for the inlet characterisation. The four-point probe signal analysis, explained in section 3.4 was applied. Averaging was carried out over at least 500 selected bubbles, i.e. measurement times of 5 to 10 minutes. For high void fraction ($\epsilon > 0.1$) the typical frequency of selected bubbles was 3 to 10 bubbles/s, leading to more than 1000 selected bubbles per experimental point. The results are given in figure 4.2.

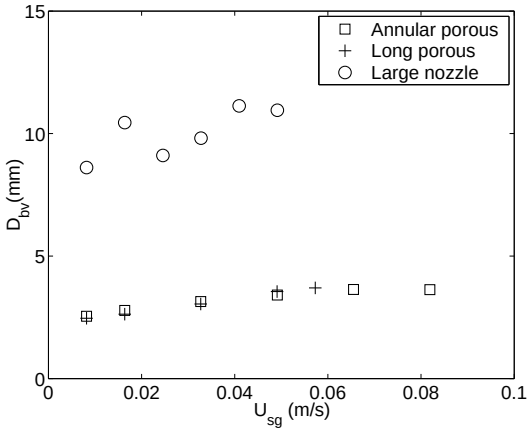

Figure 4.2: Mean bubble vertical chord length at $U_{sl} = 8.2cm/s$ measured at $\frac{h}{D_p} = 70$ on the pipe centreline and using the three different inlets. The largest gas superficial velocity points for each injector is close to the transition to slug flow.

The mean vertical chord length resulting from the two porous inlets at low gas flow rate are nearly equal, ranging from 2.4 to 3.7mm. This confirms that the porous material areas are similar (Koide *et al.*, 1968). In contrast to the porous inlets, the large nozzle inlet was creating much larger bubbles (figure 4.2). The mean vertical chord length was in that case of the order of 8.5 to 11mm. The probability density function (PDF) for the bubble size was similar for the two porous inlets when the superficial gas velocity was low (figure 4.3), i.e. for low gas concentration near the inlets. When the gas flow rate was increased, coalescence occurred for the long porous inlet in the vicinity of the porous material (where the gas concentration was high) resulting in a somewhat wider distribution of the vertical chord length (figure 4.3.c) and a shift to the right of the density distribution.

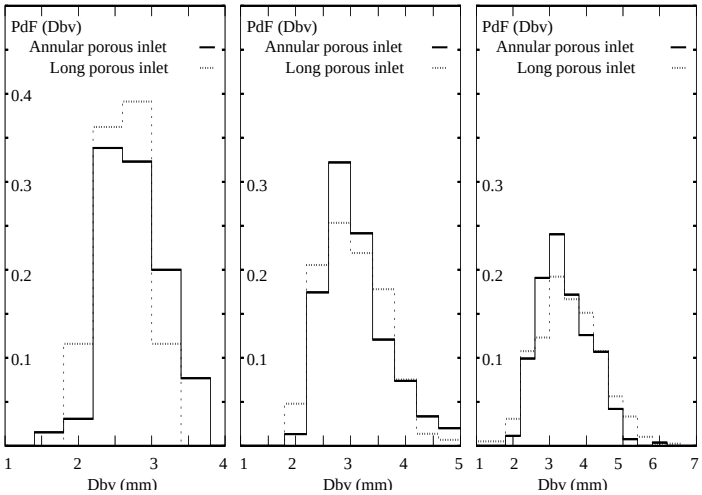

(a) $U_{sg} = 1.65cm/s$ (b) $U_{sg} = 3.3cm/s$ (c) $U_{sg} = 4.9cm/s$

Figure 4.3: PDF of bubble vertical chord length for the porous medium inlets, measured at $\frac{h}{D_p} = 70$ at the pipe centreline. From (a) to (c) the superficial gas velocity is increased.

The PDF of vertical chord length for the large nozzle showed a much wider distribution than for the porous inlets. Two peaks appeared (figure 4.4), due to the presence of two groups of bubbles, namely ellipsoidal bubbles with a typical vertical chord length between 1 and 10mm and spherical cap bubbles having a larger vertical size.

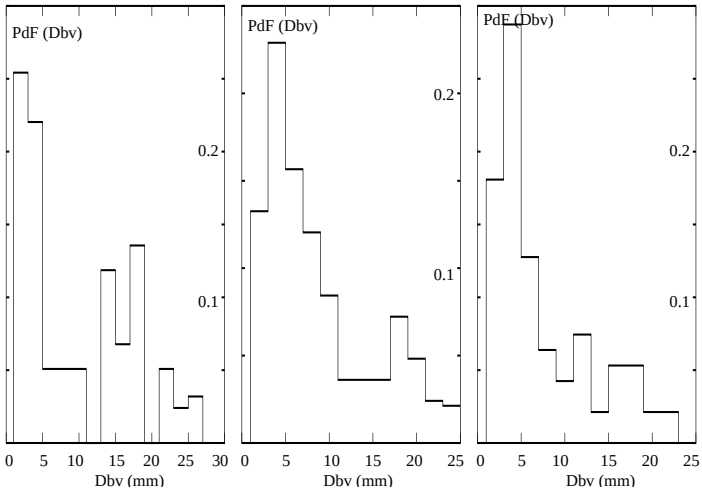

(a) $U_{sg} = 1.65cm/s$ (b) $U_{sg} = 3.3cm/s$ (c) $U_{sg} = 4.9cm/s$

Figure 4.4: PDF of bubble vertical chord length for the large nozzle inlet, measured at $\frac{h}{D_p} = 70$ at the pipe centreline. From (a) to (c) the superficial gas velocity is increased. In (c) the flow pattern transition is approached.

4.3.2 Gas-lift experiments

4.3.2.1 Gas-lift efficiency and bubbly flow to slug flow transition

Under normal gas-lift conditions no additional liquid pumping was applied. The liquid flow was only due to the gas injection. The gas flow rate was increased by small steps, and the axial pressure drops and re-circulating liquid flow (after reaching equilibrium) were measured. The gas-lift efficiency can be evaluated in two ways. First, the generated liquid flow for a given gas flow is a measure of the efficiency of the technique. The second measure is the ratio of the pressure drop over the gas-lift pipe for a certain value of the generated liquid flow, ΔP_m, and the pressure drop over the pipe for the same liquid flow and without gas injection, ΔP_l (we call this ratio $\frac{\Delta P_m}{\Delta P_l}$ the normalised pressure drop). In figure 4.5 the normalised pressure drop between $h = 2m$ and $h = 18m$ is presented for each of the three bubble injectors when operating in bubbly flow. It is evident, that the annular porous inlet is the most efficient in reducing the hydrostatic pressure drop. In figure 4.6 the superficial liquid velocity generated by the injected gas flow is presented in a U_{sg} versus U_{sl} plot, where the superficial gas velocity is given at atmospheric pressure. The observed transition points from bubbly flow to slug flow coincide with the local change of slope on the curves for the porous inlets. These local changes of slope are due to a decrease of the gas concentration in the tube when the first slug bubbles are observed, since slug bubbles are having a significantly larger rise velocity than millimetre-size bubbles. For the large nozzle inlet, the transition occurs at much lower gas and liquid flow rates (i.e. at the third point on the left of the curve). The Taitel *et al.* (1980) criterion for the bubbly flow to slug flow transition (with

$\epsilon_c = 0.25$) is also plotted on the figure. This illustrates, that this criterion cannot be generally valid. It is clear from figure 4.6, that the liquid flow rate generated by the injected gas flow and also the points of transition from bubbly flow to slug flow are strongly affected by the type of bubble injector.

A significant difference between the porous inlets (generating small bubbles) and the large-nozzle inlet (generating large bubbles) can be observed, even when both

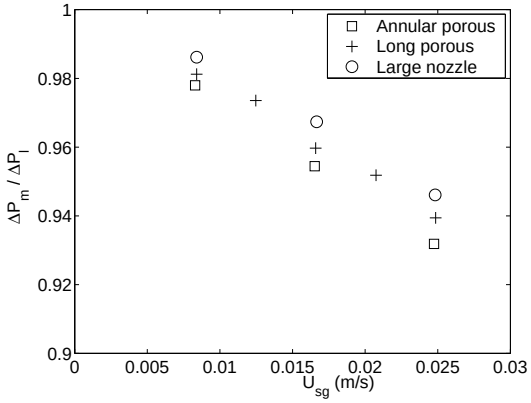

Figure 4.5: Normalised pressure drop for bubbly flow conditions as a function of the superficial gas velocity for the three different bubble injectors. Due to the difference in slip velocity and void fraction distribution, the annular porous inlet is the most efficient in reducing the pressure drop.

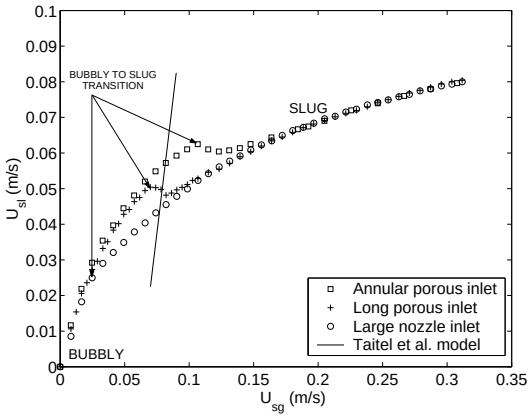

Figure 4.6: Liquid flow as a function of the injected gas flow for the normal airlift case and using the three different inlets. The Taitel et al.(1980) criterion for flow pattern transition is also plotted.

types of inlets are in the bubbly flow regime. Small bubbles are more efficient than large bubbles in generating a liquid flow, since they lead to higher gas fractions in the pipe due to their lower rise velocity and their capability to postpone the transition from bubbly flow to slug flow to larger values of the gas concentration. Similar results will be obtained when scaling the oil properties with an increased viscosity and a decreased surface tension (section 4.3.2.4).

4.3.2.2 Void fraction profiles

The gas fraction profiles measured under airlift conditions at $h = 8m$ for the three different bubble injectors are presented in figure 4.7. For small bubbles at low gas flow rate conditions (far away from the bubbly flow to slug flow transition boundary) the profiles are flat with a wall peaking profile (see the curves for the porous inlets in figure 4.7). However, when injecting large bubbles the profiles are core peaking (see the curve for the large nozzle inlet in figure 4.7). During the experiments it was observed, that the transition from bubbly flow to slug flow always starts from flow conditions with a core peaking profile. The airlift efficiency was found to be better when operating at wall peaking conditions than at core peaking conditions (figures 4.5, 4.6 and 4.7).

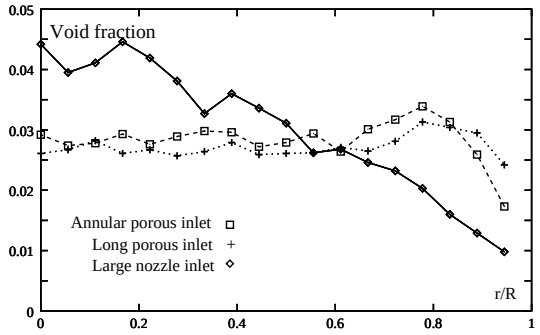

Figure 4.7: Radial void fraction profile measured at $\frac{h}{D_p} = 110$, $U_{sg} = 0.016ms^{-1}$ (i.e. far from the transition boundary) and using the three bubble inlets.

The gas fraction profiles corresponding to the two porous inlets at low gas flow rate conditions are similar at $h/D_p = 110$, showing that the initial distribution of the bubbles is not relevant in itself for the downstream development of the radial gas fraction profile at low void fraction. This also proves that the wall peaking behaviour is not an entrance effect. However, the transition from wall peaking to core peaking was occurring at a lower gas fraction for the long porous inlet than for the annular porous inlet. This was due to some quick bubble coalescence near to the porous surface of the long porous inlet.

Due to the decrease in pressure with height the bubbles grow in size with height in the pipe. As larger bubbles have the tendency to move to the pipe centre, it can be expected that the bubble distribution goes from wall peaking to core peaking. Figures 4.8 and 4.9 show indeed (for the annular porous inlet) the evolution from

wall peaking to core peaking with height at $U_{sg} = 0.016ms^{-1}$ and $U_{sg} = 0.04ms^{-1}$. The core peaking radial profile was rapidly reached (at $\frac{h}{D_p} = 160$ in figure 4.9), probably due to the interaction between the wake of the bubbles and the shear in the liquid flow (Tomiyama *et al.*, 2002b).

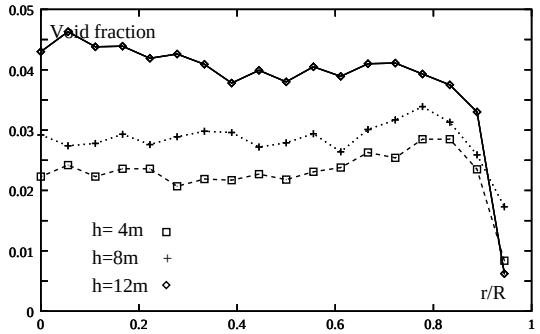

Figure 4.8: Radial void fraction profile evolution with height, measured at $\frac{h}{D_p} = 56$; 110 and 166, $U_{sg} = 0.016ms^{-1}$ and using the annular porous inlet. The profile remains wall peaking to flat with height.

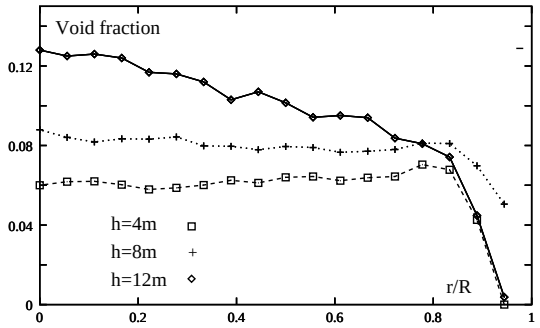

Figure 4.9: Radial void fraction profile evolution with height, measured at $\frac{h}{D_p} = 56$; 110 and 166, $U_{sg} = 0.04ms^{-1}$ and using the annular porous inlet. The profile evolves from wall peaking to core peaking with height. At this particular gas flow value, the bubble diameter is $D_b \approx 5.5mm$.

4.3.2.3 Experiments at reduced surface tension

Decreasing the surface tension reduces the size of the generated bubbles (Koide *et al.*, 1968) and limits coalescence. Experiments with 0.5 percent volume ethanol in water showed indeed for the case of the annular porous inlet, that the bubble diameter was much smaller ($D_b \approx 1-2mm$ according to photos for the water-ethanol solution, compared to $D_b \approx 2-8mm$ for water). The wall peaking profile was kept for much larger height to diameter ratios. The associated airlift production curve in bubbly flow was showing a remarkable improvement as compared to the water results (figure 4.10). Also the transition from bubbly flow to slug flow was postponed to larger critical void fraction values compared to the water experiments.

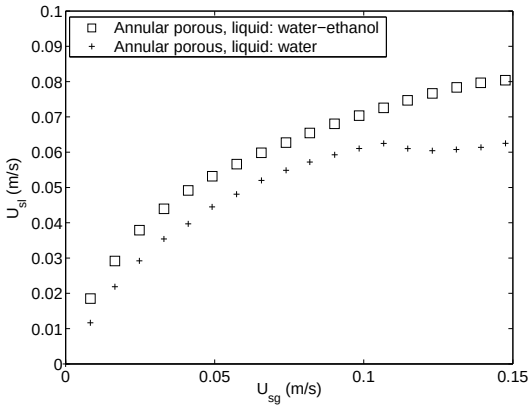

Figure 4.10: Liquid flow as a function of the injected gas flow for the normal airlift case and using water and water + 0.5 percent volume ethanol in solution. The estimated bubble diameter in the ethanol solution is $D_b \approx 1-2mm$.

4.3.2.4 Scaling-liquid experiments

In this section, we report gas-lift experiments carried out at increased viscosity. For scaling the flow of viscous oil during gas-lift operations, we used a solution consisting of water and 40 % volume glycerol. The (measured) properties of this mixture were the following: $\rho_l = 1112kg.m^{-3}$, $\sigma = 67mN/m$ and $\mu = 4.6mPa.s$. These values allow for scaling the bubble size effects at low pressure, gravity-driven gas-lift conditions, as discussed in section 2.3. In figure 4.11, we present the measured liquid superficial velocity as a function of the gas superficial velocity for our three different bubble injectors (1), (2) and (3) when using this liquid solution on our gas-lift experimental set-up. The experimental results are similar to the results obtained for water (figure 4.6 in section 4.3.2). The wall-peaking radial distribution of void fraction was also measured when using this liquid phase. A larger improvement due to the reduced bubble size generated from the porous inlets is found when operating in bubbly flow compared to the water experiments. This is attributed to a reduced bubble relative velocity. Also, the decreased surface tension value compared to

water contributed in reducing the bubble diameter, similarly to the water-ethanol tests reported in figure 4.10.

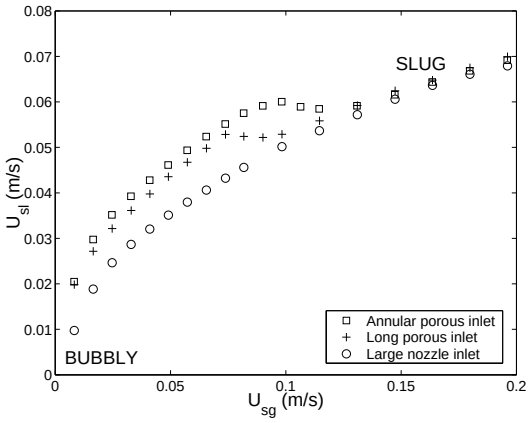

Figure 4.11: Liquid flow as a function of the injected gas flow during gas-lift experiments, and using the three different inlets in the glycerol-water solution. The results are similar to the water experiments reported in figure 4.6.

4.3.3 Forced liquid flow experiments

4.3.3.1 Bubbly flow to slug flow transition

A centrifugal pump was used in the experimental set-up depicted in figure 3.1 for making measurements at forced liquid flow rates. Particular attention was given to the measurement of the transition from bubbly flow to slug flow at various pump conditions by using water as the liquid phase. For a given pump setting, the gas flow rate was increased by small steps, starting with bubbly flow and leading to the transition to slug flow. The flow pattern transition was determined from the pressure signal, since it became strongly non-stationary under conditions of slug flow. This was also confirmed by visual observation. In figure 4.12 all the measured transition points obtained with the three inlets are presented. As expected the transition points are again strongly dependent on the type of bubble injector. In the figure also a comparison is made with model predictions from equation (4.4). The best fit was found when choosing $D_b = 7mm$ (for the annular porous inlet) and $13mm$ (for the large-nozzle inlet). As mentioned this model involves the use of the relation of Song et al.(1995) for the critical void fraction in the Taitel *et al.* (1980) criterion, combined with the Harmathy (1960) expression.

It is interesting to compare the bubble diameters chosen to give the best fit in figure 4.12 with the actually measured bubble diameters. The mean bubble size D_b of the ellipsoidal bubbles generated by the inlets were evaluated from the measurements of the vertical chord length D_{bv} and an estimate of the bubble aspect ratio χ by

means of the following relation:

$$D_b = D_{bv}\chi^{\frac{2}{3}}. \tag{4.5}$$

For the long and the annular porous inlet the bubble vertical chord length was $3.6mm$ near the transition (figure 4.2). The aspect ratio was determined by making use of photos, leading to $\chi = 2.5$ and $D_b = 7mm$ for the porous inlets. This is in agreement with the chosen value for the bubble diameter of the annular porous inlet.

The transition points for the long porous inlet are shifted to the left compared to those for the annular porous inlet. This is caused by the fact, that the bubbles were generated perpendicularly to the flow in the case of the long porous inlet. This resulted in an increased gas flow re-circulation and a tendency of keeping the bubbles in the plume close together, when the gas and liquid flow rates were increased. Those effects are illustrated with photos of the long porous inlet mixing region for different flow conditions in figure 4.13. They cause coalescence of the bubbles near the long porous inlet. This coalescence (causing larger bubbles) initiated a transition to slug flow at (nearly) fixed gas flow conditions (figure 4.12). Therefore, not only the initial bubble size is important, but also the initial bubble concentration distribution.

The large nozzle inlet was generating both ellipsoidal shaped bubbles and spherical cap bubbles. If the vertical chord length was larger than $10mm$, the bubbles were treated as spherical cap (according to $E_o = \frac{g\rho_l {D_b}^2}{\sigma} > 40$, Tomiyama et al. 1998). For smaller chord length, the bubbles were assumed to be ellipsoidal shaped. This leads to $D_b = 12.2mm$ at the transition from bubbly flow to slug flow. This is again in reasonable agreement with the chosen value of $D_b = 13mm$ for the large nozzle inlet.

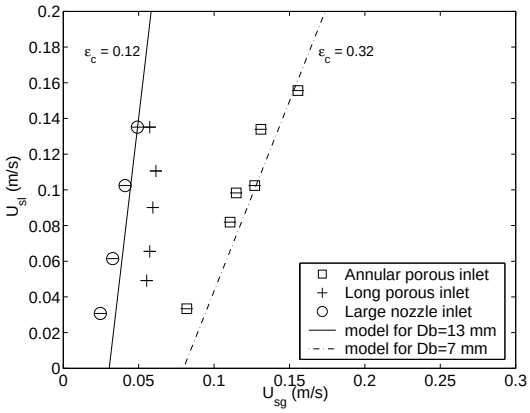

Figure 4.12: Bubbly flow to slug flow transition points for the three inlets. U_{sg} is given at atmospheric pressure.

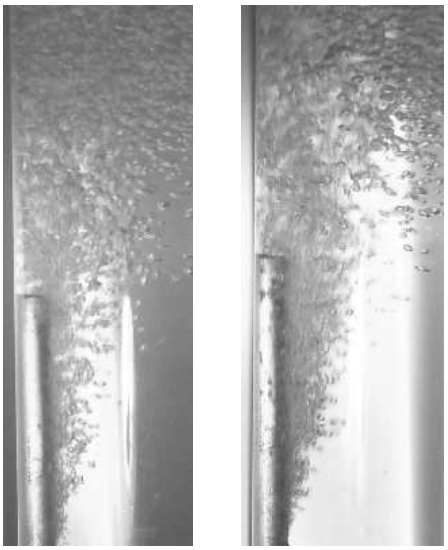

(a)$U_{sg} = 1.65cm/s$ (b)$U_{sg} = 3.3cm/s$

Figure 4.13: Bubble concentration distribution in the mixing zone of the long porous inlet for two gas flow rates.

4.3.3.2 Average gas fraction and gas-lift efficiency

In the range of low liquid flow conditions of our experiments the contribution of friction and acceleration to the pressure drop is negligible.
Since $< \epsilon > \rho_g << (1 - < \epsilon >)\rho_l$, the average gas fraction can be estimated from pressure drop measurements by means of

$$< \epsilon > = 1 - \frac{\Delta P}{\Delta h \rho_l g}, \tag{4.6}$$

where ΔP is the pressure difference between two measurement points and Δh the distance between these points. The contribution of the air density is neglected because of the low pressure conditions used. We used this equation to calculate the average gas fraction from the measured pressure drop at the transition from bubbly flow to slug flow. Since this transition always started at the top of the pipe, the pressure drop was calculated by using the pressure difference between $h_1 = 12m$ and the top (i.e. $h_2 = 18m$). The average gas fraction between h_1 and h_2 associated with flow pattern transition, calculated from the average pressure drop was 0.3 for the annular porous inlet, which is comparable to $\epsilon_c(D_b = 7mm, D_p = 72mm) = 0.32$ calculated from the Song et al.(1995) correlation (4.3). The average gas fraction for the large nozzle inlet at transition (calculated from the measured pressure drop) is 0.1, while the Song et al. correlation predicts $\epsilon_c = 0.12$. This shows that this correlation gives reliable predictions. It also confirms that the average gas fraction for bubbly flow to slug flow transition is strongly affected by the size of the injected bubbles. Moreover it proves again, that the gas-lift efficiency is significantly increased when using small bubbles (as a larger gas fraction means a smaller pressure drop).

4.4 A simplified bubble-size dependent pressure drop model

As mentioned in the introduction, the effect of the bubble size on the gas-lift efficiency can be split into the following three parts: small bubbles have a lower rise velocity than large bubbles, small bubbles postpone the transition from bubbly flow to slug flow compared to large bubbles, and small bubbles distribute more evenly over the pipe cross section than large bubbles. A simple theoretical model was developed, based on the drift-flux model of Zuber and Findlay (1965), to predict the overall effect of the bubble size on the pressure gradient in a pipe under gas-lift conditions. This model is described below.

4.4.1 Bubble rise velocity

4.4.1.1 Bubbly flow

According to the Harmathy (1960) expression, given by equation (4.1), the bubble rise velocity U_t is independent of the bubble diameter. However, Peebles and Garber (1953) showed that the rise velocity of a single bubble in an infinite medium is dependent on the bubble size. As we want to study with our theoretical model the influence of the bubble diameter on the pressure drop (and thus on the gas-lift efficiency) we will apply this expression. For an air bubble in water it is given by

- $U_t = 1.35(\frac{2\sigma}{\rho_l D_b})^{\frac{1}{2}}$ for $2.1mm < D_b < 4.1mm$,
- $U_t = 1.53\left(\frac{g(\rho_l-\rho_g)\sigma}{{\rho_l}^2}\right)^{\frac{1}{4}}$ for $4.1mm < D_b < 12.4mm$,
- $U_t = (\frac{gD_b}{2})^{\frac{1}{2}}$ for $D_b > 12.4mm$.

A correction of this expression is still necessary at higher values of the bubble concentration due to the hydrodynamic interaction between the bubbles. To that purpose we introduce the bubble drift velocity U_{drift}, which is defined as the rise velocity of a bubble with respect to the mixture velocity of the two-phase system at a finite value of the gas concentration. We use the following expression for the drift velocity (Richardson and Zaki, 1954)

$$U_{drift} = U_t(1- < \epsilon >). \tag{4.7}$$

4.4.1.2 Slug flow

In case of slug flow the drift velocity of a slug bubble is given by (Clift *et al.*, 1978)

$$U_{drift,slug} = 0.35(\frac{g\Delta\rho D_p}{\rho_l})^{\frac{1}{2}}. \tag{4.8}$$

4.4.2 Flow pattern

As discussed the transition from bubbly flow to slug flow only takes place, when the gas fraction is larger than the critical value ϵ_c (which depends on the bubble size). In our model we apply equation 4.3 based on the work of Song et al.(1995) for the critical concentration. So we apply the following criterion:

- if $(<\epsilon>) < \epsilon_c$, bubbly flow is assumed to be present in the pipe,
- if $(<\epsilon>) > \epsilon_c$, slug flow is assumed to be present.

4.4.3 Radial void fraction distribution effect

For small (typically $D_b < 5.5mm$) air bubbles in water the radial gas fraction distribution is known to exhibit a peak near the wall (Serizawa *et al.*, 1975; Liu, 1993a). Larger bubbles lead to a parabolic type of profile. Tomiyama *et al.* (2002b) showed that there is a critical *Eo* number above which bubbles move from the wall to the centre region of the pipe. A related transverse lift force coefficient as function of the bubble diameter was deducted from single bubble experiments in a simple shear flow. The result is shown in figure 4.14 for air bubbles in water. Lucas *et al.* (2001) successfully applied this approach in a two-fluid model to describe wall peaking and core peaking profiles.

Following the approach of Rivière and Cartellier (1999), the wall peaking void fraction profile can be described by means of three zones; in each zone the gas fraction has a certain constant value. In between a wall peaking and core peaking profile, we describe the radial gas fraction profile by $\frac{\epsilon}{\epsilon_M} = 1 - (\frac{r}{R})^n$, in which ϵ_M is the gas fraction at the centreline of the pipe (the exponent n changes from $n = 7$ for a flat profile to $n = 2$ for a parabolic void fraction profile).

To include the effect of the bubble diameter on the radial gas fraction profile we apply the drift-flux model of Zuber and Findlay (1965). According to this model the following relation holds: $<\epsilon> = \frac{U_{sg}}{<U_g>}$ with $<U_g> = C_0(U_{sg} + U_{sl}) + \overline{U_{drift}}$, where $<U_g>$ is the cross-section averaged value of the gas velocity and C_0 is the distribution parameter. As a first approximation, the weighted mean drift velocity $\overline{U_{drift}}$ is taken as the drift velocity U_{drift} described above in equation (4.7) and (4.8). The value of the distribution parameter depends on the radial gas fraction profile and changes from $C_0 \approx 1$ for a wall peaking gas fraction profile to $C_0 \approx 1.1$ for a core peaking profile and $C_0 = 1.2$ for slug flow. For our model predictions of the flow of air bubbles in water we suggest, as a first estimate, the following values for the distribution parameter (see figure 4.14):

- if $D_b < 5.5mm$: $C_0 = 1$,
- if $D_b > 5.5mm$: $C_0 = 1.1$,
- in case of slug flow ($(<\epsilon>) > \epsilon_c$): $C_0 = 1.2$.

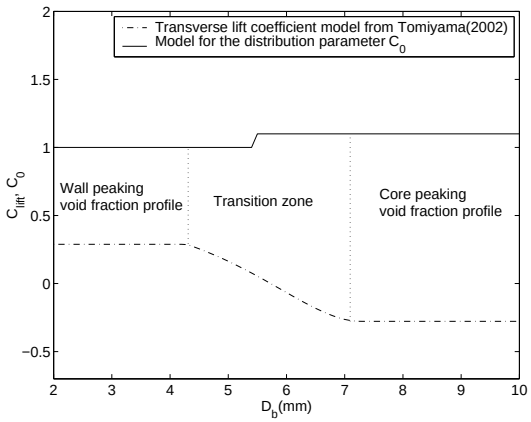

Figure 4.14: Lift force coefficient for an air-water bubble, and a model for the associated distribution parameter C_0.

4.4.4 Pressure drop predictions

We computed the pressure gradient in the pipe between $h = 12m$ and $h = 18m$ for the case of our gas-lift experiments by using the following bubble-diameter dependent calculation procedure:

1. We assume bubbly flow. From the known bubble diameter D_b the bubble rise velocity U_t and the distribution parameter C_0 are calculated by means of the expressions discussed above.

2. The averaged gas fraction $< \epsilon >$ is determined from the drift-flux model using the known values of U_{sl} and U_{sg}.

3. Using the known values of D_p and D_b, the critical gas fraction ϵ_c can be calculated from the criterion for the bubbly flow to slug flow transition given by equation (4.4). When the averaged gas fraction is smaller than its critical value bubbly flow is still assumed to be present. When it is larger slug flow is present. In that case, the slug-flow expressions for the rise velocity and the distribution parameter are applied.

4. Using the value of the gas fraction the hydrostatic pressure gradient $(\frac{\partial P}{\partial z})_H = (1- < \epsilon >)\rho_l g$ is computed.

Using the model described above the normalised pressure drop between $h = 12m$ and $h = 18m$ (in the pipe used for our gas-lift experiments) was computed for several values of the bubble diameter ($D_b = 4mm$; $7mm$ and $13mm$) representing the bubble sizes generated by the different bubble injectors. $D_b = 4mm$ and $D_b = 7mm$ represent the annular porous inlet (respectively at low and high values of injected gas). Accordingly, the superficial liquid velocities experimentally obtained with the annular porous inlet for different values of the superficial gas velocity were used in

step 2 of the calculation procedure. $D_b = 13mm$ represents the large-nozzle inlet and the superficial liquid velocities obtained for the large-nozzle inlet were applied. The theoretical predictions are given in figure 4.15 and compared with experimental data. The bends in the theoretical curves represent the transition from bubbly flow to slug flow. At low values of injected gas the predictions for the annular porous inlet are in good agreement with the experimental data for $D_b = 4mm$, and at large values of injected gas with the data for $D_b = 7mm$. This is in agreement with expectation as the bubble size generated by the porous material increases with superficial gas velocity (see figure 4.2). The transition from bubbly flow to slug flow is correctly predicted when using $D_b = 7mm$. With $D_b = 4mm$ this transition is postponed to unrealistic high values of the superficial gas velocity. The predictions for the large-nozzle inlet correctly show the negative effect of larger bubbles on the gas-lift efficiency, although the quantitative agreement between the predictions and experimental data is less good than for the annular porous inlet.

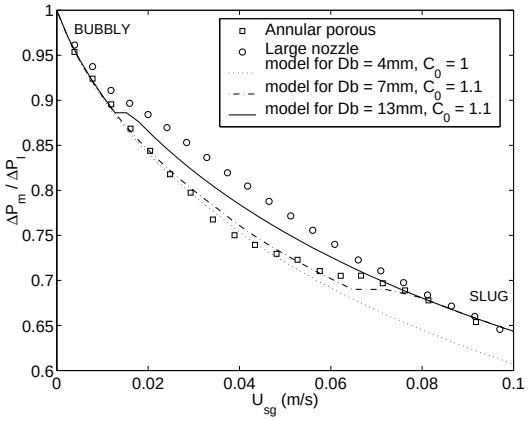

Figure 4.15: Comparison between the normalised pressure drop between $h = 12m$ and $h = 18m$ obtained with the theoretical model and from the experiments. U_{sg} is given at $h = 12m$.

4.5 Conclusion

The influence of three different bubble injectors on the gas-lift efficiency was investigated experimentally in a vertical pipe of $18m$ height and $72mm$ diameter. Three different bubble injectors were used, that had a significant influence on the initial bubble size and on the initial radial gas fraction profile. The evolution of the gas fraction profile from wall peaking to core peaking and the transition from bubbly flow to slug flow was monitored as a function of the gas flow rate and bubble size for the three injectors. The efficiency of the airlift technique was shown to be strongly dependent on the type of bubble injector. Small bubbles cause the largest gas-lift efficiency, as small bubbles have a low rise velocity and a more evenly distributed gas concentration in a pipe cross-section.

Moreover with small bubbles the transition from bubbly flow to slug flow is postponed to larger values of injected gas. The average gas fraction associated with the flow pattern transition changed from 10% to 30% when decreasing the bubble diameter from $13mm$ to $7mm$. The flow pattern transition for the three injectors used in our $72mm$ diameter air-water experiments could be predicted properly by using the expression for the critical void fraction based on the experiments of Song *et al.* (1995) for a $25mm$ diameter air-water pipe flow. However, also the geometry of the bubble generation device was found to affect the gas-lift efficiency. A difference between the annular porous inlet and the long vertical porous inlet could be observed. This was due to bubble coalescence in case of the long porous inlet close to the injector, in particular at increased gas and liquid flow rate conditions. So not only the type of injector material is important, but also the geometry of the injector surface.

Using the drift-flux model, an attempt was made to take into account the bubble size effect on the bubble rise velocity, the radial void fraction distribution, and the transition from bubbly flow to slug flow. The drift-flux parameters were however inferred by assuming some typical radial profiles in this first attempt. For the weighted mean drift velocity, the expression (4.7) was assumed. The distribution parameter was inferred by assuming some specific profiles of the void fraction and phase velocities. Although the main effects of the bubble size on the measured pressure could be properly described with this model, the contributions due to the slip velocity and transverse distribution could not be clearly separated. The gas-lift efficiency associated with large bubbles was over-predicted when operating in bubbly flow conditions (figure 4.15). This suggests either the weighted mean drift velocity or the distribution parameter to be under-estimated in those large bubble size and low liquid input conditions.

In the next chapter, we will investigate separately the contributions of the bubble relative velocity and of the radial heterogeneities of void fraction and velocity on the normalised pressure by measuring the radial profiles of void fraction and phases flux with our local measurement techniques. Using these measurements, we will compute the distribution parameter and the weighted mean drift velocity of the drift-flux model by using their definition.

Chapter 5

Bubble size effect on low liquid input drift-flux parameters*

Abstract

We investigated the effect of bubble size on the drift-flux parameters at low liquid flow conditions by measuring the radial profiles of void fraction and phase velocities in our vertical bubbly pipe flow of diameter $D_p = 72mm$ and height $18m$. To study the effect of the bubble size, we used two different types of bubble inlets, corresponding to the annular porous inlet (1) and the large nozzle injector (3) described in section 3.1. We measured the local bubble fraction and velocity U_g by using single and four-point-optical fibre probes, and we used Laser Doppler Anemometry to determine the liquid velocity U_l. The distribution parameter C_0 and the weighted mean drift velocity $|U_{drift}|$ were directly computed from local measurements. Both parameters are influenced by the bubble size. Provided no liquid flow reversal was occurring in the near wall region, the distribution parameter reached a below unity minimum plateau value of $C_0 = 0.95$ for wall peaking void fraction profiles. At low liquid input conditions, both the liquid input and bubble size had an influence on the distribution parameter and we measured extreme values such as $C_0 > 2$. From these measurements, we developed models for the drift-flux parameters to take into account the effects of bubble size and input-flow conditions for our intermediate pipe diameter value. We tested and validated these models with separately collected experimental data.

5.1 Introduction

Previous laboratory experiments with water and air indicated that the gas-lift efficiency could be improved by reducing the size of the injected bubbles. As compared to the standard gas injection via large nozzles as used in practice, the liquid (water) production was remarkably higher when generating smaller bubbles via a porous plate inlet. An important effect of the reduced bubble size was the larger critical

*See also: S. Guet, G. Ooms, R.V.A. Oliemans, & R.F. Mudde. Accepted for publication in *Chemical Engineering Science.*

void fraction associated with the bubbly to slug flow transition boundary, as reported in the previous chapter. The improvements due to a reduced bubble size when operating in the bubbly flow regime were attributed to two essential effects: (a) the void fraction radial distribution changes from core peaking to wall peaking with decreasing bubble size, and (b) the slip velocity reduces with decreasing bubble size.

To predict the efficiency of gas-lift systems, the drift-flux model as proposed by Zuber and Findlay (1965) is commonly used. The main advantage of such an approach is the possibility of taking into account the above-mentioned effects in a simplified, one-dimensional model. This approach is furthermore applicable to a large range of flow regimes (bubbly flow, slug flow, churn-turbulent) provided that accurate models for the drift-flux parameters are available. It is therefore of importance for the application to investigate the effect of various conditions, such as the fluid properties, bubble and pipe dimensions, as well as the flow conditions, on the distribution parameter C_0 and void fraction weighted mean drift velocity $|U_{drift}|$.

The bubble size influences significantly the evolution of the radial distribution of void fraction in upward vertical bubbly pipe flows (Serizawa *et al.*, 1975; Liu, 1993a; Moursali *et al.*, 1995). Due to the lift force small bubbles move towards the pipe wall to generate the wall-peaking profile, whereas large bubbles (typically $D_b > 5 - 6mm$ in water) move toward the centre of the pipe. This is related to the interactions between the wake of the bubbles and the velocity distribution of the liquid (Tomiyama *et al.*, 2002b; Lucas *et al.*, 2001). As initially pointed out by Zuber and Findlay (1965), at wall-peaking void fraction conditions the distribution parameter is expected to be below 1 while for a parabolic (or 'core peaking') void fraction profile $C_0 > 1$. The C_0 distribution parameter should therefore be given as a function of bubble size in vertical pipe flows. Indeed, Hibiki and Ishii (2002) successfully applied such a bubble size dependent distribution parameter model for finely dispersed bubbly flow in small diameter pipes.

The liquid input can also influence the drift-flux parameters in vertical pipes. For instance low liquid input bubbly pipe flows can present liquid re-circulation patterns, similarly to bubble column flows. This 'convected bubble column' flow mode was measured by Mudde and Saito (2001) in a $15cm$ diameter column operating both in bubble column and low-liquid input flow mode conditions. Important changes of the drift-flux distribution parameter would therefore be expected at low liquid input flow conditions (Clark *et al.*, 1990). Hibiki and Ishii (2003) showed with global measurements in large vertical pipes ($10cm < D_p < 15cm$), that the distribution parameter was indeed strongly affected. As pointed out by Hibiki and Ishii (2003), the use of global measurements to extract distribution parameter information was mandatory due to the lack of local measurements for such low input and large diameter vertical pipe flow conditions. In those non-finely dispersed bubbly pipe flow conditions, the bubble size can be considered as an independent parameter, i.e. it can be varied by changing the bubble inlet configuration (see section 4.2 and figure 4.1). The bubble size cannot be determined from the global flow conditions, and needs to be determined from local measurements. The effect of bubble size on the distribution parameter in low liquid input, large diameter pipes remains therefore an open question.

The objective of this chapter is to investigate the effect of the bubble size on the drift-flux parameters for an upward vertical pipe flow operating at low to moderate liquid input conditions, and when approaching the transition from bubbly to slug flow. We used an $18m$ height vertical pipe with a realistic gas-lift condition pipe diameter of $72mm$, and the void fraction ranged up to $< \epsilon > = 0.3$. The gas was air and the liquid was a mixture of water and ethanol. We used two different injectors to investigate the effect of bubble size. To measure the radial distributions of void fraction, bubble size and velocity, we applied single and four-point optical fibre probes. For determining the time average liquid velocity (including its sign) we used a Laser Doppler Anemometer equipped with a pre-shifting Bragg-cell. For the direct measurement of the drift-flux parameters, simultaneous measurements of local void fraction, gas and liquid velocity were carried out at a height $h = 5m$ on our experimental set-up.

In section 5.2, we will investigate with synthetic void fraction profiles the sensitivity of the drift-flux parameters on the bubble size and liquid input. The experimental set-up and measurement techniques will be the subject of Section 5.3. Section 5.3.2 will be devoted to the drift-flux parameter measurements. We will then propose a model for taking into account the effect of liquid input and bubble size on the drift-flux parameters. The model results will be compared with pressure data obtained during separate measurements on our pipe flow experimental set-up in section 5.3.3.

5.2 Drift-flux parameters

5.2.1 Distribution parameter C_0

The bubble size has a strong effect on the transverse void fraction distribution. For small (typically $D_b < 5 - 6mm$) air bubbles in low to moderate diameter vertical pipes, the radial gas fraction distribution is known to present a peak near the wall (Serizawa *et al.*, 1975; Liu, 1993a). Larger bubbles lead to a parabolic type of profile. These effects of the void fraction profile on the distribution parameter C_0 were inferred by Clark *et al.* (1990). The authors applied a stress balance to compute the liquid velocity. With a parabolic void fraction distribution in a $10cm$ diameter air-water column, the distribution parameter could reach values of up to $C_0 = 5$, due to a liquid down-flow at the wall for low input conditions. With a saddle shape radial distribution of void fraction, the authors reported that the distribution parameter could be below unity in that case, since no returning liquid flow at the wall was observed.

These results suggest a significant change of the distribution parameter with a decreased bubble size at low liquid input conditions. However the numerical investigation reported in Clark *et al.* (1990) did not take into account the coupling effects between the void fraction and velocity profiles, and the bubble size effects on the stresses. Therefore, experimental evidence needs to be established on the minimum and maximum values taken by the distribution parameter C_0 by using experimental profiles of void fraction and velocities.

5.2.2 Void fraction weighted mean drift velocity

The drift velocity is defined as the slip velocity between the gas and the mixture

$$U_{drift} \equiv U_g - j, \tag{5.1}$$

which is related to the slip velocity between the gas and the liquid $U_{slip} = U_g - U_l$ in the following way:

$$U_{drift} = (1 - \epsilon)U_{slip}. \tag{5.2}$$

The weighted average mean drift velocity, as used in the drift-flux model, is given by $|U_{drift}| = \frac{<\epsilon U_{drift}>}{<\epsilon>}$. This average drift velocity is often taken as the rise velocity of a single bubble in an infinite medium, U_t. Although this might not have a significant effect on the result for high liquid input flows, since in that case $|U_{drift}| < U_t << j$, it is of importance to have a good description of this term for low liquid input flows, for which $j = O(U_t)$.

Both experimental and numerical investigations (Garnier *et al.*, 2002; Richardson and Zaki, 1954; Zenit *et al.*, 2001; Bunner and Tryggvason, 2002) outlined that the bubble slip velocity was decreasing with increasing void fraction. The slip velocity U_{slip} is generally correlated to the terminal velocity of a single bubble U_t and the local void fraction. Richardson and Zaki (1954) proposed for the drift velocity

$$U_{drift} = U_t(1 - \epsilon)^n, \tag{5.3}$$

where the exponent n has a typical value of 1 to 2.4 connected to the bubble size and shape (Van Wijngaarden, 1991). Based on a similar expression using the mean void fraction, Hibiki and Ishii (2002) proposed the following expression for the weighted mean drift velocity:

$$|U_{drift}| = U_t(1 - <\epsilon>)^{1.75}. \tag{5.4}$$

Garnier *et al.* (2002) found, from local measurements of bubble and liquid velocity in a well-controlled bubbly flow situation (and where no transverse gradient was occurring), that the slip velocity was scaling with the distance between bubbles. An expression for the slip velocity was proposed:

$$U_{slip} = U_t(1 - \epsilon^{\frac{1}{3}}). \tag{5.5}$$

By assuming that this expression is valid locally, i.e. by using the local value of ϵ in this expression, the local drift velocity follows from equation (5.2) as $U_{drift} = U_t(1 - \epsilon)(1 - \epsilon^{\frac{1}{3}})$.

We investigated the sensitivity of the weighted mean drift velocity to the void fraction radial profile by using prescribed wall and core peaking void fraction radial profiles. For the core peaking profile we use a parabola, and for the wall peaking profile we impose the peak at $0.8 < \frac{r}{R} < 0.9$ with a peak value of 20 % above the centerline value. The wall peaking void fraction profile was decreasing linearly from $\frac{r}{R} = 0.9$ to $\frac{r}{R} = 1$. These synthetic profiles are plotted in figure 5.1.

To investigate the void fraction radial profile influence on the drift flux parameters, we compute the weighted mean drift velocity

$$|U_{drift}| \equiv \frac{\int \epsilon(r)U_{drift}(r)rdr}{\int \epsilon(r)rdr}, \tag{5.6}$$

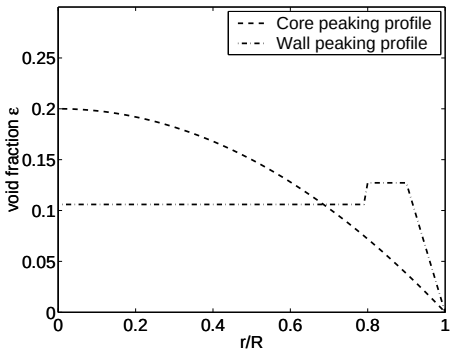

Figure 5.1: Imposed core peaking and wall peaking void fraction profiles.

where the local void fraction $\epsilon(r)$ is taken from the imposed void fraction profiles and the local drift velocity $U_{drift}(r)$ is computed from the models proposed by Richardson and Zaki (1954) and Garnier *et al.* (2002) (equations 5.2, 5.3 and 5.5). We also compute the weighted mean drift velocity directly from the mean void fraction using equation (5.4) as proposed by Hibiki and Ishii (2002). In analogy with this approach, we investigate a modified version of equation (5.5) for the weighted mean drift velocity, using directly the mean void fraction $< \epsilon >$:

$$|U_{drift}| = U_t(1 - < \epsilon >)(1 - < \epsilon >^{\frac{1}{3}}). \tag{5.7}$$

The weighted mean drift velocity obtained from those profiles and by applying the slip velocity correlations described above are presented in figure 5.2. The coefficient used in the Richardson and Zaki (1954) correlation is $n = 1.75$, as used by Hibiki and Ishii (2002) in equation (5.4). As can be seen from figure 5.2 the use of different correlations for the slip velocity leads to large changes of the weighted mean drift velocity value. However, as can also be seen from this figure the radial profile of void fraction is not significantly affecting the weighted mean drift velocity. The correlations using the mean void fraction are leading to similar results. Provided the *local* drift velocity can be described from the *local* void fraction value, the analog correlation using the area average void fraction can be used to relate directly the weighted mean drift velocity to the mean void fraction value. This is of practical importance for the direct computation of the weighted mean drift velocity from global measurements.

Richardson and Zaki (1954) suggested the use of an upper limit value of $n = 2.4$ (for $Re_b > 500$, where Re_b is the particle or bubble Reynolds number). Such large exponent values ($n > 2$) were reported in a number of experimental investigations. Using $n > 2$ for the weighted mean drift velocity, as used in Zenit *et al.* (2001), the predictions are leading to low slip velocity values similar to the results obtained with the relation proposed by Garnier *et al.* (2002). We therefore expect this model to provide a low limit value for the weighted mean drift velocity.

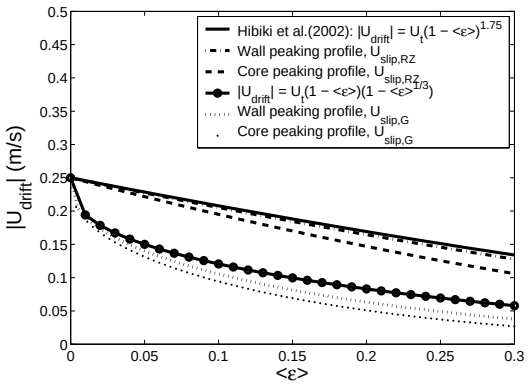

Figure 5.2: Weighted mean drift velocity versus area average void fraction. The slip velocity $U_{slip,RZ}$ refers to Richardson and Zaki (1954), $U_{slip,G}$ refers to Garnier *et al.* (2002). The void fraction trend is taken from figure 5.1. The model suggested by Hibiki and Ishii (2002) is also plotted.

5.3 Experiments

The experimental facility used for the drift-flux parameters bubbly pipe flow measurement corresponds to the convected bubbly flow conditions by making use of the centrifugal pump (section 3.1). As mentioned in the introduction, the bubble injector as used in practice consists of a large nozzle (gas-lift valve). To compare the effect of the size of the injected bubbles, we used the annular porous (1) and the large nozzle injector (3) (see section 3.1.3). During the application of gas-lift, the liquid properties are typically corresponding to low surface tension (section 2.3). It is therefore of interest to investigate the effect of a decreased liquid surface tension with respect to water. Two different liquid phases were used during the drift-flux parameter measurements. We reduced the liquid surface tension by mixing ethanol in water (Table 1). Although the surface tension was only reduced slightly with respect to water in case of liquid A, this had a significant influence on the bubble size generated from the porous plate, due to a modified bubble formation process (Koide *et al.*, 1968).

Liquid	Volumetric composition	$\rho_l(kg.m^{-3})$	$\mu(mPa.s)$	$\sigma(mN.m^{-1})$
A	water + 0.5% Ethanol	998.3	1.01	69.8
B	water + 2% Ethanol	998.2	1.01	59.3

Table 1: Liquids used for the drift-flux parameter determination experiments.

5.3.1 Local measurements of void fraction and phase velocities

5.3.1.1 Void fraction

We used an optical fibre for the local void fraction determination. We measured the local void fraction at $h = 5m$ with the central fibre of the four-point optical fibre (described in 5.3.1) and at $h = 6m$ with a single-point optical fibre probe on our pipe flow. The average void fraction followed from: $< \epsilon > = \frac{2}{R^2} \int \epsilon(r) r dr$.

The area-average values were compared with the volume average value obtained by differential pressure measurements, from $h = 4m$ to $h = 6m$. In the range of low liquid flow conditions of our experiments the contribution of friction and acceleration to the pressure drop is negligible. Since $< \epsilon > \rho_g << (1 - < \epsilon >)\rho_l$, the average void fraction was estimated from

$$< \epsilon > = 1 - \frac{\Delta P}{\Delta h \rho_l g}, \tag{5.8}$$

where ΔP is the pressure difference between two measurement points and Δh the distance between these points. We compared the mean void fraction results obtained from the optical fibre technique, applied at $h = 5m$, with the differential pressure drop measurements (figure 5.3). A reasonable agreement was obtained.

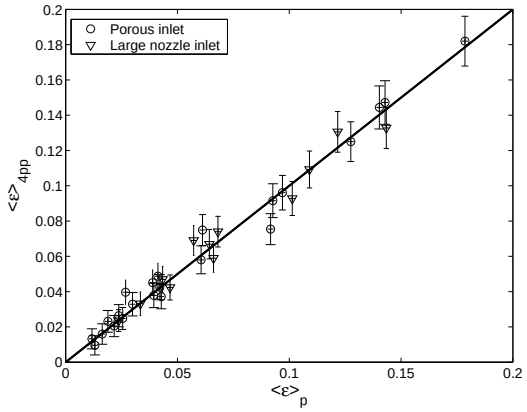

Figure 5.3: Comparison between the area averaged void fraction as obtained by the four-point probe measurements and by global measurements.

5.3.1.2 Bubble velocity

We measured the vertical component of the bubble velocity U_b by using a four point optical fibre probe (section 3.4). To relate the measured vertical chord length D_{bv} to the spherical equivalent diameter D_b, we used the following correlation for each individually measured bubble vertical chord length by the four-point optical fibre probe (Wellek *et al.*, 1966; Clift *et al.*, 1978; Tomiyama *et al.*, 2002b):

$$\chi = 1 + 0.163{E_o}^{0.757}, \tag{5.9}$$

where $\chi = \frac{D_{bh}}{D_{bv}}$ is the ellipsoidal shape-bubble aspect ratio and $E_o = \frac{g\rho_l {D_b}^2}{\sigma}$ is the Eötvös number. We used an iterative procedure to obtain the spherical equivalent diameter from equation (5.9), and using $D_b = D_{bv}\chi^{\frac{2}{3}}$.

We stored the four optical fibre signals on a computer with a NI-DAQ AI-16E-4 sampling card at a sampling frequency of $f = 65kHz$ per channel, and we analysed the sampled data separately. Each local four-point probe measurement contained a minimum of 500 selected bubbles according to the criteria $\beta = 0.25$ in equation (3.4). This corresponds to measurement time durations of 600 to $900s$ for each radial position. In figure 5.4 the superficial gas velocity obtained by area-integrating the four point probe measurements $U_{sg,4pp}$ (i.e. averaging the local gas flux obtained with void fraction and bubble velocity measurements), is compared with the superficial gas velocity as obtained with the gas flow meter $U_{sg,fm}$, confirming the accuracy of the measurements.

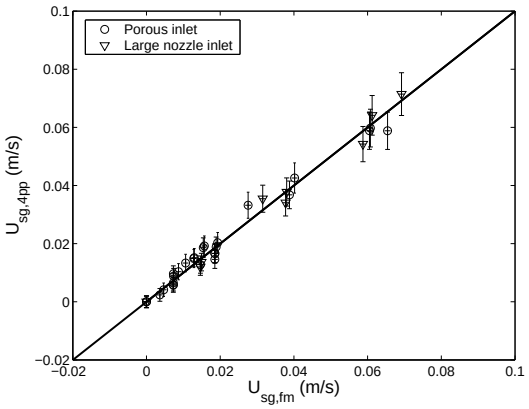

Figure 5.4: Comparison between the gas superficial velocity obtained by the four-point probe measurements and by global measurements. The bisector is also shown.

5.3.1.3 Liquid velocity

As mentioned in the introduction, the local liquid velocity in low liquid input bubbly pipe flows is expected to change sign, since a down flow at the wall can be present. Therefore, the flow direction cannot be prescribed a priori. This would make the application of Hot Film Anemometry (HFA) to such flows difficult: such a measurement technique, based on the heat transfer due to forced thermal convection between the flow and the heated film, provides the normal to the film component of velocity. As a result, only the absolute value of the liquid velocity can be obtained by using HFA. The application of HFA therefore requires preferential direction flows. Other particularities of HFA applied to low liquid input bubbly flows are: (a) the large inaccuracy associated with the low amplitude velocities, and (b) the difficulty of phase discrimination, requiring the application of careful signal thresholding (Farrar *et al.*, 1995; Ellingsen *et al.*, 1997; Larue de Tournemine *et al.*, 2001). The liquid velocity was measured by using a laser-Doppler anemometer (LDA), equipped with a pre-shifting Bragg-Cell to allow the measurement of reversal flow component. The present LDA technique was shown to give meaningful liquid velocity results in bubbly flow, provided the bubble size was large compared to the measurement volume dimensions, and the optical distance between the sending and receiving optics was low enough for enabling optical access (see section 3.3).

For each point, the measurement contained $360k$ values, corresponding to data series of $300s$ to $900s$. Due to the particularities of LDA applied to bubbly flow mixtures, i.e. the restricted optical access, the data rate was larger when measuring at the near wall region than when measuring at the centreline, and was decreasing with increased void fraction, as reported in section 3.3. Similar results are reported in Mudde *et al.* (1997) and Groen *et al.* (1999). The mean data rate was ranging from $1.5kHz$ to $50Hz$, depending on the void fraction, the velocity, and the measurement volume radial position. To investigate the possibility of multiple bubble scattering detection, measurements were carried out in bubbly flow without scattering particles. The data rate corresponding to no scattering particles was always below 5% of the data rate when measuring with scattering particles. This is a good confirmation that multiple bubble scattering was negligible during our experiments.

The time-average local velocity data were also compared with results obtained by applying the time-between data weighting correction procedure (see section 3.3). We did not find significant deviations between the two methods. The superficial liquid velocity could be obtained by area integration of the local liquid fluxes $j_l = (1-\epsilon)U_l$, where U_l is the liquid velocity as measured with the LDA and ϵ is the void fraction as measured with the optical fibre probe. We compared these results with the superficial liquid velocity as measured with the liquid flow meter: the agreement was reasonable (figure 5.5). The main sources of inaccuracy were connected to the near-wall void fraction determination at low liquid input, where we observed some bubbles travelling downward. Only the measurements providing the drift-flux parameter with confidence were used for further analysis.

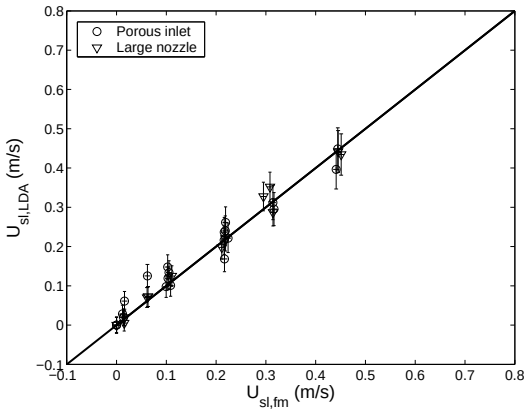

Figure 5.5: Comparison between the liquid superficial velocity obtained by the LDA measurements and by global measurements. The bisector is also shown.

For the direct computation of the drift-flux parameters in a section, we placed the LDA measurement volume $5mm$ below the central tip of the four-point probe by using the same measurement section as used for the four-point probe tests described in section 3.4.5.4 (figure 3.32). This measurement section was placed at a height $h = 5m$ on our upward bubbly pipe flow experimental set-up. We measured the pressure up- and downstream of the measurement section, at $h = 4m$ and $h = 6m$, for a comparison of the drift flux parameter results with global parameter measurements.

5.3.2 Results

5.3.2.1 Radial profiles

Void fraction

The transverse profiles were measured for a set of 40 experimental conditions, corresponding to $2mm < D_b < 15mm$, $0 < \epsilon < 0.3$ and $1000 < Re_m < 30000$, where $Re_m = \frac{U_m D_p \rho_l}{\mu_l}$ is the mixture Reynolds number. The use of the two different bubble injectors resulted in significant changes of the void fraction profiles (figure 5.6 compared to figure 5.7). The transition was essentially triggered by the bubble size: bubbles of less than $5mm$ equivalent diameter were accumulating at the wall, while bubbles of spherical equivalent diameter larger than $6mm$ were migrating to the centreline zone.

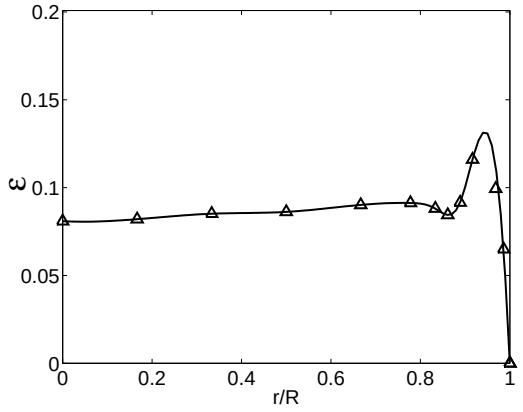

Figure 5.6: Void fraction profile for the porous inlet: $D_b = 4mm$ and $Re_{sl} = 16000$.

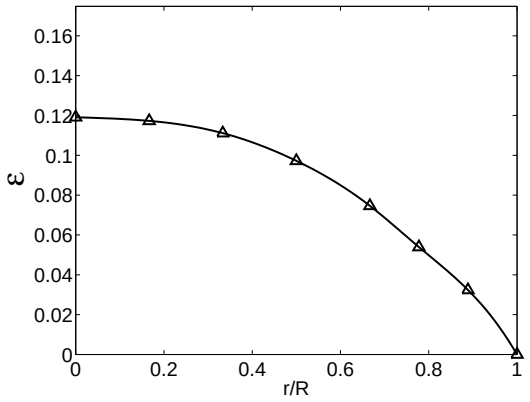

Figure 5.7: Void fraction profile, large nozzle inlet: $D_b = 8mm$ and $Re_{sl} = 16000$.

Phase velocities

Also the measured velocities were different (figure 5.8 and 5.9). The liquid velocity was evolving from a flat profile for small bubbles to a parabolic trend for larger bubbles. For low liquid input conditions, a returning liquid flow region at the wall could be observed. This is illustrated in figure 5.10 for $Re_{sl} = 1200$. This effect, already observed by Mudde and Saito (2001) in a $15cm$ diameter pipe, was also affected by the size of the bubbles and the void fraction conditions. The liquid down flow re-circulation increases with the mean void fraction, and is larger for large bubbles than for small bubbles (figure 5.10), as inferred in section 5.2. When

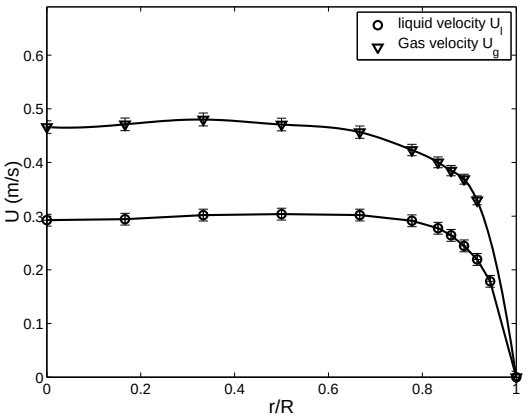

Figure 5.8: Gas and liquid velocity profile corresponding to the porous inlet void fraction profile experiment of figure 5.6.

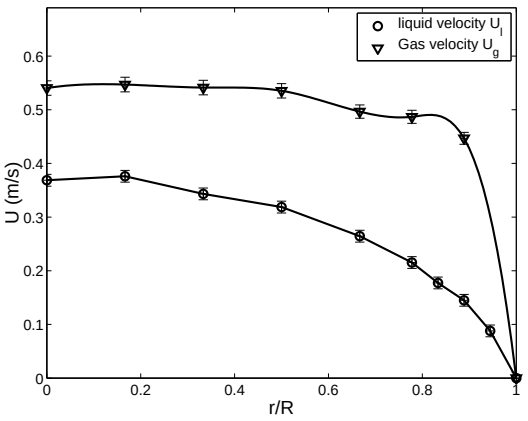

Figure 5.9: Gas and liquid velocity profiles corresponding to the large nozzle inlet void fraction profile experiment of figure 5.7.

injecting small bubbles and at low void fraction, both the magnitude and the area of the negative velocity region are lower than when increasing the void fraction and bubble size.

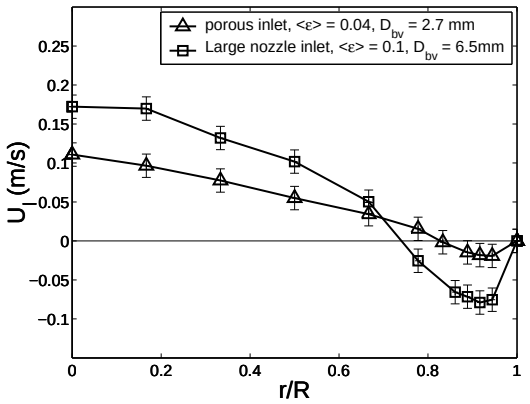

Figure 5.10: Returning flow at the wall for $Re_{sl} = 1200$ and for two bubble size and void fraction conditions.

5.3.2.2 Local slip velocity

The slip velocity between the gas and the liquid was larger at the wall for a core peaking profile, and reduced at the wall for a wall peaking profile (figure 5.9 compared to figure 5.8). This was essentially due to the bubble hydrodynamic interactions: the slip velocity is known to decrease for increased void fraction (Garnier *et al.*, 2002; Richardson and Zaki, 1954; Bunner and Tryggvason, 2002; Zenit *et al.*, 2001). This results in a local decrease of the slip velocity at the void fraction peak location (figure 5.6 and 5.8).

We investigated the effect of the local void fraction on the measured local slip velocity. The results, using our local measurements of void fraction and velocities, are shown in figure 5.11. For $D_b < 6mm$, the minimum value taken by the slip velocity was properly described by using the expression proposed by Garnier *et al.* (2002) (equation 5.5): $U_{slip} = U_t(1 - \epsilon^{1/3})$. The associated terminal velocity U_t was in the range of $0.2m/s < U_t < 0.26m/s$ for liquid A and $0.18m/s < U_t < 0.23m/s$ for liquid B. These values are in agreement with known results for the rise velocity of a single bubble in contaminated water (Clift *et al.*, 1978). The difference of terminal velocity between bubbles in liquid A and B is due to the surface tension property changes: in that range of bubble size, the terminal velocity U_t of a single bubble is given by (Peebles and Garber, 1953): $U_t = 1.53\left(\frac{g\sigma}{\rho_l}\right)^{\frac{1}{4}}$. Therefore, the changes of terminal velocities for liquid A and B are related by $U_{t,B} = U_{t,A}\left(\frac{\sigma_B}{\sigma_A}\right)^{\frac{1}{4}}$. This leads to a ratio of 0.96, which is consistent with the terminal velocity values as obtained from the measurements.

The terminal velocity of a single bubble increases with the bubble size (Clift *et al.*, 1978; Peebles and Garber, 1953). We clearly observed this effect in our experiments (figure 5.11): for $D_b > 6mm$, the slip velocity values were in general larger than for the smaller bubbles. This is due to an increase of the bubble terminal velocity with bubble size for that range of bubble diameter in contaminated water (Clift *et al.*, 1978), associated with a progressive change of bubble shape regime with increasing bubble size.

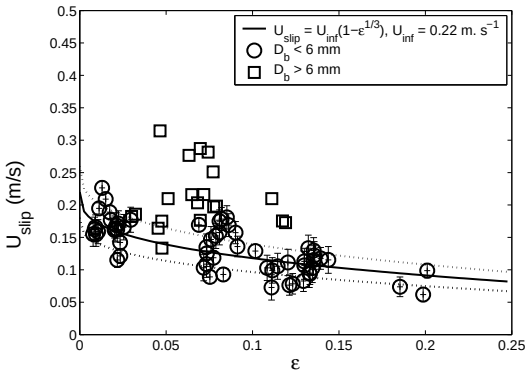

Figure 5.11: Local slip velocity versus local void fraction for two bubble size classes. The solid line denotes Garnier *et al.* (2002) relation for the slip velocity.

5.3.2.3 Weighted mean drift velocity

The weighted mean drift velocity was computed from the measured local velocities and void fractions and by applying the formal definition given by equation (5.6). The results are shown in figure 5.12 for three different bubble size classes. As shown in figure 5.11, the measured local slip velocities were found to be in good agreement with the relation proposed by Garnier *et al.* (2002) when using the measured local void fraction ϵ. We therefore compared the measured weighted mean drift velocity with an analog formulation using the area average value of the void fraction (equation 5.7). The measurement results were also compared with the correlation proposed by Hibiki and Ishii (2002) (equation 5.4) in figure 5.12.

The weighted mean drift velocity associated with small bubbles ($D_b < 6mm$) was properly described by equation (5.7). For intermediate size-range bubbles, corresponding to the wobbling regime ($6mm < D_b < 12mm$), the measured weighted mean drift velocity values were more difficult to predict, although the weighted mean drift velocity values were ranging between equation (5.7) and the relation proposed by Hibiki and Ishii (2002). For large bubbles ($D_b > 12mm$), we did not measure a clear dependence of the weighted mean drift velocity on the area average void fraction. For those large bubbles, the values were ranging from $|U_{drift}| = 0.23m.s^{-1}$ to $|U_{drift}| \approx 0.3m.s^{-1}$ (figure 5.12). The maximum value of $0.3m.s^{-1}$ corresponds to the transition to slug flow: this is consistent with a commonly used slug flow

correlation (Clift *et al.*, 1978; Mishima and Ishii, 1984; Hibiki and Ishii, 2002): $|U_{drift}| = 0.35(gD_p)^{\frac{1}{2}} \approx 0.3m.s^{-1}$.

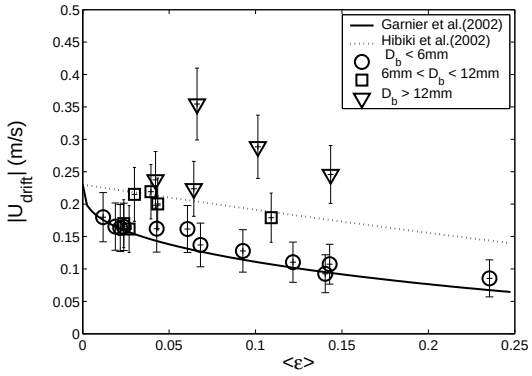

Figure 5.12: Weighted averaged mean drift velocity, obtained from the local measurements of void fraction and phases velocities. For $D_b < 6mm$, the drift velocity is correctly predicted using equation (5.7).

5.3.2.4 Distribution parameter C_0

We computed the distribution parameter C_0 for each profile by applying the formal definition to cylindrical coordinate averaging

$$C_0 \equiv \frac{<\epsilon j>}{<\epsilon><j>} = \frac{R^2}{2}\frac{\int \epsilon j r dr}{\int \epsilon r dr \int j r dr}, \tag{5.10}$$

in which ϵ is the *local* void fraction, $j = \epsilon U_g + (1-\epsilon)U_l$ is the (local) mixture volumetric flux and R is the pipe radius. In figure 5.13, we present the distribution parameters obtained from all the measurements as a function of the mixture Reynolds number Re_m. It is clear from that picture, that both the bubble size and the input flow conditions are having an important impact on the distribution parameter C_0.

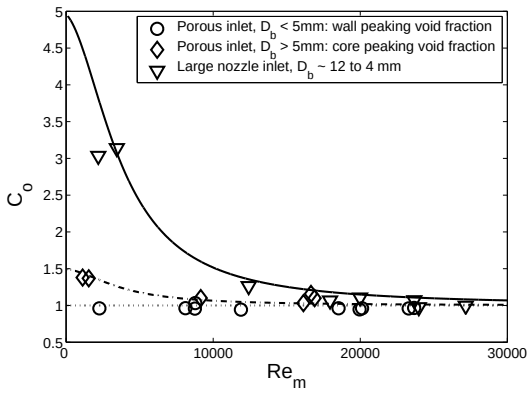

Figure 5.13: Distribution parameter C_0 versus mixture Reynolds number Re_m for all the experiments. The dotted line represents $C_0 = 1$. The solid line denotes the upper C_0 limit for the large nozzle inlet by using equation (5.13) with $C_{BC} = 5$, $C_{0,Re\infty} = 1.2$ and $Re_c = 4000$. The dash-dotted line corresponds to the upper limit obtained at core peaking void fraction profile for the porous inlet ($C_{BC} = 1.5$).

Bubble size

Wall peaking void fraction profiles, associated with the porous bubble inlet, could lead to values as low as $C_0 = 0.95$. This value could be maintained even for low liquid input conditions, provided that the bubble size was small enough to ensure a wall peaking void fraction profile and that no returning liquid flow was occurring at the wall. When using the large nozzle inlet, the C_0 values were systematically larger, with a typical value of $C_0 = 1.2$ at large liquid input conditions (figure 5.13).

Provided that liquid re-circulation was not occurring, the C_0 parameter was only connected to the bubble size, and was increasing from 0.95 to 1.2 with bubble diameter. This is clear from figure 5.14, where all the C_0 parameter results corresponding to $Re_m > 20000$ are plotted as a function of the spherical equivalent bubble diameter measured with the four-point optical fibre probe. Our measured C_0 parameters are compared with the bubble size dependent relation proposed by Hibiki and Ishii (2002):

$$C_0 = \left(1.2 - 0.2\frac{\rho_g}{\rho_l}\right)\left(1 - e^{-22\frac{D_s}{D_p}}\right), \tag{5.11}$$

where D_s is a Sauter mean bubble diameter, equal to the spherical equivalent bubble diameter for monodisperse bubble sizes. This correlation was obtained by Hibiki and Ishii (2002) by interpolating the measured C_0 parameter with the estimated bubble diameter in pipes of small diameter.

Equation (5.11) was correctly describing the trend associated with the wall to core peaking of void fraction profile, although the critical values of the bubble diameter corresponding to the changes of the C_0 parameter were differing. These changes are attributed to the smaller pipe diameters studied by Hibiki and Ishii (2002), the different bubble diameter determination techniques, as well as the different liquid

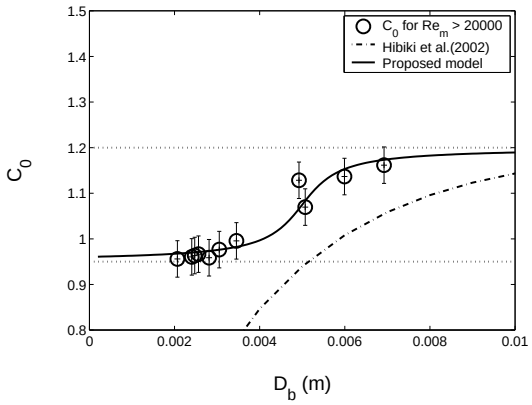

Figure 5.14: Distribution parameter C_0 versus the spherical equivalent bubble diameter D_b. Also the correlation proposed by Hibiki and Ishii (2002) for finely dispersed bubbly flow in small diameter pipes is plotted.

properties. However, the transition from a wall peaking void fraction profile to core peaking, responsible for the changes of C_0 values, were clearly associated with a critical value of the bubble size. Provided no down-flow of liquid at the wall was occurring, the C_0 parameter was typically ranging from $C_0 = 0.95$ at wall peaking profile, to $C_0 \approx 1.05 - 1.1$ at the transition and $C_0 = 1.2$ at the core peak void fraction conditions (figure 5.14). We therefore suggest the use of the correlation

$$C_0 = C_{0,crit} + (\frac{2}{\pi})(C_{0,crit} - C_{0,min})tan^{-1}[A(D_b - D_{b,crit})], \qquad (5.12)$$

where $C_{0,crit}$ and D_{bcrit} are the distribution parameter and bubble diameter associated with the transition from wall peaking to core peaking ($C_{0,crit} = \frac{C_{Max}+C_{min}}{2} = 1.075$ and $D_{b,crit} = 5mm$ at $Re_m > 20000$). $C_{0,min} = 0.95$ is the minimum value of the C_0 parameter and A is an adjustable coefficient. We could correctly describe the effect of bubble size on the distribution parameter by using equation (5.12) with $A = 1500m^{-1}$ (figure 5.14).

An important difference with the correlation proposed by Hibiki and Ishii (2002) is the existence of a lower limit $C_{0,min}$: the C_0 parameter was not decreasing to lower values than $C_0 = 0.95$, even for very small bubbles. This lower limit is due to the particularities of the wall peaking void fraction profile: the void fraction and the phase fluxes are decreasing to a zero value at the wall. The void fraction peak is thus located at some distance from the wall (of the order of the bubble diameter). The measured C_0 parameter values are therefore larger then when analytically applying a void fraction peak at the wall location and a zero void fraction at the centreline, as initially suggested by Zuber and Findlay (1965).

Liquid input

At large liquid input (i.e. on the right part of figure 5.13), the bubble size was significantly reduced when using the large nozzle inlet, due to the occurrence of bubble break-up in the vicinity of the injector. This resulted in a flatter void fraction profile. This is illustrated in figure 5.15, where the measured bubble diameters are plotted as a function of the mixture Reynolds number: for $Re_m > 20000$, the maximum bubble size is decreasing.

The gas injector configuration also affects the distribution parameter values at low input conditions. For large bubbles, the magnitude of the (negative) peak of returning flow in the near wall region was larger than for the smaller bubble experiments. This resulted in an increased distribution parameter with larger bubbles. It is interesting to compare the actual results with the existing literature on low liquid input bubbly flows (Collins *et al.*, 1978; Clark *et al.*, 1990). For the slug flow regime, Collins *et al.* (1978) and Dukler and Fabre (1994) suggested to replace the well known large liquid input slug flow value of $C_0 = 1.2$ by

$$C_0 = \frac{C_{BC}}{1 + \left(\frac{Re_m}{Re_c}\right)^2} + \frac{C_{0,Re_\infty}}{1 + \left(\frac{Re_c}{Re_m}\right)^2}, \tag{5.13}$$

where Re_c is a critical Reynolds number, $C_{0,Re_\infty} = 1.2$ is the large-input slug flow distribution parameter and C_{BC} corresponds to the distribution parameter associated with zero-liquid input slug flow, i.e. bubble column flow mode. Collins *et al.* (1978) proposed $C_{BC} = 2.27$ for the bubble column flow mode distribution parameter. During our experiments, the C_0 dependency on Re_m could be described by using equation (5.13). The upper limit of the C_0 experimental data was fitted by using $Re_c = 4000$ and changing the value of C_{BC} in equation (5.13), from $C_{BC} = 1.5$ for the core peaking porous inlet to $C_{BC} = 5$ for the large bubble inlet (figure 5.13).

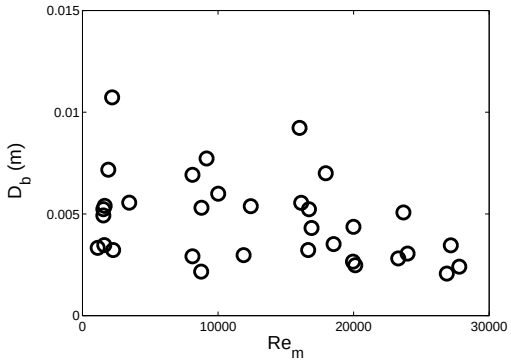

Figure 5.15: Spherical equivalent bubble diameter D_b as a function of the mixture Reynolds number Re_m. For $Re_m > 20000$, the maximum bubble size is decreasing with the liquid input, due to turbulence break-up in the vicinity of the large nozzle inlet.

5.3.3 Drift-flux model predictions

In this section, the relations obtained for $|U_{drift}|$ and C_0 (equation 5.7, 5.12 and 5.13) are tested and validated by using pressure data collected on our pipe flow experimental set-up during separate experiments. We tested three liquid flow rates conditions, corresponding to $Re_{sl} = 1200; 8000$ and 16000. During each fixed liquid input condition experiment, we increased the gas flow rate stepwise to generate a set of experimental results. We also used a third porous gas injector to ensure very small diameter bubbles ($D_b = 0.1$ to $5mm$). This injector consisted of a mixing box, in which a large area of low pore size material was used to generate the bubbles. This mixing box is sketched in figure 3.3, and was described in more details in section 3.1. This ensured smaller bubbles compared to the previous porous inlet (Koide *et al.*, 1968). The bubble size being reduced, this injector can be expected to postpone the wall to core peaking transition to larger values of the gas input. We estimated the area average void fraction $< \epsilon >$ at $h = 5m$ from the pressure data collected at $h = 4m$ and $6m$ and using $< \epsilon > = 1 - \frac{\Delta P}{\Delta h \rho_l g}$, i.e. neglecting the pressure drop due to friction.

During those separate experiments, we did not measure any local quantities, and we estimated the bubble size from photos. From these estimates, we obtained three bubble size conditions:

- Very small bubbles, corresponding to $D_b \approx 0.1$ to $5mm$, generated by the above mentioned new porous injector,
- Intermediate size range bubbles: $4mm < D_b < 10mm$, generated by the porous injector used previously. With an increased bubble size, the transition from a wall peaking to a core peaking radial profile of void fraction was observed.
- Large bubbles, associated with the large nozzle inlet ($D_b \approx 10mm$).

5.3.3.1 Drift flux modelling

We used the drift-flux model, given by equation (2.8), in the form of

$$< \epsilon > = \frac{U_{sg}}{C_0 < j > + |U_{drift}|}, \tag{5.14}$$

in which U_{sg} and $< j >$ were given by the experiment. We used the models proposed in section 5.3.2.3 and 5.3.2.4 for the drift-flux parameters $|U_{drift}|$ and C_0 respectively. We considered two situations, corresponding to: (a)the small bubble, wall peaking profile and (b) the slug flow regime, known to have a detrimental effect on the area average void fraction for given input flow conditions. Both C_0 and $|U_{drift}|$ are decreasing with bubble size and are the largest at slug flow conditions. It can be expected that plotting (a) and (b) will give an upper and lower limit for the collected experimental data of area average void fraction at given flow conditions.

We computed the trends predicting case (a) and case (b) from equation (5.7), (5.12), (5.13) and (5.14):

a - Small bubbles, wall peaking void fraction profile ($D_b < 5mm$):
$C_0 = 0.95$ and $< U_{drift} > = (1 - < \epsilon >)(1 - < \epsilon >^{\frac{1}{3}})U_t$. In that case, we solved equation (5.14) iteratively due to the dependence of $|U_{drift}|$ on $< \epsilon >$.

b - The slug flow boundary, corresponding to the lowest $< \epsilon >$ values for given gas and liquid flow conditions. This boundary is given by $|U_{drift}| = 0.35(gD_p)^{\frac{1}{2}} = 0.3m.s^{-1}$ and C_0 is taken from equation (5.13). The constants were $C_{BC} = 5$ and $C_{0,Re\infty} = 1.2$, as obtained experimentally for the large nozzle inlet in section 5.3.2.4. Although Re_m changed slightly during each experiment since the gas input was varied, we neglected this effect ($Re_{sl} \approx Re_m$). The slug flow distribution parameter was therefore given a constant value for each experiment: $C_0 = 1.3; 1.5$ and 4 for $Re_{sl} = 16000$; 8000 and 1200 respectively.

5.3.3.2 Model results

We plotted the mean void fraction as a function of the superficial gas velocity for three bubble size experimental conditions, corresponding to: the wall peaking void fraction radial profile ($D_b < 5mm$), the intermediate to centreline peaking void fraction profile ($4 < D_b < 10mm$) and the large bubble core peaking case corresponding to the large nozzle inlet. The results are presented and compared with the predictions given by case (a) and (b) in figure 5.16, 5.17 and 5.18 for $Re_{sl} = 16000$, 8000 and 1200 respectively.

The large nozzle inlet void fraction data were closely described by the slug flow correlation results given by model (b), although no large slug bubbles were observed at the measurement location during those experiments. However, at low gas input, the large nozzle mean void fraction values were slightly larger than the slug flow values. This is due to lower bubble diameter at decreased gas input, resulting in a decreased weighted mean drift velocity $|U_{drift}|$.

We could describe closely the small bubbles data ($D_b < 5mm$) with the maximum void fraction value taken by case (a). At low gas input, the void fraction data were providing even larger void fraction results than predicted by model (a). This was due to the sub-millimetre size range of the bubbles for $U_{sg} < 0.01m.s^{-1}$, resulting in decreased bubble terminal velocity values (Peebles and Garber, 1953). The inter-

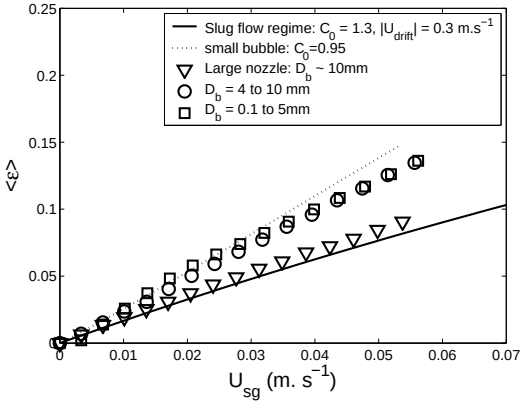

Figure 5.16: Mean void fraction versus superficial gas velocity for $Re_{sl} = 16000$.

mediate bubble size range void fraction values ($D_b > 4mm$) were contained between the small and the large bubble experiments. A gradual evolution from the small to the large bubble model can be observed, due to the increased bubble diameter with gas input, from $D_b = 4mm$ to $D_b = 10mm$.

At low liquid input conditions ($Re_{sl} = 1200$, figure 5.18), the wall peaking line described by model (a) was matching with the small bubble experiments only for very low void fraction conditions ($\epsilon < 0.03$). At increased void fraction, the returning flow effects on the C_0 value were enhanced. This is a good indication that the bubbles have the tendency to be ejected from the liquid down flow region, due to an inversed lift force in that area. Although the smaller bubbles reduced the magnitude of the liquid down-flow at the wall compared to larger bubbles, the C_0

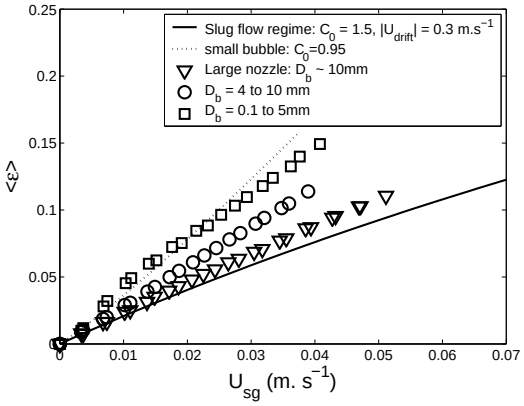

Figure 5.17: Mean void fraction versus superficial gas velocity for $Re_{sl} = 8000$.

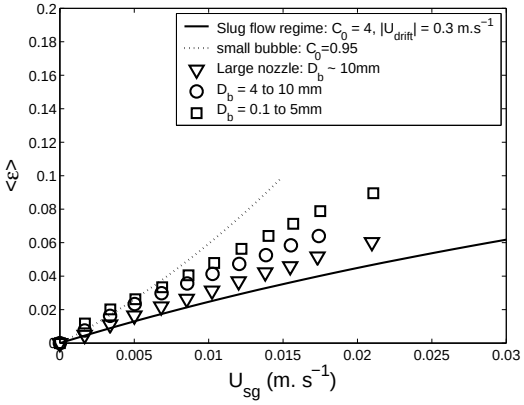

Figure 5.18: Mean void fraction versus superficial gas velocity for $Re_{sl} = 1200$.

parameter value was quickly above unity when increasing the void fraction in that case.

5.3.4 Conclusion

We investigated the sensitivity of the drift flux parameters to the bubble size at low input flow conditions in a vertical upward bubbly pipe flow of diameter $D_p = 72mm$ and height $H = 18m$. We monitored both the distribution parameter and the weighted mean drift velocity from measurements of the void fraction and phase velocity radial profiles at various bubble size and liquid input conditions. We used single and four-point optical glass fibre probes for the bubble fraction, velocity and size determination, and a Laser Doppler Anemometer for the local liquid velocity sign and magnitude. The weighted mean drift velocity and distribution parameter were strongly affected by the bubble size value.

We could describe the low-limit value of the weighted mean drift velocity associated with the small bubbles from the area average void fraction by using a modified version of the slip velocity expression proposed by Garnier *et al.* (2002) (equation (5.7)). The large bubbles mean drift velocity values were systematically larger but no unique correlation was found. The small bubbles ($D_b < 5 - 6mm$) were accumulating at the wall, resulting in a decreased distribution parameter. Also the liquid input was influencing the distribution parameter value. We found that the distribution parameter could reach values of up to $C_0 > 2$ for low-input flows with large bubbles, while for small bubble wall peaking void fraction profile flow conditions, we obtained a minimum plateau value of $C_0 = 0.95$.

We proposed a bubble size and input flow conditions dependent model for the drift flux parameters, that we tested for the description of the small bubble wall peaking void fraction profile and the slug flow regime. The model results were compared with pressure data collected during separate experiments on our experimental set-up at various liquid input conditions. Reasonable area average void fraction predictions were obtained. For a practical airlift application, the trends given by these two flow models can be used to quantify the optimal pressure gradient improvements gained by decreasing the bubble size.

As a following step, it would be interesting to investigate whether the experimental observation reported in this chapter could be described by using a bubble size dependent numerical model for predicting the void fraction and velocity radial profiles. Such a model would potentially permit to up-scale our drift-flux parameters results to different fluid and geometrical properties. This will be the subject of the next chapter.

Chapter 6

Bubbly pipe flow modelling*

Abstract

We developed a simplified Euler-Euler model for predicting the void fraction and velocity profiles in a vertical upward bubbly pipe flow. The main objective of this approach is to provide a tool for computing the gravitational pressure gradient associated with a large number of flow conditions. This model is based on existing correlations for the interfacial momentum transfer and for turbulence modelling. Assuming a fully developed, axially symmetric flow, our formulation reduces to a set of first order equations, which can be solved with relatively fast convergence. The results obtained with our approach are first validated by comparisons with experiments collected in small-diameter tubes, taken from literature. Then, the model results are compared with our experiments at low liquid input, moderate pipe diameter conditions and for various bubble size values. The model is found to correctly predict the evolution of void fraction and velocity profiles associated with bubble size and liquid input changes. We finally computed the drift-flux model distribution parameter and the superficial gas velocity for various flow conditions. The results show a reasonable comparison with experiments.

6.1 Introduction

Modelling the relevant physical phenomena for predicting the phase and velocity radial distributions in upward bubbly pipe flows is a challenging issue. The main difficulties are associated with the dependency of the void fraction radial profile on the bubble size and flow conditions, and the coupling between the void fraction and velocity profiles. To solve this problem, the two-fluid or Euler-Euler modelling approach (Ishii, 1975) is often applied for vertical upward bubbly pipe flow predictions (Drew and Lahey, 1982; Lopez de Bertodano, 1994; Hill *et al.*, 1995; Chahed and Masbernat, 1998; Lucas *et al.*, 2001; Politano et al., 2003). In this modelling method both the continuous phase and the dispersed phase are considered as a continuum. The mass and momentum conservation equations are averaged and given in Eulerian coordinates.

*See also: S. Guet, G. Ooms, & R.V.A. Oliemans. A simplified Euler-Euler model for gas-lift efficiency predictions. *Submitted for publication.*

The aim of the present contribution is to develop a simplified model able to predict the main effects of bubble size and liquid input on the gravitational pressure gradient in vertical upward bubbly pipe flows. We want to develop an Euler-Euler model able to capture the main changes in transverse profiles due to bubble size and liquid input, based on available models for the interfacial momentum transfer and turbulence modelling. Our objective is to develop a simple and fast converging model. Such a model will enable to investigate the effect of various combinations of bubble size and liquid input conditions on the gravitational pressure gradient.

The bubble size is known to affect the void fraction transverse profiles in vertical pipe flows. Small bubbles accumulate at the wall to form a wall peaking radial distribution, while large bubbles migrate to the centreline zone of the pipe and lead to a core-peaking void fraction distribution. Recently, it was shown that the evolution of the transverse void fraction profile with increased bubble size could be properly described by using an appropriate model for the lift force, as proposed in Tomiyama (1998) and Tomiyama *et al.* (2002b) (Lucas *et al.*, 2001; Politano et al., 2003). In this model, the lift force coefficient is changing sign with increased bubble diameter, due to the effects of bubble deformation on the bubble wake - shear field interactions. In addition, a lubrication type of repulsion force at the near wall, as suggested in Antal *et al.* (1991) brought significant improvements for proper near wall void fraction predictions.

Also the liquid input conditions have an impact on the transverse profiles of liquid velocity and void fraction. At low enough liquid input, a down flow of liquid at the wall can be observed, similarly to bubble column flows (Mudde *et al.*, 1997; Mudde and Saito, 2001). This in turn can be expected to affect the void fraction profile: the liquid velocity gradient is changing sign near the wall, which might result in an inversed lift force direction in that area. Therefore, at low liquid input conditions, not only the bubble size is important for the void fraction profile determination, but also the coupling effects between the liquid input and the bubble size.

The gas-lift technique is a gravity-driven pumping technique, which uses gas injection to reduce the gravitational pressure in vertical oil wells. The reduced pressure compared to single-phase liquid flow permits to generate or increase the liquid input. To quantify the gas-lift efficiency changes due to the effects of bubble size and liquid input, we will compute the distribution parameter C_0 of the drift-flux model (Zuber and Findlay, 1965) for various flow conditions. This parameter C_0 directly connects the area average void fraction to the superficial gas and liquid velocities by

$$\frac{U_{sg}}{<\epsilon>} = C_0(U_{sg} + U_{sl}) + |U_{drift}|, \tag{6.1}$$

in which $|U_{drift}|$ is the weighted mean drift velocity defined by

$$|U_{drift}| = \frac{\int_A \epsilon U_{drift} dA}{\int_A \epsilon dA}. \tag{6.2}$$

The distribution parameter C_0 is given by

$$C_0 = A\frac{\int_A \epsilon j dA}{\int_A \epsilon dA \int_A j dA}, \tag{6.3}$$

where j is the (local) mixture flux: $j = \epsilon U_g + (1-\epsilon)U_l$. It is clear from equation (6.1), that provided $|U_{drift}|$ is known the distribution parameter C_0 given by equation (6.3) can be used to quantify the gravitational pressure gradient for given gas and liquid superficial velocities U_{sg} and U_{sl}. Such a result permits to evaluate the gas-lift efficiency when operating at low liquid input, since in those conditions the frictional pressure drop is negligible regarding the gravitational contribution.

In a previous study, we measured the radial profiles of void fraction and phase velocities associated with various bubble size and liquid input conditions in a $72mm$ inner diameter pipe flow experimental set-up. The measurement techniques used for that purpose were a four-point optical fibre probe for the bubble velocity and size determination (Mudde and Saito, 2001), and Laser Doppler Anemometry for the liquid phase velocity characterization. Based on these measurements, we computed the distribution parameter C_0 by applying equation (6.3) to the measured profiles of void fraction and velocities. Due to the changes in the void fraction and velocity distributions, significant variations of the distribution parameter were found when varying the bubble size and the liquid input conditions, from $C_0 \approx 0.95$ for large liquid input flow with small bubbles to $C_0 > 1.2$ for low liquid input conditions with large bubbles.

The changes of the C_0 parameter will be investigated with a numerical model in the present study. The advantage of developing such a model is its potential ability to upscale our experimental results to different pipe diameter and fluid properties. We will first compare some computed void fraction and velocity profiles with experiments reported by Liu and Bankoff (1993b) and Serizawa *et al.* (1975) for pipe diameters $D_p = 38mm$ and $D_p = 60mm$ respectively. Then, our model results will be compared with our experimental data collected on a $72mm$ diameter pipe flow experimental set-up. Various liquid input and bubble size conditions will be compared. Finally, the distribution parameter C_0 of the drift-flux model will be computed for a large range of liquid input and bubble size conditions, and compared with our set of experimental data.

6.2 Model formulation

6.2.1 Averaged equations

The phase indicator functions X_k, where $k = g$ or l for the gas and the liquid phase, are introduced:

$$X_k(\vec{x},t) = \begin{cases} 1 & \text{if } \vec{x} \text{ is in phase k,} \\ 0 & \text{otherwise.} \end{cases}$$

The phase indicators X_k are advected by phase k :

$$\frac{\partial X_k}{\partial t} + \vec{u}_k.\vec{\nabla}(X_k) = 0, \tag{6.4}$$

and the averaged value of the phase indicator leads to the k-phase averaged fraction:

$$\epsilon_k = \langle\langle X_k \rangle\rangle \tag{6.5}$$

The velocity is decomposed into an average and a fluctuating part $\vec{u}_k = \vec{U}_k + \dot{\vec{u}_k}$, with $\vec{U}_k = \langle\langle \vec{u}_k \rangle\rangle$. After averaging the continuity and momentum conservation equation

for the gas and the liquid phases, the following set of four equations is obtained ($k = g$ or l):

$$\frac{\partial(\epsilon_k \rho_k)}{\partial t} + \vec{\nabla}.(\epsilon_k \rho_k \vec{U}_k) = 0. \tag{6.6}$$

$$\frac{\partial(\epsilon_k \rho_k \vec{U}_k)}{\partial t} + \vec{\nabla}.(\epsilon_k \rho_k \vec{U}_k \vec{U}_k{}^t) = \epsilon_k \rho_k \vec{g} + \epsilon_k \vec{\nabla}.(\boldsymbol{\tau}_{kT}) - \epsilon_k \vec{\nabla} P_k + \vec{M}_k + (\boldsymbol{\tau}_{kT} - \boldsymbol{\tau}_{kI})\vec{\nabla}\epsilon, \tag{6.7}$$

where ρ_k, U_k, P_k and ϵ_k are respectively the average density, velocity, pressure and the volume fraction of phase k. $\vec{M}_k$ is the interfacial momentum transfer, $\boldsymbol{\tau}_{kT}$ denotes the average total stress tensor, and $\boldsymbol{\tau}_{kI}$ is the average total stress tensor at the interface. The total stress is decomposed into a viscous shear and a turbulence part:

$$\boldsymbol{\tau}_{kT} = \boldsymbol{\tau}_k{}^{\mu} + \boldsymbol{\tau}_k{}^{Re} \tag{6.8}$$

where $\boldsymbol{\tau}_k{}^{\mu}$ is the viscous contribution and $\boldsymbol{\tau}_k{}^{Re}$ is the Reynolds stress tensor representing the contribution due to turbulence. In the present model, it is defined by $\epsilon_k \boldsymbol{\tau}_k{}^{Re} = -\langle\langle X_k \rho_k \dot{\vec{u}}_k \dot{\vec{u}}_k{}^t \rangle\rangle$.

6.3 Interfacial momentum transfer

The interfacial momentum transfer is decomposed into

$$\vec{M}_k = (P_{kI} - P_k)\vec{\nabla}\epsilon_k + \vec{F}_k, \tag{6.9}$$

where the first term on the right hand side denotes the interfacial pressure density. It takes into account the effect of the average interfacial pressure P_{kI}, different from the far field pressure P_k. The second term $\vec{F}_k$ represents all the other interfacial forces. The interfacial force $\vec{F}_k$ is expressed in the following way:

$$\vec{F}_k = \vec{F_{k,drag}} + \vec{F_{k,lift}} + \vec{F_{k,wall}} + \vec{F_{k,am}} + \vec{F_{k,td}}, \tag{6.10}$$

where $\vec{F_{drag}}$ is the drag force, $\vec{F_{lift}}$ the lift force, $\vec{F_{wall}}$ a wall force, $\vec{F_{am}}$ the added mass force, and $\vec{F_{td}}$ a turbulent dispersion force, which can be included in different ways. The gravity and drag forces are acting along the $\vec{g}$ vector (i.e. in the axial direction for vertical pipe flow). The lift, wall and turbulent dispersion forces are acting in the transverse direction. The competition between those three forces therefore has an important impact on the void fraction profile. In the present model, the added mass force contribution is neglected, and we consider a fully developed pipe flow. By considering no mass transfer between phases and neglecting surface tension forces, we will assume $\vec{F_g} = -\vec{F_l}$.

6.4 A simple two-fluid model for vertical bubbly pipe flow

6.4.1 Assumptions

A simple version of the two-fluid model is formulated. The assumptions are:

1 the flow is stationary ($\frac{\partial}{\partial t} = 0$),

2 we assume a 1D flow: $\vec{U_g}.\vec{e_r} = \vec{U_l}.\vec{e_r} = 0$ and $\vec{U_g}.\vec{e_\theta} = \vec{U_l}.\vec{e_\theta} = 0$, in which $\vec{e_r}$, $\vec{e_\theta}$ and $\vec{e_z}$ are the radial, tangential and axial direction,

3 the flow is fully developed ($\frac{\partial U_k}{\partial z} = 0$ and $\frac{\partial \epsilon_k}{\partial z} = 0$). Although bubbles will always expand and/or coalesce, far from the entrance boundaries this hypothesis is locally valid.

4 The relative velocity $U_r = |\vec{U_g} - \vec{U_l}|$ between the bubble and the liquid phase is constant in the radial direction.

5 In the gas phase, both the gravity and stress terms are neglected due to the low density and viscosity.

6 In the liquid phase, the difference between the average stress tensor and the interfacial stress tensor is neglected.

6.4.2 Closure formulation

6.4.2.1 Drag force

The drag force density is given by:

$$\vec{F_{g,drag}} = -\frac{3}{8}\frac{\epsilon}{R_b}C_d\rho_l(\vec{U_g} - \vec{U_l})|\vec{U_g} - \vec{U_l}|, \tag{6.11}$$

in which $\epsilon = \epsilon_g$ and where the drag coefficient is taken as (Politano et al., 2003):

$$C_d = \frac{8}{3}(1-\epsilon)^2. \tag{6.12}$$

6.4.2.2 Lift force

The general formulation of the lift force is:

$$\vec{F_{g,lift}} = -C_l\epsilon\rho_l(\vec{U_g} - \vec{U_l})\times(\vec{\nabla}\times\vec{U_l}), \tag{6.13}$$

which, in the frame of a preferential direction, fully established co-current shear flow, reduces to

$$\vec{F_{g,lift}} = -C_l\epsilon\rho_l|\vec{U_g} - \vec{U_l}|\frac{\partial U_l}{\partial r}\vec{e_r}. \tag{6.14}$$

The lift coefficient is typically $C_l = 0.5$ for a single particle in shear flows. Values of $C_l = 0.05$ to 0.3 were reported to properly describe the wall-peaking void fraction experiments in pipes with the Euler-Euler formulation (Antal *et al.*, 1991; Lance

and Lopez de Bertodano, 1994; Lopez de Bertodano, 1994). More recently, some models for the lift coefficient dependence on the bubble shape were proposed from bubble tracking experiments (Tomiyama, 1998; Tomiyama *et al.*, 2002b). In those experiments the shape of the bubbles was found to affect the symmetry of the bubble wake, and its interaction with the shear field. This resulted in a negative equivalent lift force coefficient for large bubbles. Lucas *et al.* (2001) showed, by using the model proposed by Tomiyama (1998) and Tomiyama *et al.* (2002b) in a two-fluid model that both the wall peaking and core peaking radial void fraction distributions could be qualitatively described. This model is given by:

$$C_l = \begin{cases} min[0.288tanh(0.121R_e), f(E_{o_d})] & \text{for } E_{o_d} < 4 \\ f(E_{o_d}) & \text{for } 4 < E_{o_d} < 10.7 \\ -0.29 & \text{for } 10.7 < E_{o_d} \end{cases}$$

with $f(E_{o_d}) = 0.00105{E_{o_d}}^3 - 0.0159{E_{o_d}}^2 - 0.0204E_{o_d} + 0.474$.
The bubble lift force coefficient is then dependent on the bubble Reynolds number $R_e = \frac{\rho_l U_r D_b}{\mu_l}$ for small bubbles. For larger bubbles (typicaly $D_b > 1mm$ for air-water flows), the lift force coefficient is essentially affected by the bubble shape through a modified Eötvös number given by

$$E_{o_d} = \frac{g(\rho_l - \rho_g){D_H}^2}{\sigma}, \tag{6.15}$$

where D_H is the maximum horizontal dimension of the bubble. This maximum horizontal dimension is computed using the correlation proposed by Wellek *et al.* (1966) for the ellipsoidal-bubble aspect ratio:

$$D_H = D_b(1 + 0.163{E_o}^{0.757})^{1/3}, \tag{6.16}$$

in which the Eötvös number is given by

$$E_o = \frac{g(\rho_l - \rho_g){D_b}^2}{\sigma}. \tag{6.17}$$

6.4.2.3 Wall force

A local wall force, which acts to drive the bubbles away from the wall has been modeled by Antal *et al.* (1991), following a similarity with lubrication theory. This wall force is expressed as:

$$\vec{F_{g,wall}} = -\frac{\epsilon\rho_l|\vec{U_g} - \vec{U_l}|^2}{R_b}\left(C_{w1} + C_{w2}(\frac{R_b}{y_0})\right)\vec{e_r}, \tag{6.18}$$

where: $C_{w1} = -0.06|\vec{U_g} - \vec{U_l}| - 0.104$, $C_{w2} = 0.147$ and $y_0 = R - r$ is the local distance from the wall. This force is only valid in the near wall region, and should tend to zero when the distance from the wall increases. The wall-repulsion force is taken into account for $F_{g,wall} < 0$, i.e for $r > R + \frac{C_{w2}R_b}{C_{w1}}$ (Tomiyama, 1998; Troshko and Hassan, 2001). This wall force brought significant improvements for a proper near wall void fraction description: the void fraction is observed to decrease

towards a value of zero at the wall (we also observed this void fraction decrease in our experiments), while two-fluid models based on the lift force only would predict a maximum void fraction value at the wall for small bubbles. Since the void fraction is zero at the wall, the bubble relative velocity $U_r = U_{r,wall}$ in equation (6.18) is estimated by using the relative velocity of a single bubble in an infinite medium in our model (Peebles and Garber, 1953).

6.4.2.4 Dispersion force

The turbulence in the liquid has the tendency to redistribute the phase fractions heterogeneities. To model this effect, a turbulence dispersion term is included in the model. Contrary to microscopic diffusion terms included in the mass conservation equation, this effect is taken into account by an additional turbulent dispersion force in the momentum conservation equation (Drew, 2001; Moraga *et al.*, 2003). Following a diffusion approach, this force is modelled as (Politano et al., 2003; Carrica *et al.*, 1999; Hill *et al.*, 1995; Troshko and Hassan, 2001):

$$\vec{F_{g,td}} = -\frac{3}{8}\rho_l \nu_t \frac{C_d}{R_b}|\vec{U_g} - \vec{U_l}|\frac{\partial \epsilon}{\partial r} \tag{6.19}$$

In this formulation ν_t is the turbulent viscosity, taken from the model described in section 6.4.4.

6.4.3 Interfacial pressure

The area averaged interfacial pressures P_{lI} and P_{gI} need to be related to the spatial average of the pressure. Near to the bubble surface, the liquid velocity is larger than the far field velocity. This results in a pressure difference, approximated by a potential flow solution:

$$P_{lI} - P_l = -C_p \rho_l (1-\epsilon)|\vec{U_g} - \vec{U_l}|^2 \tag{6.20}$$

In this expression the coefficient $C_p = \frac{1}{4}$ is valid for spherical particles (Stuhmiller, 1977). For oblate spheroid bubbles, this coefficient can be up to 0.71 (Lance and Lopez de Bertodano, 1994), while the value $C_p = 1$ is used in Lopez de Bertodano (1994) and Politano et al. (2003), who considered large bubbles. For comparing our results with the work reported by these authors (and in view of the lack of correlations for C_p), we will use the value $C_p = \frac{1}{2}$. In contrast from P_{lI}, the following hypothesis is valid for the gas phase due to its low density: $P_{gI} = P_g$.

6.4.4 Reynolds stress closure

The Reynolds stress tensor $\boldsymbol{\tau}_{Re} = \langle\langle \rho_k \dot{\vec{u_k}} \dot{\vec{u_k}}^t \rangle\rangle$ is approximated using an eddy-viscosity approach based on the bubbly flow algebraic model proposed by Sato et al. (1981). The total eddy viscosity is given by

$$\nu_t = \nu_{t_0} + \nu_{t_b}, \tag{6.21}$$

where ν_{t_0} and ν_{t_b} are respectively the contribution of wall friction and bubble induced turbulence. The wall friction effects are modelled following Reichardt (1951) and

including a wall damping function $f(y^+)$ as proposed by Van Driest (1956) for a realistic prediction in the near wall region:

$$\nu_{t_0} = \frac{KRu_L{}^*}{6}(1 - r^{*2})(1 + 2r^{*2})f(y^+), \tag{6.22}$$

in which $f(y^+) = (1 - e^{\frac{-y^+}{A^+}})^2$, $A^+ = 26$, $K = 0.41$, $y^+ = \frac{yu^*}{\nu}$, $r^* = \frac{r}{R}$, $u_L{}^* = \sqrt{\frac{\tau_w}{\rho}}$ and $\tau_w = \frac{R}{2}(\frac{\partial P}{\partial z})_f$. The bubble induced term is given by the model of Sato et al. (1981), also weighted by the wall damping function as suggested by Van Driest (1956):

$$\nu_{t_b} = k_1 \epsilon R_b |\vec{U_g} - \vec{U_l}| f(y^+), \tag{6.23}$$

with:

$$k_1 = \begin{cases} k_{1,Max} & \text{if } r < R - R_b \\ -\frac{k_{1,Max}}{R_b - d_c} r - \frac{k_{1,Max}}{d_c - R_b}(R - d_c) & \text{if } R - R_b < r < R - d_c \\ 0 & \text{if } r > R - d_c \end{cases}$$

Since no bubbles are found very near to the wall (for $r > R - d_c$), the bubble-induced term is neglected in this part. The thickness of this layer is taken as $d_c = 20\mu m$ (Sato et al., 1981). The centreline value of k_1, given by $k_{1,Max}$, was found to be in the range of 1 to 1.4 by Sato et al. (1981). In some of our model results, the best agreement was found for lower values of $k_{1,Max}$. We however will use the value of $k_{1,Max} = 1.2$ recommended by Sato et al. (1981) for our investigation, since we want to develop a model free of input from individual experiments.

It should be noted that an additional contribution for taking into account the motion of the liquid around the bubbles can be added to this Reynolds stress formulation (Antal *et al.*, 1991; Politano et al., 2003):

$$\boldsymbol{\tau}_{Re,b} = -\rho_l \frac{3}{20} \epsilon |\vec{U_g} - \vec{U_l}|^2 \mathbf{I_d}. \tag{6.24}$$

In our model this term was neglected, the contribution due to the interfacial pressure being significantly larger by using $C_p = \frac{1}{2}$ in equation (6.20).

6.4.5 Boundary conditions

The boundary conditions used are the following:

- No-slip condition for the liquid phase: $\vec{U_l}(r = R) = 0$,
- the flow is axially symmetric: $\frac{\partial U_l}{\partial r}(r = 0) = 0$,
- the area averaged void fraction is specified: $< \epsilon > = c$,
- the superficial liquid velocity value U_{sl} is specified, and the pressure gradient $\frac{\partial P}{\partial z}$ is determined accordingly.

6.5 Final formulation

6.5.1 Simplified set of equations

Following the formulation given in equations (6.6) and (6.7) and the hypothesis, the system is explicitly written for the gas and the liquid phase. Using $\nu_t = \frac{\mu_t}{\rho_l}$, $U_r = |\vec{U_g} - \vec{U_l}|$ and projecting on the r and z axis leads to:

$$\frac{\partial P_g}{\partial z} = \rho_g g - \frac{3}{8}\frac{1}{R_b} C_d \rho_l {U_r}^2 \tag{6.25}$$

$$\epsilon \frac{\partial P_g}{\partial r} = -C_l \epsilon \rho_l U_r \frac{\partial U_l}{\partial r} - \frac{\epsilon \rho_l {U_r}^2}{R_b}[C_{w1} + C_{w2}(\frac{R_b}{R-r})] - \frac{3}{8}\mu_t \frac{C_d}{R_b} U_r \frac{\partial \epsilon}{\partial r} \tag{6.26}$$

$$(1-\epsilon)\frac{\partial P_l}{\partial z} = (1-\epsilon)\frac{1}{r}\frac{\partial}{\partial r}[r(\mu_l + \mu_t)\frac{\partial U_l}{\partial r}] + (1-\epsilon)\rho_l g + \frac{3}{8}\frac{\epsilon}{R_b} C_d \rho_l {U_r}^2 \tag{6.27}$$

$$\begin{aligned}(1-\epsilon)\frac{\partial P_l}{\partial r} = &-C_p \rho_l {U_r}^2 (1-\epsilon)\frac{\partial \epsilon}{\partial r} + C_l \epsilon \rho_l U_r \frac{\partial U_l}{\partial r} \\ &+ \frac{\epsilon \rho_l {U_r}^2}{R_b}[C_{w1} + C_{w2}(\frac{R_b}{R-r})] + \frac{3}{8}\mu_t \frac{C_d}{R_b} U_r \frac{\partial \epsilon}{\partial r}\end{aligned} \tag{6.28}$$

The gas phase velocity follows from $U_g(r) = U_l(r) + U_r$, since the relative velocity was assumed to be constant in the radial direction in the present model. The drag coefficient C_d was computed by using the area average void fraction $< \epsilon >$ in equation (6.12). Equation (6.26) to (6.28) are combined to further simplify the numerical formulation.

6.5.2 Numerical formulation

For convenience, the following variables are introduced: $a_l(r) = \frac{\partial U_l}{\partial r}$ and $\alpha(r) = 2\pi \int \epsilon r dr$. Since we want to adjust the pressure gradient for a given liquid volumetric flux U_{sl} and area-average void fraction $< \epsilon >$, we also introduce $\gamma = \frac{\partial P}{\partial z}$, and the cumulative liquid flux $J_l(r) = \frac{2}{R^2}\int (1-\epsilon) U_l r dr$. The set of equations to solve is a system of six first order differential equations, strongly coupled through the void fraction ϵ and the liquid velocity U_l:

$$\frac{\partial \gamma}{\partial r} = 0 \tag{6.29}$$

$$\frac{\partial J_l}{\partial r} = \frac{2}{R^2}(1-\epsilon) U_l r \tag{6.30}$$

$$\frac{\partial \alpha}{\partial r} = 2\pi \epsilon r \tag{6.31}$$

$$\frac{\partial U_l}{\partial r} = a_l(r) \tag{6.32}$$

$$\frac{\partial a_l}{\partial r} = \frac{\frac{\partial P}{\partial z} - \rho_l g}{\mu_l + \mu_t} - (\frac{1}{r} + \frac{1}{\mu_t + \mu_l}\frac{\partial \mu_t}{\partial r})a_l - \frac{3C_d\rho_l {U_r}^2}{8R_b(\mu_l + \mu_t)}\frac{\epsilon}{1-\epsilon} \tag{6.33}$$

$$\frac{\partial \epsilon}{\partial r} = \frac{-C_l\rho_l U_r a_l \epsilon - \frac{\epsilon\rho_l {U_r}^2}{R_b}(C_{w1} + C_{w2}\frac{R_b}{R-r})}{\epsilon(1-\epsilon)C_p\rho_l {U_r}^2 + \frac{3}{8}\mu_t\frac{C_d}{R_b}U_r} \tag{6.34}$$

The quantities of input are the following: the area averaged void fraction $< \epsilon >$, the superficial liquid velocity U_{sl} and the bubble radius R_b. Reformulating the boundary conditions for our set of equations leads to:

- No-slip condition for the liquid phase $\vec{U_l}(R) = 0$,
- the flow is axialy symmetric: $a_l(0) = 0$,
- the area averaged void fraction specification: $\alpha(0) = 0$ and $\alpha(R) = \pi R^2 < \epsilon >$,
- to specify the liquid input, we impose $J_l(0) = 0$ and $J_l(R) = U_{sl}$.

A set of six unknown has to be determined by using 6 ODES with 6 boundary conditions. The D02RAF NAG FORTRAN library was used, which is suitable for a full non-linear problem. A deferred correction technique and Newton iterations were implemented. Since the lift force was a source of strong gradients, a continuation parameter was used to increase progressively the lift force coefficient magnitude in an iterative loop. Typical computations consisted in 50 iterations on the lift force, and used 10000 to 50000 mesh points. The numerical results are provided for a maximum norm corresponding to an error of less than 5.10^{-6} on the void fraction values.

6.6 Results

6.6.1 Model validation

6.6.1.1 Comparison with experiments from literature

To validate our simplified model, two sets of experimental data collected at differing liquid input and pipe diameter conditions are used:

a- The experiment of Serizawa *et al.* (1975) in an air-water $60mm$ diameter pipe at $U_{sl} = 1.03m/s$, $U_{sg} = 0.21m/s$ and $D_b = 4mm$, and

b- the experiments of Liu and Bankoff (1993b) in an air-water $38mm$ diameter pipe at $U_{sl} = 0.753m/s$, $U_{sg} = 0.23m/s$ and $D_b = 4.1mm$.

The results for the void fraction and radial profiles of liquid velocity obtained for those two experiments are shown in figure 6.1. The model allows describing correctly the void fraction and liquid velocity for both pipe diameter values. The magnitude

of the liquid velocity gradient at the wall is somehow underestimated (figure 6.1(b)). However similar effects can be found when using more elaborated models, such as $k-\epsilon$ turbulence modelling, in which in general the wall shear stress is found to be slightly under-predicted (Politano et al., 2003). The current model is therefore found to capture the relevant physical mechanism with a relatively reasonable confidence. A better description of the liquid velocity profile was found by neglecting the bubble eddy viscosity contribution, corresponding to $k_{1,Max} = 0$ in equation (6.23) (see figure 6.2). This is consistent with the eddy-viscosity model developed in Chahed *et al.* (2003): the authors reported that the eddy viscosity in bubbly flow can be larger or lower than the corresponding single phase flow eddy viscosity, depending on a competition between bubble agitation (which tends to increase the eddy viscosity), and shear stress attenuation due to turbulent isotropization by the bubbles (which

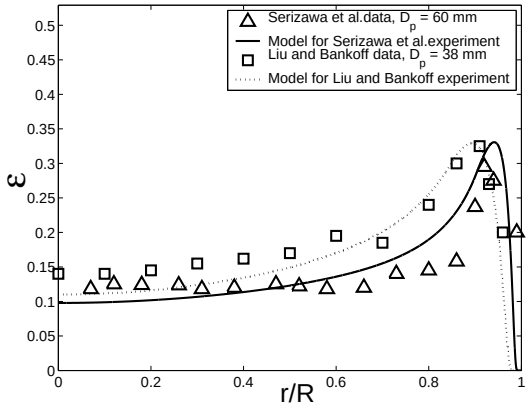

(a) Void fraction

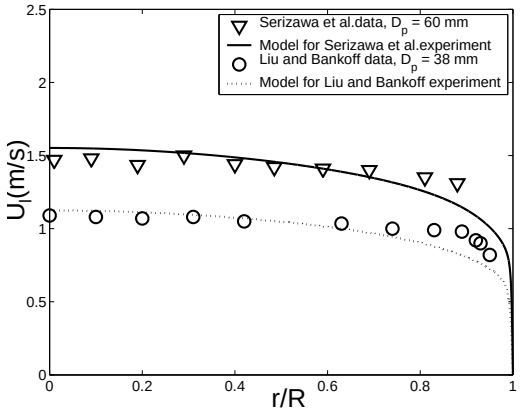

(b) Liquid velocity

Figure 6.1: Comparison between the experimental data of Serizawa *et al.* (1975) and Liu and Bankoff (1993b) with the model results (with $k1(r=0) = 1.2$ in equation 6.23): (a) Void fraction, (b) Liquid velocity.

decreases the appropriate eddy viscosity value). Also experimental investigations reported these turbulence damping effects (Serizawa *et al.*, 1994). Since we want to capture the main trends with our simplified phenomenological model, we will however use the initially proposed value of $k_{1,Max} = cste = 1.2$ by Sato et al. (1981) in this first attempt.

6.6.1.2 Moderate liquid input predictions: bubble size effects

We compared the radial profile results obtained with the model with experiments carried out in our pipe flow experimental set-up of $72mm$ inner diameter. The comparison for $Re_{sl} = 16000$ and for two bubble size values are presented in figure 6.3. The model is able to capture the wall and core peaking void fraction profiles associated with increased bubble diameter. Also, the liquid velocity evolution is well

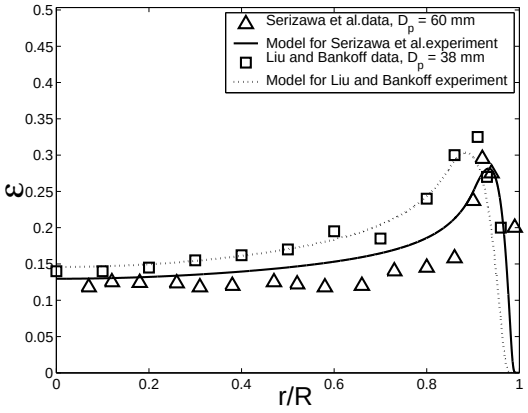

(a) Void fraction

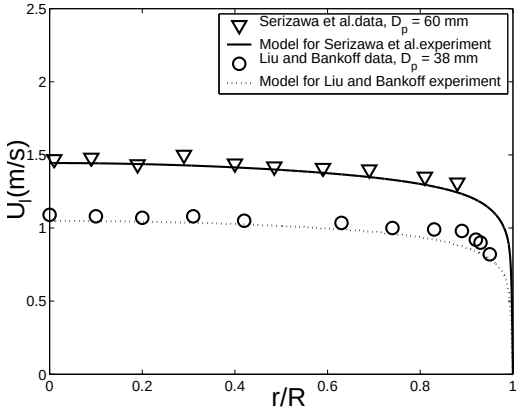

(b) Liquid velocity

Figure 6.2: Comparison between experimental data model results when neglecting the bubble eddy viscosity (i.e.using $k_1 = 0$ in equation 6.23).

described by the model, changing from a flat to a parabolic profile with increased bubble size. However, the profiles associated with the large bubble size experimental conditions are not as well predicted as the small bubble situation. This is attributed to the large distribution of bubble size during the large bubble experiments. Bubbles with a spherical equivalent diameter of less than $5mm$ were measured by our four-point probe near the wall location during this experiment. Therefore, to describe more closely the profiles, a multiple-bubble size classes model such as the one developed by Lucas *et al.* (2001) and Politano et al. (2003) would be needed. Also, a number of coefficients used in this model, such as C_p and C_d, might be changing with bubble size. However, our simplified model is found to properly capture the main effect of an increased bubble size on the radial profiles.

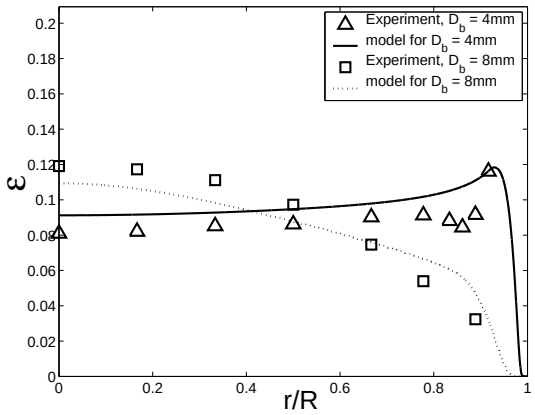

(a) Void fraction

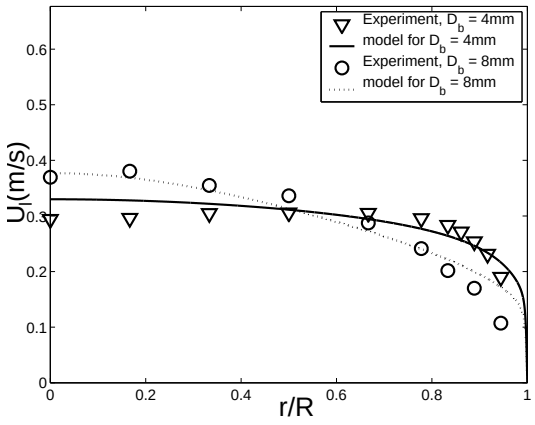

(b) Liquid velocity

Figure 6.3: Predictions obtained for our $72mm$ inner diameter pipe flow, for $Re_{sl} = 16000$, and for $D_b = 4$ and $8mm$. The model results are compared with experiments corresponding to $D_b = 4mm$ and $D_b \approx 8mm$.

6.6.1.3 Bubble column predictions

We also computed the void fraction and liquid velocity associated with various bubble size and void fraction conditions in an air-water bubble column, i.e. for $U_{sl} = 0$. In figure 6.4, the void fraction and liquid velocity profiles obtained for two bubble diameter ($D_b = 4mm$ and $8mm$) and for an area average void fraction $< \epsilon >= 0.05$ are presented.

As observed in bubble column experiments, we obtain a liquid down-flow at the wall (Clark *et al.*, 1990; Mudde *et al.*, 1997; Mudde and Saito, 2001). Although we use a turbulent pipe flow model for the eddy viscosity as suggested by Sato et al. (1981), the liquid velocity trends associated with bubble column conditions are qualitatively in agreement with experimental observations. Due to the change of sign of the lift force coefficient when varying the bubble diameter, the void fraction

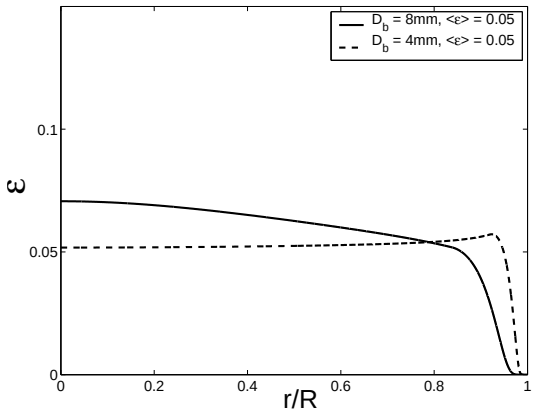

(a) Void fraction

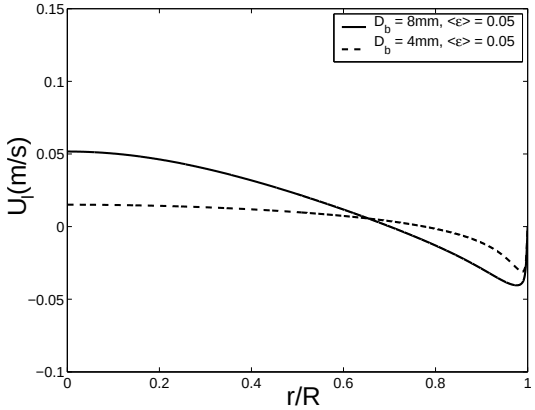

(b) Liquid velocity

Figure 6.4: Typical void fraction and velocity radial profiles in the bubble column mode as predicted by the model for $D_b = 4mm$ and $D_b = 8mm$, and for $< \epsilon >= 0.05$.

profile is almost flat for small bubbles, while we obtain a parabolic profile for core peaking conditions. The liquid re-circulation is decreased when using small bubbles: the small bubbles are accumulating in the negative velocity part of the flow, thus preventing the falling liquid flow by locally increasing the void fraction.

6.6.1.4 Low liquid input predictions

We also compare our simulations with experimental results collected at low Re_{sl} conditions. In those conditions, a liquid down-flow at the wall was also found. In figure 6.5, we compare the void fraction and velocity measurements with model predictions for $Re_{sl} = 1200$; $D_b = 6.5mm$ and a low area average void fraction $< \epsilon >= 0.01$. In those conditions, the profiles of void fraction and liquid velocity were properly predicted with our model.

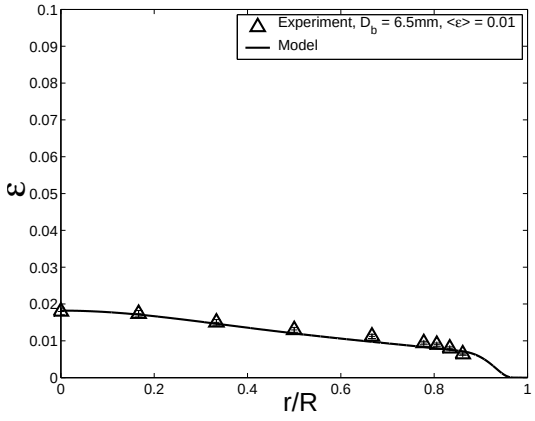

(a) Void fraction

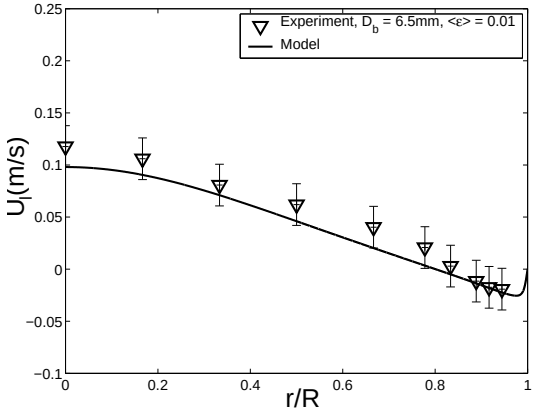

(b) Liquid velocity

Figure 6.5: Velocity profiles obtained from the model and the experiments at $Re_{sl} = 1200$, $< \epsilon >= 0.01$ and $D_b = 6.5mm$: (a) Void fraction, (b) Liquid velocity.

At increased void fraction, the liquid re-circulation was however systematically under-predicted by our model, independently from the bubble size conditions (see figure 6.6 for $Re_{sl} = 1200$, $D_b = 8mm$ and $< \epsilon >= 0.09$). This can be connected to a number of effects, such as the poly-disperse aspects of the medium due to bubble fragmentation, bubble entrainment in the down-flow regions, and bubble coalescence. Also, our pipe flow eddy-viscosity model is clearly not appropriate for low liquid input flows, for which the pipe Reynolds number is below the critical value corresponding to the transition to turbulence. In those conditions our simplified approach is therefore of limited interest. Our drift-flux distribution parameter computations will be restricted to turbulent pipe flow conditions (we will use $Re_{sl} = 2000$ as a lower limit for the computations).

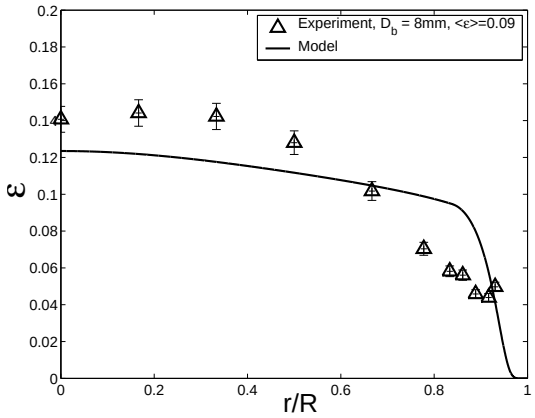

(a) Void fraction

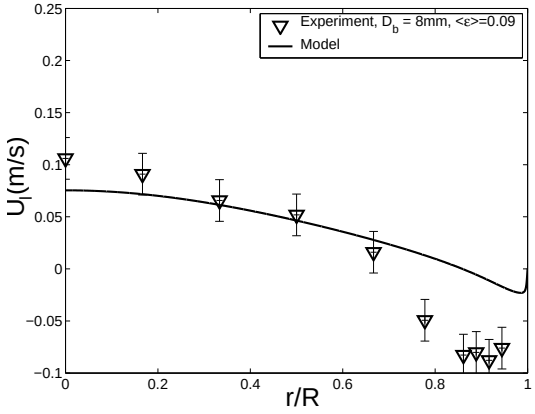

(b) Liquid velocity

Figure 6.6: Comparison of the void fraction and velocity radial profiles obtained from the model and the experiments at $Re_{sl} = 1200$, $< \epsilon >= 0.09$ and $D_b = 8mm$: (a) Void fraction, (b) Liquid velocity. In that case the liquid re-circulation is under-predicted by the model.

6.6.2 Drift-flux distribution parameter

In this section we use our model for making predictions of the change of the distribution parameter with liquid input and bubble size in our $72mm$ diameter air-water pipe flow. For that purpose, we carry out series of simulations at varied $U_{sl} = J_l(R)$ and R_b values. The distribution parameter, defined by equation (6.3) in the drift-flux model (Zuber and Findlay, 1965) is calculated for each simulation by using the computed profiles. These results are compared with the experimental values of the distribution parameter C_0 obtained in chapter 5.

6.6.2.1 Liquid input

We computed the effect of the liquid input for two different values of the bubble size corresponding to $D_b = 4mm$ and $D_b = 8mm$, as shown in figure 6.7(a).

The area average void fraction was kept constant at $< \epsilon >= 0.1$ in those calculations. A few simulations were also done at varied void fraction conditions. No significant changes were found. We observe a significant increase of the C_0 parameter at decreased liquid input, due to the appearance of liquid re-circulation in the near wall region. It is interesting to note that reducing the bubble size reduces the C_0 parameter at any liquid input conditions. This is also observed in the experiments: the liquid re-circulation was prevented by the small bubbles, therefore reducing C_0. In figure 6.7(b) we also plot our experimental data collected for two different type of bubble size conditions, corresponding to the wall peaking of void fraction ($D_b < 5mm$) and the core peaking radial profile of void fraction ($D_b > 5mm$). The numerical simulation and experiments are describing the same behaviour at low liquid input for large bubbles: the C_0 parameter increases significantly when reducing the liquid input below $Re_{sl} < 10000$. Each C_0 experimental point is computed ac-

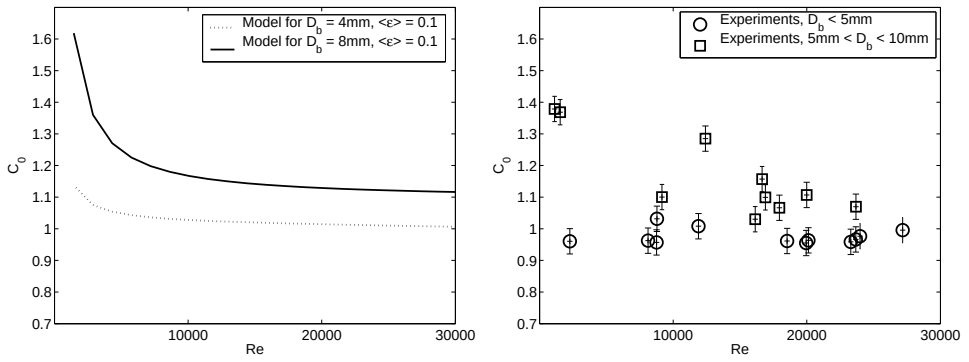

(a) Model (b) Experiments

Figure 6.7: Distribution parameter as a function of the liquid input Reynolds number: (a) model results for $D_b = 4mm$ and $D_b = 8mm$ with $< \epsilon >= 0.1$; (b) Experimental results at various area average void fraction conditions. The experiments are separated in wall peaking void fraction conditions ($D_b < 5mm$) and core peaking ($D_b > 5mm$).

cording to measured void fraction and velocity profiles. During these experiments, the void fraction has been varied from $< \epsilon >= 0.01$ to $< \epsilon >= 0.2$. This explains the scatter in the experimental data. However, it is clear from this plot, that the bubble size is one of the most important parameter for a proper description of the flow and accurate pressure drop predictions, due to the associated void fraction profile changes.

6.6.2.2 Bubble size

We also computed the C_0 parameter for various bubble size values when operating at a fixed large liquid input, for which no liquid down-flow at the wall was obtained. This condition corresponds to $U_{sl} = 1.39m/s$, i.e. $Re_{sl} = 100000$. The area average void fraction was fixed at $< \epsilon >= 0.1$. The results are shown in figure 6.8(a).

In figure 6.8(b) we also show experimental data collected in our experimental set-up at large liquid input conditions, for conditions at which no liquid down-flow was measured at the wall. These measurements are corresponding to $Re_{sl} > 20000$. The numerical results show the same behavior as in the experiments: due to the lift force changes with bubble size, the C_0 parameter changes drastically near to $D_b = D_{b,neutral}$ ($D_{b,neutral}$ being the bubble diameter associated with a 'neutral' lift force, i.e. $C_l = 0$: $D_{b,neutral} = 5.8mm$ for water). Small bubbles ($D_b < D_{b,neutral}$) lead to $C_0 \approx 0.9 - 1$, while larger bubbles ($D_b > D_{b,neutral}$) give $C_0 \approx 1.1 - 1.2$. There is however a shift between the experimental and numerical results. This is attributed to the differences of liquid input and void fraction conditions during the experiments and for the simulations, as well as the method of evaluation of the spherical-equivalent bubble size during the experiments, which was based on the correlation of Wellek *et al.* (1966) for connecting the spherical equivalent diameter to the measured bubble vertical chord length. In the next section, we will compare the superficial gas velocity values associated with these experimental conditions.

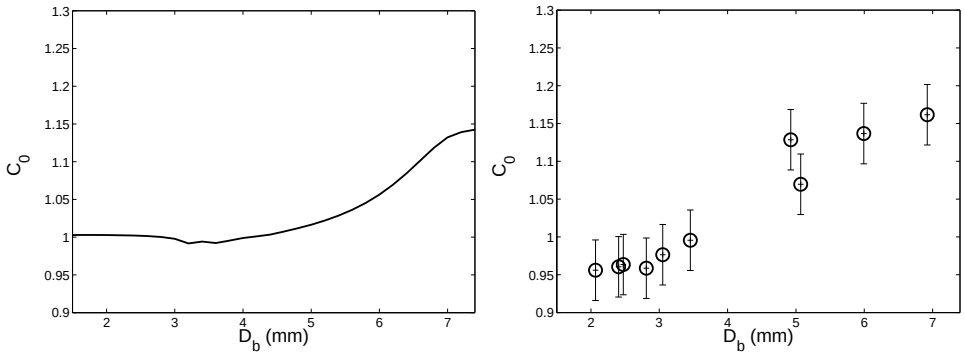

(a) Model (b) Experiments

Figure 6.8: Distribution parameter as a function of the spherical-equivalent bubble diameter: (a) Simulation results for $Re_{sl} = 100000$, $D_p = 72mm$, and $< \epsilon >= 0.1$; (b): Collected experiments for $D_p = 72mm$, $Re_{sl} > 20000$ and various area average void fraction conditions.

6.6.2.3 Superficial gas velocity

In practical laboratory and gas-lift conditions, the input gas flow rate is known, rather than the area-average void fraction. Our model would therefore have to be used in an iterative way for predicting the pressure drop associated with a given gas input. We therefore investigate in this section whether our model is able to predict the superficial gas velocity associated with given void fraction and bubble size conditions. We compared our predicted superficial gas velocity values with experimental data collected for various bubble diameter and void fraction conditions. In those simulations the liquid input, area average void fraction and mean spherical-equivalent bubble diameter were taken from the measurements. The superficial gas velocities as measured by area averaging our gas flux measurements (using the four-point optical fibre probe technique) are compared with the associated model predictions in figure 6.9. The comparison is reasonable regarding the accuracy of the measurement technique, and the simplicity of our model. Improvements are expected if we would consider the changes of the relative velocity with local void fraction, by using the local void fraction in the drag coefficient C_d. These changes of relative velocity with local void fraction were confirmed by our experiments.

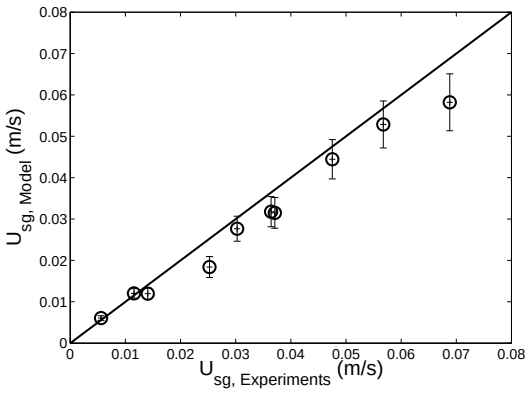

Figure 6.9: Comparison between the superficial gas velocity taken from the experiment and the model predictions. For each simulation the area average void fraction and mean bubble diameter are taken from the corresponding measurement.

6.7 Conclusion

In this contribution a simplified model, based on the two-fluid Euler-Euler modelling approach, has been developed for predicting the void fraction and velocity radial profiles associated with given bubble size and liquid input conditions. This model is able to capture the main trends associated with bubble size and liquid input changes. The most important phenomena are: (1) the transition from wall peaking to core peaking of void fraction for increased bubble diameter, and (2) the liquid down-flow at the wall for low liquid input conditions.

In our two-fluid model, we used the lift force coefficient correlation suggested by Tomiyama *et al.* (2002b) for taking into account the bubble shape effects. This force term was found to be crucial for properly describing the changes of void fraction radial profiles with increased bubble size. This also had an impact on the liquid velocity profiles. At low liquid input, the liquid down-flow at the wall was enhanced when increasing the bubble size, due to an increased mixture density in the down-flow region. This behaviour was also observed in the experiments.

From the void fraction and velocity profiles obtained at various flow conditions, we computed the drift-flux distribution parameter C_0 as defined in Zuber and Findlay (1965). A reasonable description of the distribution parameter as a function of bubble size and liquid input was achieved. Typical values were $C_0 \approx 1$ for small bubbles at large liquid input, and up to $C_0 > 1.5$ for large bubbles at low liquid input.

The present model could be further improved by using an eddy-viscosity model able to predict turbulence damping, as the one suggested by Chahed *et al.* (2003), and by taking into account the bubble velocity fluctuations and the associated effects on the interfacial forces, as suggested in Lathouwers (1999) and Chahed *et al.* (2003). Such an additional contribution could be included by using the approach described in Mudde and Simonin (1999). For a proper up-scaling of gas-lift conditions as encountered during the application, it would also be interesting to extend the present model to large pressure conditions.

Chapter 7

Conclusion

The aim of this thesis was to study the influence of the initial bubble size and distribution on the development of a vertical upward bubbly pipe flow and the associated consequences on the gas-lift technique efficiency. A bubbly pipe flow of height $18m$ and diameter $72mm$ was used at moderate liquid input flow conditions, and different bubble injectors were tested. The effects of bubble size could be separated in essentially three main contributions: the flow pattern changes, the transverse distribution (of void fraction and velocity), and the relative velocity between the phases. In this last chapter, the general conclusions are presented. We also give some suggestions for gas-lift up-scaling and further research.

7.1 Conclusions

7.1.1 Measurement techniques

To separate the different contributions associated with bubble size changes, we developed and used local measurement techniques.

- We investigated the feasibility of performing Laser Doppler measurements to determine the liquid velocity in our flow configuration. Such measurements were found to provide meaningful time average velocity information.
- For determining the bubble size and investigating the coupling effects between the bubble and liquid velocity through the local void fraction, we used a four-point optical fibre probe. A bubble selection criterion was applied to select the bubbles rising along the axis of the probe. A bubble mean time of flight approach was used for computing the associated bubble velocity and chord length (Frijlink, 1987). This approach gave accurate results.
- We developed an approach for estimating the bubble shape and orientation by using the signal provided by a four point optical fibre probe. This method was first validated by comparisons with synthetic data and single bubble stereoscopic images. The results obtained by applying this technique to our multiple-bubble pipe flow measurements were supported by available bubble shape correlations. Also, the bubble orientation results were consistent with observations on single bubbles in a linear shear flow (Tomiyama *et al.*, 2002b).

7.1.2 Bubbly pipe flow measurement results

We investigated the effects of bubble size and concentration distribution on the gas-lift technique by using in-situ bubble size measurements.

- The initial bubble size significantly affected the transition from bubbly flow to slug flow, which in turn had a detrimental effect on the gas-lift efficiency. This transition boundary could be properly described by using a bubble size dependent critical void fraction relation, as observed in Song *et al.* (1995) for small diameter pipes.

- The initial bubble concentration distribution could have a strong impact on the bubbly to slug flow transition, due to locally increased void fraction values and quick bubble coalescence in case of a non-symmetric, vertically oriented porous injector.

- When operating in bubbly flow, reducing the bubble size clearly improved the gas-lift efficiency. These improvements were due to:

  a- the reduction of the bubble relative velocity with decreased bubble size, which in turn increased the area average void fraction for given mean flow conditions,

  b- the radial distribution of void fraction and phases velocities: small bubbles formed a wall peaking void fraction profile, while large bubbles migrated toward the centre of the pipe.

A specific measurement section was developed to measure the coupling effects between the void fraction and the phase velocity profiles. This measurement section consisted in a four-point optical fibre probe and a backscatter Laser Doppler Anemometry probe. Both probes could be traversed in the radial direction to investigate the radial profiles of void fraction and velocities. With an increased bubble size, not only the void fraction transverse distribution but also the phase velocity profiles were changing. This also contributed to the changes in gas-lift efficiency. Using these measurements we computed the drift-flux parameters C_0 and $|U_{drift}|$. The measured weighted mean drift velocity increased with the spherical-equivalent bubble diameter. Also the drift-flux distribution parameter was increasing with bubble diameter, from $C_0 \approx 0.95$ for small bubbles to $C_0 > 1.1$ for a centreline peaking void fraction profile associated with large bubbles. At low liquid input conditions, much larger distribution parameter values were obtained, due to a liquid down-flow at the wall.

Based on our measurement results we developed bubble size and liquid input dependent drift-flux parameter models for quantifying the contributions due to these effects. Comparisons with separately collected pressure data associated with various bubble size conditions confirmed the validity of these correlations.

7.1.3 Euler-Euler modelling

We developed a numerical model for predicting the void fraction and velocity profiles associated with bubble size changes. This model properly described the void fraction changes by using a bubble size dependent lift force model (Tomiyama *et al.*, 2002b). The drift flux distribution parameter was computed from this numerical model, and compared with our experiments. A reasonable agreement was found. The turbulence modelling was however included in a simplistic way in this phenomenological model. Improvements can be expected by using more elaborated models for the eddy viscosity, and for the bubble velocity fluctuations.

7.2 Gas-lift up-scaling

The experimental conditions investigated in the present study showed that during gravity-dominated gas-lift conditions, reducing the bubble size and injecting the bubbles symmetrically at the wall improved the efficiency of the technique.

The transition from bubbly flow to slug flow was affected by the bubble size conditions. This effect was also observed at increased viscosity and decreased surface tension by using a water-glycerol mixture. The bubble size dependent correlation used for the flow pattern transition, developed in chapter 4 and validated for air-water flows, will however be different if the surface tension and viscosity properties are changed. As reported in section 4.3.2.3, reducing the surface tension changes the critical void fraction associated with the bubbly to slug flow transition. Also, the liquid viscosity is reported to shift the boundary from bubbly flow to slug flow to lower superficial gas velocity conditions (Furukawa and Fukano, 2001).

At low liquid input conditions, the bubble relative velocity changes can have significant effects on the gas-lift efficiency. The increased gas density at large pressure will tend to reduce the drift velocity values of small bubbles, therefore improving the gas-lift efficiency. These effects have been observed in bubble columns (Krishna *et al.*, 1991; Luo *et al.*, 1999; Urseanu *et al.*, 2003) and small scale gas-lift systems (Letzel and Stankiewicz, 1999). These bubble relative velocity changes can in turn also affect the bubble break-up phenomena, particularly for large bubbles (Wilkinson *et al.*, 1993). The pressure conditions can therefore have important effects on the bubble size. Additional effects, such as internal gas re-circulation inside the bubbles (Luo *et al.*, 1999) might also affect the bubble break-up phenomena in those conditions.

In our experiments, we measured the wall peaking of void fraction when using small bubbles ($D_b < 5mm$) with a reduced surface tension liquid phase at low to moderate liquid input conditions. Experiments at increased liquid viscosity also indicated the existence of the wall peaking void fraction profile effects for small bubbles (Van Geest *et al.*, 2001). Based on our distribution parameter measurements, operating in the wall peaking void fraction regime rather than in the core peaking regime permits to significantly reduce the gravitational pressure gradient. The value of the critical bubble diameter associated with a bubble transverse migration towards the pipe centreline depends however on the fluid properties. As a first estimate, the critical bubble size associated with oil properties is $D_{b,crit} \approx 3 - 4mm$ according to the lift-force model proposed by Tomiyama *et al.* (2002b).

7.3 Recommendations

The measurement techniques used in the present study are potentially able to provide interesting information on the local structure of the flow. The four-point probe technique could be further developed to allow for the detection of spherical-cap bubbles from their associated signal. This would permit to gain accuracy when measuring in poly-disperse mixtures. The backscatter Laser Doppler Anemometry technique used in this thesis was found to be suitable for turbulence analysis. Therefore the LDA data collected during the present pipe flow experiments could be used for extracting more information on the changes due to bubble size. This would permit to improve our understanding on the turbulence changes due to bubble size.

In this thesis we studied the effect of bubble size on the pressure gradient in a vertical bubbly pipe flow when operating in the gravity-dominated regime. An interesting subject of further research would be to investigate how the frictional part of the pressure gradient is affected by the bubble size. This would ultimately permit to develop a model valid for gas-lift predictions at any combination of liquid input and bubble size conditions. Simultaneous measurements of area average void fraction and frictional pressure drop at increased liquid input would permit to investigate these effects. In this perspective, the simplified Euler-Euler model approach developed in the present work could be used for modelling the contribution due to gravity and friction, and might be extended for predicting such flow conditions.

In the present experiments, the pipe flow was operated at low pressure. High-pressure bubbly pipe flow experiments investigating both the bubble size and the axial pressure gradient would therefore be useful for up-scaling our results to down-hole pressure conditions. To model large pressure flow conditions, the numerical model developed in the present study would need to be extended for taking into account the stresses in the gas-phase.

Another particularity of gas-lift conditions is the presence of non-miscible liquid phases. Very often, at conditions were gas-lift is considered, a large volumetric fraction of water in oil can be found. It is therefore of interest to study how the two liquid phases are distributing in such gas-liquid-liquid flows, and whether the results obtained in this thesis are applicable to such conditions. For instance, the liquid phases might distribute in the radial direction in a specific way due to their significantly different properties. This might lead to some phase stratification effects. A follow-up of the present PhD research work is being carried out to study these flow conditions.

Appendix A

LDA turbulence measurement feasibility

In this apendix, we report some results on the feasibility of estimating the turbulence spectrum by using LDA data collected on the stirred vessel experimental set-up, described in section 3.2. The technique used for power spectrum fitting is the following:

1 First, the auto-correlation function is determined from the raw data. The auto correlation evaluation is done by using a combination of the 'fuzzy' and the local normalisation slotting technique, described in more detail in Van Maanen *et al.* (1999b).

2 Then the time auto correlation function is fitted with a least square method by a continuous function which depends on six parameters. This analytical expression follows from network theory, and no particular shape needs to be assumed 'à priori' (Van Maanen and Oldenziel, 1998).

3 Finally, the coefficients of the fitted auto-correlation function are used to generate the fitted turbulence spectrum. This fitting procedure had been shown to be flexible enough for a large range of flow situations.

In a high void fraction bubbly flow, the data rate can be expected to be significantly lower than in single-phase flow, due to:

1 the low probability of simultaneous beam penetration through the medium (Mudde *et al.*, 1998), and

2 the gaps in the signal due to bubble passages through the measurement volume itself (Mudde *et al.*, 1998).

In the case of bubbly flow re-sampling techniques might lead to non-physical results, since the physical gaps (generated by the bubble passages) would be replaced by interpolated liquid velocity data in the signal. The power spectrum curve-fit procedure, described above and in more detail in Van Maanen and Oldenziel (1998), has been shown to provide reasonable accuracy for such low data rate experiments. Therefore, this approach is followed in the present contribution.

In most cases the power spectra can be fitted by using the technique described above. Clear distinctions can be found between the low and high void fractions tests

(figures A.1.a and A.1.b). The turbulence power spectrum corresponding to low void fraction (figure A.1.a), done close to the impellers ($d_m = 50mm$, i.e $\frac{r}{r_{blade}} \approx 1$), shows a slope between $-\frac{5}{2}$ and $-\frac{5}{3}$. This is in agreement with previous results on stirred tank in single-phase flow (Van der Molen and Van Maanen, 1978): near to the impellers the non-equilibrium between turbulence production and dissipation affects the slope of the spectrum. The higher void fraction tests, done closer to the wall boundary, also show coherent properties. Improvements can be expected for a larger number of samples. The variance of the correlation coefficients at the smaller time-scales needs however to be reduced for estimating the power spectrum at the higher frequencies more accurately.

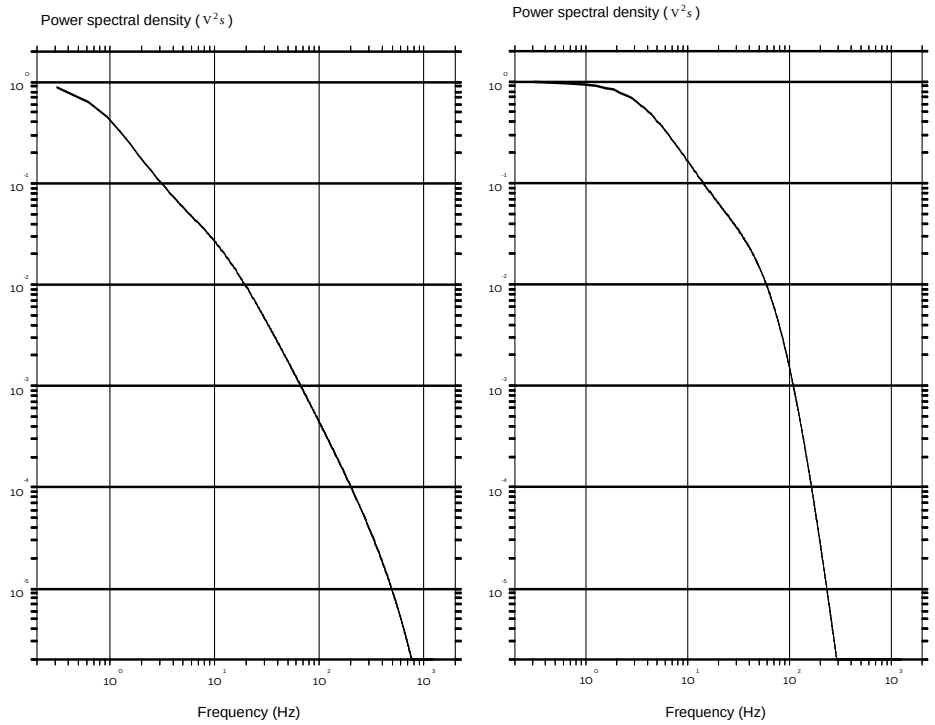

(a) (b)

Figure A.1: Fitted power spectrum of: (a) 0.08% void fraction test, bubble layer thickness of $50mm$, and (b) 20% void fraction test, bubble layer thickness of $30mm$.

Bibliography

Antal, S.P., Lahey, R.T., & Flaherty, J.E. (1991). Analysis of phase distribution in fully developed laminar bubbly two phase flow. *Int. J. Multiphase Flow*, 7, 635-652.

Barrau, E., Rivière, N., Poupot, Ch., & Cartellier, A. (1999). Single and double optical probes in air water two- phase flows: real-time signal processing and sensor performance. *Int. J. Multiphase Flow*, 25, 229-256.

Batchelor, G.K. (1989). A brief guide to two phase flow. *Theoretical and applied mechanics* (Eds Germain, Piau and Caillerie), Elsevier, Amsterdam, IUTAM, 27-40.

Bunner, B., & Tryggvason, G. (2002). Dynamics of homogeneous bubbly flows. Part 1. Rise velocity and microstructure of the bubbles. *J. Fluid. Mech.*, 466, 17-52.

Bunner, B., & Tryggvason, G. (2003). Effect of bubble deformation on the properties of bubbly flows. *J. Fluid. Mech.*, 495, 77-118.

Burgess, J.M., & Calderbank, P.H. (1975). The measurement of bubble parameters in two-phase dispersions. 1: The development of an improved technique. *Chem. Eng. Sci.*, 30, 743-750.

Carrica, P.M., Drew, D., Bonetto, F., & Lahey Jr., R.T. (1999). A polydisperse model for bubbly two-phase flow around a surface ship. *Int. J. Multiphase Flow*, 25, 257-305.

Cartellier, A. (1992). Simultaneous void fraction measurement, bubble velocity and size estimate using a single optical probe in gas-liquid two-phase flows. *Rev. Sci. Instrum.*, 63, 5442-5453.

Cartellier, A., & Barrau, E. (1998a). Monofiber optical probes for gas detection and gas velocity measurements: conical probes. *Int. J. Multiphase Flow*, 24, 1265-1294.

Cartellier, A., & Barrau, E. (1998b). Monofiber optical probes for gas detection and gas velocity measurements: optimized sensing tips. *Int. J. Multiphase Flow*, 24, 1295-1315.

Chahed, J. & Masbernat, L. (1998). Effet de parois sur la distribution de taux de vide dans les écoulements à bulles. *C. R. Acad. Sci.*, 326, Série 2b, 719-726.

Chahed, J., Roig, V., & Masbernat, L. (2003). Eulerian-Eulerian two-fluid model for turbulent gas-liquid bubbly flows. *Int. J. Multiphase Flow*, 29, 23-49.

Chen, X.T., Cai, X.D., & Brill, J.P. (1997). A general model for transition to dispersed bubble flow. *Chem. Eng. Sci.*, 52, 4373-4380.

Cheng, H., Hills, J.H., & Azzorpardi, B.J. (1998). A study of the bubble-to-slug transition in vertical gas-liquid flow in columns of different diameter. *Int. J. Multiphase Flow*, 24, 431-452.

Cheng, H., Hills, J.H., & Azzorpardi, B.J. (2002). Effect of initial bubble size on flow pattern transition in a 28.9 mm diameter column. *Int. J. Multiphase Flow*, 28, 1047-1062.

Clark, N.N., Egmond, J.W. van, & Nebiolo, E.P. (1990). The drift-flux model applied to bubble columns and low velocity flows. *Int. J. Multiphase Flow*, 16, 261-279.

Clift, R., Grace, J.R., & Weber, M.E. (1978). *Bubbles, drops and particles.* Academic press, New York.

Collins, R., Moraes, F.F., Davidson, J.F., & Harrison, D. (1978). The motion of a large gas bubble rising though liquid flowing in a tube. *J. Fluid. Mech.*, 89, 497-514.

De Vries, A. W. G. (2001). *Path and wake of a rising bubble.* PhD. Thesis, Twente University of Technology, The Netherlands.

Drew, D.A., & Lahey, R.T. (1982). Phase distribution mechanisms in turbulent low-quality two- phase flow in a circular pipe. *J. Fluid. Mech.*, 117, 91-106.

Drew, D.A. (2001). A turbulent dispersion model for particles or bubbles. *J. of Eng. Math.*, 41, 259-274.

Driest, E.R. van. (1956). On turbulent flow near a wall. *J. Aeron. Sci.*, vol. 23, 1007-1011.

Dukler, A.E., & Fabre, J. (1994). Gas liquid Slug flow. *Multiphase Science and Technology*, 8, 355-469.

Ellingsen, K., Risso, F., Roig. V., & Suzanne, C. (1997). Improvements of velocity measurements in bubbly flows by comparison of simultaneous hot-film and laser-Doppler anemometry signals. *ASME Fluid Eng. Div. Summer Meeting*, Paper 97-3529, Vancouver, Canada.

Farrar, B., Samways, A.L., Ali, J., & Bruun, H.H. (1995). A computer based technique for two phase flow measurements. *Meas. Sci. Technol.*, 6, 1528-1537.

Ford, B., & Loth, E. (1998). Forces on ellipsoidal bubbles in a turbulent shear layer. *Phys. Fluids*, 10, 178-188.

Fortunati, R., Guet, S., Ooms, G., & Mudde, R.F. (2002). Accuracy and feasibility of bubble dynamic measurement with a four point optical fiber probe, *Proc. of the 11th symposium on Application of Laser Technique to Fluid Mechanics*, Lisbon.

Frijlink, J.J. (1987). *Physical aspects of gassed suspension reactors*. PhD. Thesis, Delft University of Technology.

Furukawa, T., & Fukano, T. (2001). Effects of liquid viscosity on flow patterns in vertical upward gas-liquid two-phase flow. *Int. J. Multiphase Flow*, 27, 1109-1126.

Garnier, C., Lance, M., & Marié, J.L. (2002). Measurement of local flow characteristics in buoyancy-driven bubbly flow at high void fraction. *Experimental Thermal and Fluid Science*, 26, 811-815.

Gavze, E., & Shapiro, M. (1997). Particles in a shear flow near a solid wall: effect of nonsphericity on forces and velocities. *Int. J. Multiphase Flow*, 23, 155-182.

Geest, S. van, Ellepola, J.H., & Oliemans, R.V.A. (2001). Comparison of different air injection methods to improve gas-lift performance. *Proc. of the Tenth Conf. Multiphase 01'*, Cannes, France.

Geraets, J.J.M. (1986). *Centrifugal scaling of isothermal gas/liquid flow in horizontal tubes*. PhD. Thesis, Delft University of Technology.

Groen, J.S., Mudde, R.F., & Den Akker, H.E.A. van (1999). On the application of LDA to bubbly flow in the wobbling regime. *Exp. in Fluids*, 27, 435-449.

Grossetête, C. (1995). Experimental investigation of void profile development in a vertical cylindrical pipe. *Proc. of the Second International Conference on Multiphase Flow*, Kyoto, Japan.

Harmathy, T.Z. (1960). Velocity of large drops and bubbles in media of infinite or restricted extent. *AIChE Journal*, 6, 281-288.

Hibiki, T., & Ishii, M. (2002). Distribution parameter and drift velocity of drift-flux model in bubbly flow. *Int. Journal of Heat and Mass Transfer*, 45, 707-721.

Hibiki, T., & Ishii, M. (2003). One dimensional drift-flux model for two-phase flow in a large diameter pipe. *Int. Journal of Heat and Mass Transfer*, 46, 1773-1790.

Hill, D.P., Wang, D.M., Gosman, A.D., & Issa, R.I. (1995). Numerical prediction of two-phase bubbly flow in a pipe. *Proc. second Int. Conf. on Multiphase Flow*, Kyoto, Japan.

Hinze, J.O. (1975). *Turbulence*. McGraw-Hill, New York.

Ishii, M. (1975). *Thermo-fluid dynamic theory of two-phase flow*. Eyrolles, Paris.

Koide, K., Kato, S., Tanaka, Y., & Kubota, H. (1968). Bubble generated from porous plate. *Journal of Chemical Engineering of Japan*, 5, 51-56.

Kowe, R., Hunt, J.C.R., Hunt, A., Couet , B., & Bradbury, L.J.S. (1998). The effects of bubbles on the volume fluxes and the pressure gradients in unsteady and non uniform flow of liquids. *Int. J. Multiphase Flow*, 14, 587-606.

Krishna, R., Wilkinson, P.M., & Dierendonck, L.L. (1991). A model for gas holdup in bubble columns incorporating the influence of gas density on flow regime transition. *Chem. Eng. Sci.*, 14, 587-606.

Lance, M. and Lopez de Bertodano, M., (1994). Phase distribution phenomena and wall effects in bubbly two- phase flow. *Multiphase Science and Technology*, 8, 69-123.

Larue de Tournemine, A., Roig, & V., Suzanne, C. (2001). Experimental study of the turbulence in bubbly flows at high void fraction. *Proc. of the Fourth International Conference on Multiphase Flow*, New Orleans, USA.

Lathouwers, D. (1995). *Modelling and turbulent simulation of turbulent bubbly flow.* PhD. Thesis, Delft University of Technology.

Letzel, M., & Stankiewicz, A. (1999). Gas hold-up and mass transfer in gas-lift reactors operated at elevated pressure. *Chem. Eng. Sci.*, 54, 5153-5157.

Levich, V.G. (1962). *Physicochemical Hydrodynamics.* Prentice-Hall, Englewood Cliffs.

Liu, T.J. (1993a). Bubble size and entrance length effects on void development in a vertical channel. *Int. J. Multiphase Flow*, 19, 99-113.

Liu, T.J., & Bankoff, S.G. (1993b). Structure of air-water bubbly flow in a vertical pipe. 2: Void fraction, bubble velocity and bubble size distribution. *J. Heat Transfer*, 36, 1061-1072.

Liu, T.J. (2002). An Effective Signal Processing Method for Resistivity Probe Measurements in a Two-phase Bubbly Flow. *Measurement Science and Technology*, 13, 206-217.

Lopez de Bertodano, M., Lahey, R.T., & Jones, O.C. (1994). Phase distribution in bubbly two-phase flow in vertical ducts. *Int. J. Multiphase Flow*, 20, 805-818.

Lucas, D., Krepper, E., & Prasser, H.M. (2001). Prediction of radial gas profiles in vertical pipe flow on the basis of bubble size distribution. *Int. J. Therm. Sci.*, 40, 217-225.

Luo, X., Lee, D.J., Lau, R., Yang, G., & Fan, L.S. (1999). Maximum stable bubble size and hold-up in high pressure slurry bubbly column. *AIChE Journal*, 4, 665-680.

Luther, S., Rensen, J., & Guet, S. (2004). Bubble aspect ratio and velocity measurement using a four-point fiber- optical probe. *Exp. in Fluids*, 36, 326-333.

Maanen, H.R.E. van. (1999a). *Retrieval of turbulence and turbulence properties from randomly sampled Laser Doppler Anemometry data with noise.* PhD. Thesis, Delft University of Technology.

Maanen, H.R.E. van, Nobach, H., & Benedict, L.H. (1999b). Improved estimator for the slotted autocorrelation function of randomly sampled LDA data. *Measurement Science and Technology*, 10, L4 - L7.

Maanen, H.R.E. van, & Oldenziel, A. (1998). Estimation of turbulence power spectra from randomly sampled data by curve-fit to the autocorrelation function applied to laser-Doppler anemometry. *Measurement Science and Technology*, 9, 458-467.

Magnaudet, J., & Eames, I. (2000). The motion of high-Reynolds-number bubbles in inhomogeneous flows. *Ann. Rev. Fluid Mech.* 32, 659-708.

Magnaudet, J., Takagi, S., & Legendre, D. (2003). Drag, deformation and lateral migration of a buoyant drop moving near a wall. *J. Fluid. Mech.*, 476, 115-157.

Mishima, K., & Ishii, M. (1984). Flow regime transition criteria for upward two-phase flow in vertical tubes. *Int. J. Heat Mass Transfer*, 27, 723-737.

Molen, K. van der, & Maanen, H.R.E. van. (1978). Laser-Doppler measurements of the turbulent flow in stirred vessels to establish scaling rules. *Chem. Eng. Science*, vol.33, pp 1161-1168.

Moraga, F.J., Larreteguy, A.E., Drew, D.A., & Lahey Jr., R. T. (2003). Assessmentof turbulent dispersion models for bubbly flows in the low Stokes number limit. *Int. J. Multiphase Flow*, 29, 655-373.

Mortazavi, S., & Tryggvason, G. (2000). A numerical study of the motion of drops in Poiseuille flow. Part 1. Lateral migration of one drop. *J. Fluid. Mech.*, 411, 325-350.

Moursali, E., Marié, L., & Bataille, J. (1995). An upward turbulent bubbly boundary layer along a vertical flat plate. *Int. J. Multiphase Flow*, 21, 107-117.

Mudde, R.F., Groen, J.S., & Den Akker, H.E.A. van. (1997). Liquid velocity field in a bubble column: LDA experiments. *Chem. Eng. Sci.*, 52, 4217-4224.

Mudde, R.F., Groen, J.S., & Den Akker, H.E.A. van. (1998). Application of LDA to bubbly flows. *Nuclear Engineering and Design*, 184, 329-338.

Mudde, R.F., & Simonin, O. (1999). Two and three-dimensional simulations of a bubble plume using a two-fluid model. *Chem. Eng. Sci.*, 54, 5061-5069.

Mudde, R.F., & Saito, T. (2001). Hydrodynamical similarities between bubble column and bubbly pipe flow. *J. Fluid. Mech.*, 437, 203-228.

Ohnuki, A., & Akimoto, H. (1996). An experimental study on developing air-water two phase flow along a large diameter pipe: effect of air injection method. *Int. J. Multiphase Flow*, 22, 1143-1154.

Ohnuki, A., & Akimoto, H. (2000). Experimental study on transition of flow pattern and phase distribution in upward air- water two-phase flow along a large vertical pipe. *Int. J. Multiphase Flow*, 26, 367-386.

Ohnuki, A., & Akimoto, H. (2001). Model development for bubble turbulent diffusion and bubble diameter in large vertical pipes. *Journal of Nuclear Science and Technology*, 38, 1074-1080.

Peebles, F.N., & Garber, H.J. (1953). Studies on the motion of gas bubbles in liquids. *Chem. Engineering Progress*, 49, 88-97.

Politano, M.S., Carrica. P.M., & Converti, J. (2003). A model for turbulent polydisperse-two phase flow in vertical channels. *Int. J. Multiphase Flow*, 29, 1153-1182.

Reichardt, H. (1951). Vollständige Darstellung der turbulenten Geschwindigkeitsverteilung in glatten Leitungen. ZAMM, vol. 31, 208-219.

Rensen, J. (2003). *Bubbly Flow Hydrodynamic: Forces and Turbulence*. PhD. Thesis, University of Twente.

Richardson, J.F., & Zaki, W.N. (1954). Sedimentation and Fluidization: part 1. *Trans. Instr. Chem. Engrs*, 32, 35-53.

Rivière, N., & Cartellier, A. (1999). Wall shear stress and void fraction in poiseuille bubbly flows: Part 1: simple analytic predictions. *Eur. J. Mech. B/Fluids*, 18, 823.

Saito, T., & Mudde, R.F. (2001). Performance of 4-tip optical fiber probe and bubble characterization by the probe in turbulent bubbly flows. *Proc. of the Fourth International Conference on Multiphase Flow*, New Orleans, USA.

Sato, Y., Sadatomi, L., & Sekogushi, K. (1981). Momentum and heat transfer in two phase bubbly flow. *Int. J. Multiphase Flow*, 7, 167-190.

Serizawa, A., Kataoka, I., & Michiyoshi, I. (1975). Turbulence structure of air-water bubbly flows - 2. Local properties. *Int. J. Multiphase Flow*, 2, 235-246.

Serizawa, A., & Kataoka, I. (1994). Dispersed flow-1. *Multiphase Science and Technology*, 8, 125-194.

Song, C.H., No, H.C., & Chung, M.K. (1995). Investigation of bubble flow developments and its transition based on the instability of void fraction waves. *Int. J. Multiphase Flow*, 21, 381-404.

Stuhmiller , J.H. (1977). The influence of interfacial pressure forces on the character of two-phase flow model equations. *Int. J. Multiphase Flow*, 3, 551-560.

Taitel, Y., Bornea, D., & Dukler, A.E. (1980). Modeling flow pattern transitions for steady upward gas- liquid flow in vertical tubes. *AIChE Journal*, 26, 345-354.

Tomiyama, A. (1998). Struggle with computational bubble dynamics. *Third International Conference on Multiphase Flow*, ICMF '98, Lyon, France, June 8-12.

Tomiyama, A., Tamai, H., Celata, G.P., Hosokawa, S., & Yoshida, S. (2002a). Terminal velocity of single bubbles in surface tension force dominant regime. *Int. J. Multiphase Flow*, 28, 1497-1519.

Tomiyama, A., Tamai, H., Zun, I., & Hosokawa, S. (2002b). Transverse migration of single bubbles in simple shear flow. *Chem. Eng. Sci.*, 57, 1849-1858.

Troshko, A.A., & Hassan, Y.A. (2001). A two-equation turbulence model of turbulent bubbly flow. *Int. J. Multiphase Flow*, 27, 1965-2000.

Urseanu, M.I., Guit, R.P.M., Stankiewicz, A., Kranenburg, G. van., & Lommen, J.H.G.M. (2003). Influence of operating pressure on the gas hold-up in bubble columns for high viscous media. *Chem. Eng. Sci.*, 58, 697-704.

Wang, S.K., Lee, S.J., Jones, O.C., & Lahey Jr, R.T. (1987). 3-D turbulence structure and phase distribution measurements in bubbly two-phase flow. *Int. J. Multiphase Flow*, 13, 327-343.

Wellek, R.M., Arawal, A.K., & Skelland, A.H.P. (1966). Shapes of liquid drops moving in liquid media. *AIChE J.*, 12, 854-862.

Wijngaarden, L. van. (1991). Bubble deformation in bubbly liquids and its effect on the stability of void fraction waves. *Mathematical approaches in hydrodynamics*, SIAM, 38-49.

Wilkinson, P.M., Schayk, A. van, Spronken, J.P.M., & Dieredonck, L.L. van. (1993). The influence of gas density and liquid properties on bubble breakup. *Chem. Eng. Sci.*, 48, 1213-1226.

Zenit, R., Koch, D.L., & Sangani, A. (2001). Measurements of the average properties of a suspension of bubbles rising in a vertical channel. *J. Fluid. Mech.*, 429, 307-341.

Zuber, N., & Findlay, J.A. (1965). Average volumetric concentration in two-phase flow systems. *J. Heat Transfer Trans. ASME*, 87, 453-468.

Nomenclature

Symbol	Description	Unit
A	Pipe cross section	m^2
C_d	Drag force coefficient	$-$
C_l	Lift force coefficient	$-$
C_0	Drift-flux model distribution parameter	$-$
d	Four-point probe vertical dimension	m
D_b	Bubble spherical equivalent diameter	m
D_{bv}	Bubble vertical chord length	m
D_{bh}	Bubble horizontal chord length	m
D_p	Pipe diameter	m
h	height	m
H	Pipe height	m
j_k	Flux of phase k	$m\,s^{-1}$
P	Pressure	$N\,m^{-2}$
P_{kI}	Pressure at the interface of phase k	$N\,m^{-2}$
Q_k	Volumetric flow rate of phase k	$m^3\,s^{-1}$
R	Pipe radius	m
Re_{sl}	Liquid Reynolds number	$-$
Re_m	Mixture Reynolds number	$-$
r	Radial position	m
R_b	Bubble radius	m
r_{blade}	Stirring vessel blade radius	m
s	Four-point probe horizontal dimension	m
U_{drift}	Bubble drift velocity	$m\,s^{-1}$
U_k	Velocity of phase k	$m\,s^{-1}$
U_{sk}	Superficial velocity of phase k	$m\,s^{-1}$
U_{slip}	Bubble slip velocity	$m\,s^{-1}$
U_t	Single-bubble terminal velocity	$m\,s^{-1}$

β	Bubble selection parameter	-
χ	Bubble aspect ratio D_{bh}/D_{bv}	-
γ	Bubble angle of orientation	rad
ϵ	Void fraction	-
ϵ_c	Critical void fraction	-
μ	Dynamic viscosity	$Pa\,s$
ν	Kinematic viscosity	$m^2\,s^{-1}$
ω	Rotational speed	rpm
ρ	Density	$kg\,m^{-3}$
σ	Surface tension	$N\,m^{-1}$
τ	Bubble time of flight	s
$\boldsymbol{\tau}_k$	Stress tensor in phase k	$N\,m^{-2}$

$\langle\langle\rangle\rangle$	Averaging in two-fluid model
$<>$	Area-average
$\|\|$	Void fraction-weighted area average
ACF	Auto Correlation Function
LDA	Laser-Doppler Anemometry
PDF	Probability Density Function
TID	Time Interval Distribution
g	Gas phase subscript
l	Liquid phase subscript

Acknowledgments

This project was supported financially by the European Union, through the European network on Nonideal Turbulence. The experimental set-up and measurement techniques were provided by Shell E&P, Rijswijk, the Netherlands. I should like to acknowledge these institutions and all the people who contributed to this work. In particular I acknowledge my advisors Gijs Ooms and René Oliemans for the number of discussions and for the top-quality support provided during this study. I am also gratefull to Rob Mudde for the stimulating discussions and suggestions on bubbly-flow measurement techniques, and Hans van Maanen for the very useful cooperative work on the LDA measurements.

I would also like to thank Stefan Luther and Judith Rensen for the interesting cooperative project on the bubble shape and orientation determination from four point-optical fibre probe time series, and Detlef Lohse for receiving me in his laboratory during this investigation. I am also grateful to Frans Nieuwstadt for receiving me at the laboratory for Aero-and Hydrodynamics in Delft University of Technology.

A large part of this research was carried out in the Fluid and Solid Mechanics research team at Shell laboratories (Rijswijk, the Netherlands). I would like to acknowledge Michiel Groeneveld for receiving me in his team and Ben van den Brule for the stimulating support. The years spent in this team were a very interesting experience, during which I learnt to participate in research and development activities. I am also grateful to Richard Fernandes and Jerome Ellepola for the multiple discussions and supports.

Special thanks go to the students who carried out their final thesis graduation work with me: Simon van Geest, Robbert Fortunati and Michiel Visser't Hooft. I am also grateful to Jan Kater, from the group of Gert Colenbrander (Shell Amsterdam), for the time spent in making a LDA equipment available to me for the present investigation.

Finally, I acknowledge my family, particularly my parents and my partner Paulien Bos for the enthusiastic and encouraging support during this research.

About the author

Sébastien Guet was born on the 21^{st} of November 1974. During his childhood he lived six years in Fes and ten years in Abidjan. He graduated from high school in Melun, France. After graduation he studied Mechanical Engineering (University of Evry, France). In 1999 he obtained a postgraduate certificate in Fluid Mechanics (DEA 'Dynamique des Fluides et des Transferts') at the University of Orsay, France. During his final graduation project, he carried out velocity measurements in a thermo-acoustic resonator (Laboratory LIMSI/CNRS, Orsay). In 1999, Sébastien Guet came in the Netherlands to work as a military service scientist and carried out the PhD research reported in this thesis.

Publications

- Guet, S., & Ooms, G. (2001). On the importance of modelling and numerical simulation of practical flow problems from the oil industry. *La Houille blanche*, 1-2001, 30-33.
- Guet, S., Ooms, G., & Oliemans, R.V.A. (2002). Influence of bubble size on the transition from low-Re bubbly flow to slug flow in a vertical pipe. *Experimental Thermal and Fluid Science*, 26, 635-641.
- Guet, S., Ooms, G., Oliemans, R.V.A., & Mudde, R.F. (2003). Bubble injector effect on the gaslift efficiency. *AIChE Journal*, 49, 9, 2242-2252.
- Guet, S., Fortunati, R.V., Mudde, R.F., & Ooms, G. (2003). Bubble velocity and size measurements with a four-point optical fibre probe. *Part. and Part. Syst. Char. Journal*, 20, 219-230.
- Luther, S., Rensen, J., & Guet, S. (2004). Bubble aspect ratio and velocity measurement using a four-point fiber-optical probe. *Exp. in Fluids*, 36, 326-333.
- Guet, S., Ooms, G., Oliemans, R.V.A., & Mudde, R.F. Bubble size effect on low liquid input drift-flux parameters. Accepted for publication in *Chemical Engineering Science*.
- Guet, S., Ooms, G., & Oliemans, R.V.A. A simplified Euler-Euler model for gas-lift efficiency predictions. Submitted for publication in *AIChE Journal*.

Participations in international conferences

- Ooms, G., & Guet, S. On the importance of modelling and numerical simulation of practical flow problems from the oil industry. *26èmes Journées de l'Hydraulique*, September 2000, Marne La Vallée, France.
- Guet, S., Ooms, G., & Oliemans, R.V.A. Influence of bubble size on the transition from low Re-bubbly to slug flow in a vertical pipe. Paper presented at the *Fourth International Conference on Multiphase Flow (ICMF4)*, May - June 2001, New Orleans, LA, USA.
- Fortunati, R., Guet, S., & Ooms, G. Accuracy and feasibility of bubble dynamic measurement with a four point optical fibre probe. *Proceeding of the 11th symposium on Application of Laser Technique to Fluid Mechanics*, July 2002, Lisbon, Portugal.
- Guet, S., Maanen, H.R.E. van, & Mudde, R.F. Feasibility of LDA measurements in high void fraction bubbly flow. *Proceeding of the 11th symposium on Application of Laser Technique to Fluid Mechanics*, July 2002, Lisbon, Portugal.
- Guet, S., Ooms, G., Oliemans, R.V.A., & Mudde, R.F. Coupling between velocities and void fraction profile in a vertical bubbly pipe flow. Presented at the *Euromech fluid mechanics conference*, September 2003, Toulouse, France.
- Guet, S., Rensen, J., & Luther, S. Bubble aspect ratio and velocity measurements using a four-point optical fibre probe. Accepted for oral presentation at the *Third International Symposium on two-phase flow modelling and instrumentation*, September 2004, Pisa, Italy.
- Guet, S., Luther, S., & Ooms, G. Bubble transverse distribution effects on the airlift efficiency. Accepted for oral presentation at the *Fifth International Conference on Multiphase Flow (ICMF5)*, May - June 2004, Yokohama, Japan.